

Thermal Radiation Modeling for Automotive Applications

Dissertation

by

Dipl.-Ing. Christian Rauch

Submitted to the Department of Mechanical Engineering

at

Graz University of Technology

in partial fulfillment of the requirements for the degree of

Doktor der technischen Wissenschaften

Doctor technicae

in collaboration with

Kompetenzzentrum - Das virtuelle Fahrzeug Forschungsgesellschaft mbH

under the supervision of

Ao.Univ.-Prof. Dipl.-Ing. Dr.techn. Raimund Almbauer

of the Institute of Internal Combustion Engines and Thermodynamics

at Graz University of Technology

October 2012

Deutsche Fassung:
Beschluss der Curricula-Kommission für Bachelor-, Master- und Diplomstudien vom 10.11.2008
Genehmigung des Senates am 1.12.2008

EIDESSTÄTLICHE ERKLÄRUNG

Ich erkläre an Eides statt, dass ich die vorliegende Arbeit selbstständig verfasst, andere als die angegebenen Quellen/Hilfsmittel nicht benutzt, und die den benutzten Quellen wörtlich und inhaltlich entnommenen Stellen als solche kenntlich gemacht habe.

Graz, am

.....
(Unterschrift)

Englische Fassung:

STATUTORY DECLARATION

I declare that I have authored this thesis independently, that I have not used other than the declared sources / resources, and that I have explicitly marked all material which has been quoted either literally or by content from the used sources.

.....
date

.....
(signature)

Abstract

Insight is given on how and why thermal radiation is being calculated in the automotive industry. The radiation method most used in this sector is described along with recent developments in dealing with meshes of industrial size. A coupling architecture between a computational fluid dynamics (CFD) code and a thermal radiation solver is presented. It is demonstrated why one needs to know how changing parameters will influence simulation results. Equations for local sensitivity and uncertainty analysis are derived for conjugate heat transfer problems and their usability is demonstrated on simple models. This treatment constitutes an enlargement of the current state of knowledge on sensitivity and uncertainty analysis in thermal radiation calculations.

Kurzfassung

Es wird ein Einblick in die Berechnung und Anwendungsgebiete der thermischen Strahlung in der Automobilindustrie gewährt. Das in diesem Industriezweig meistverwendete Strahlungsmodell wird beschrieben mit den neuesten Entwicklungen zur Bearbeitung von Netzen industrieller Größe. Eine Kopplungsarchitektur zwischen einem Programm zur Strömungsanalyse und einem thermischen Strahlungslöser wird beschrieben. Es wird dargestellt warum man bei einer Simulation wissen sollte, wie einzelne Parameter Einfluss auf das Ergebnis nehmen. Gleichungen für eine lokale Sensitivitäts- und Unsicherheitsanalyse für konjugierte Wärmeübergangsprobleme werden hergeleitet und diese Methode an einfachen Beispielen demonstriert. Diese Arbeit stellt eine Erweiterung des bisherigen Kenntnisstandes zur Sensitivitäts- und Unsicherheitsanalyse in der Strahlungsberechnung dar.

Acknowledgment

The author would like to acknowledge the financial support of the "COMET K2 - Competence Centres for Excellent Technologies Programme" of the Austrian Federal Ministry for Transport, Innovation and Technology (BMVIT), the Austrian Federal Ministry of Economy, Family and Youth (BMWFJ), the Austrian Research Promotion Agency (FFG), the Province of Styria and the Styrian Business Promotion Agency (SFG). The author would like to express his thanks to Ao.Univ.-Prof. Dipl.-Ing. Dr.techn. Raimund Almbauer of the Institute of Internal Combustion Engines and Thermodynamics at Graz University of Technology and Prof. Dr.-Ing. Stephan Kabelac of the Institute of Thermodynamics at Leibniz Universität Hannover for acting as dissertation advisors, as well as to Graz University of Technology.

I owe gratitude to George Walton from the National Institute of Standards (NIST) in providing the source code of View3D and to Volker Wippel for helping in the implementation of the LU solver.

Finally, thank you to my wife Doris who kept in check our two children.

Danksagung

Der Autor dankt dem „COMET K2 Forschungsförderungs-Programm“ des Österreichischen Bundesministeriums für Verkehr, Innovation und Technologie (BMVIT), des Österreichischen Bundesministeriums für Wirtschaft, Familie und Jugend (BMWFJ), der Österreichischen Forschungsförderungsgesellschaft mbH (FFG), des Landes Steiermark sowie der Steirischen Wirtschaftsförderung (SFG) für die finanzielle Unterstützung. Ebenfalls dankt der Autor Ao.Univ.-Prof. Dipl.-Ing. Dr.techn. Raimund Almbauer vom Institut für Verbrennungskraftmaschinen und Thermodynamik an der Technischen Universität Graz und Prof. Dr.-Ing. Stephan Kabelac vom Institut für Thermodynamik, Leibniz Universität Hannover für deren Funktion als Doktorväter, sowie der Technischen Universität Graz.

Ich schulde George Walton vom National Institute of Standards (NIST) Dank für die Bereitstellung des Quellcodes von View3D und Dr. Volker Wippel für die Hilfe bei der Implementierung des LU-Lösers.

Schließlich danke ich meiner Frau Doris, die unsere beiden Kinder in Schach hielt.

Table of Contents

1	Introduction	1
1.1	Topical Overview	1
1.2	Impact	2
2	Thermal Radiation and the Automobile	4
2.1	Introduction	4
2.2	Material Properties	4
2.3	Thermal Radiation Models	7
2.4	Thermal Radiation Solvers	10
2.5	Thermal Radiation in the Automotive Industry	11
2.6	Thermal Radiation in the Product Development Process	18
3	Surface-to-Surface Model	22
3.1	Introduction	22
3.2	Energy Balance	22
3.3	View Factors	25
3.3.1	Taxonomy of View Factor Estimation	25
3.3.2	View Factors and Thermodynamics	42
3.3.3	Correcting View Factors	43
3.4	Data Structures for View Factor Calculation	46
3.4.1	Space Partitioning	46
3.4.2	Bounding Volumes	50
3.5	Benchmarks	51
4	Coupling of Thermal Systems	62
4.1	Introduction	62
4.2	Systems Requirements	62
4.3	Coupling Architecture	67
4.4	Test Case	70
4.5	Simulation	72
5	Sensitivity and Uncertainty Analysis	80
5.1	Taxonomy	80
5.2	Previous Research on View Factor Uncertainties	86
5.3	Mathematical Formulation	90
5.3.1	Sensitivity of View Factors	90
5.3.2	Sensitivity of Emissivity	96
5.3.3	Sensitivity of Fluid Temperature	101
5.3.4	Sensitivity to Conductance	104
5.3.5	Calculation Procedure for Sensitivity Coefficients	107
5.4	Uncertainty	109
5.5	Case Hexahedron	110
5.6	Numerical Analysis	116
5.6.1	Numerical Stability	117
5.6.2	Partial Uncertainties	120
5.6.3	Accuracy of Uncertainty Prediction	122
6	Conclusions	133
7	Literature	136
8	Appendix	144
8.1	Case Hexahedron for Uncertainty Calculation	144
8.2	Uncertainty Factors for the Muffler	145

Table of Figures

Figure 1-1: Memory requirements TheseusFE versus RadTherm by P+Z Engineering.....	2
Figure 1-2: Run-time TheseusFE versus RadTherm by P+Z Engineering.	3
Figure 2-1: Thermal radiation in the electromagnetic spectrum. Reprinted from (Modest, 2003), Copyright © 2003, with permission from Elsevier Inc.....	4
Figure 2-2: Transmissivity of two windshields (Farrington and Rugh, 2000).....	5
Figure 2-3: Hemispherical directional spectral reflectivity of steel for various reflected directions (Vujić et al., 2006a). Copyright © 2006 Taylor & Francis Group.	6
Figure 2-4: Normal spectral emissivity for Inconel X (Siegel and Howell, 2002). Copyright © 2002 Taylor & Francis Group.	6
Figure 2-5: Thermal radiation models.....	7
Figure 2-6: Control volume for the differential RTE.....	8
Figure 2-7: Heat sources in the underhood.	11
Figure 2-8: Muffler internals (left) and simulated surface temperatures (right) (Herrera and Lund, 2007).....	12
Figure 2-9: Mapping of surface temperatures from IR Thermography (Frémond, 2008).	13
Figure 2-10: Engine mount temperatures (Weidmann et al., 2004).....	13
Figure 2-11: Hardy disc temperatures (Moshhammer, 2006).....	14
Figure 2-12: Battery temperatures in the trunk of a car (Michel et al., 2006).	14
Figure 2-13: Disc brake cooling (Jansen, 2004).	15
Figure 2-14: Temperature of Silverstone track (Jussila, 2007).....	16
Figure 2-15: Coimbra box with dummy of 16 segments (Rauch et al., 2004).....	16
Figure 2-16: Share of radiative heat flux for manikin of 16 segments (Rauch et al., 2004)....	17
Figure 2-17: Level of awareness for thermal radiation.	18
Figure 2-18: Basic development process.	19
Figure 2-19: Advanced development process.	20
Figure 2-20: Heat protection activity flow at Jaguar/Land Rover (Jansen, 2007).	20
Figure 3-1: Differential solid angle.....	26
Figure 3-2: Form factor taxonomy according to Cohen and Wallace (1993).	27
Figure 3-3: Nomenclature for single line integration (1LI) (Walton, 2002).....	28
Figure 3-4: Nomenclature for single area integration (1AI) (Walton, 2002).....	29
Figure 3-5: Run-time behavior for view factor models (Walton, 2002).	30
Figure 3-6: Point locations for Gaussian area integration (Walton, 2002).	31
Figure 3-7: Study of point source shadows by da Vinci. Copyright © 2003 Wiley. Used with permission from (Hasenfratz et al., 2003).....	32
Figure 3-8: Shadow construction by Lambert. Copyright © 2003 Wiley. Used with permission from (Hasenfratz et al., 2003).	32
Figure 3-9: Hard shadow. Copyright © 2003 Wiley. Used with permission from (Hasenfratz et al., 2003).....	32
Figure 3-10: Soft shadow. Copyright © 2003 Wiley. Used with permission from (Hasenfratz et al., 2003).....	33
Figure 3-11: Soft shadow with two obstructions. Copyright © 2003 Wiley. Used with permission from (Hasenfratz et al., 2003).....	33
Figure 3-12: Partially obstructed view for blockage factor (Walton, 2002).	34
Figure 3-13: Shadow projection.	35
Figure 3-14: Determination of blockage factor (Nishita and Nakamae, 1985). © 1985, ACM, Inc.....	35
Figure 3-15: Adaptive subdivisioning (Walton, 2002).	36

Figure 3-16: Adaptive mesh refinement (Saltiel and Kolibal, 1993). Copyright © 1991 by AIAA, Inc. Reprinted with permission of the American Institute of Aeronautics and Astronautics.....	37
Figure 3-17: Projection on a hemi-cube (Fleischmann, 2007).....	38
Figure 3-18: Nusselt’s analogy (Fleischmann, 2007).	38
Figure 3-19: Relative error in view factors for hemi-cube by Baum et al. (1989). © 1989, ACM, Inc.....	39
Figure 3-20: Visibility assumption (Baum et al., 1989). © 1989, ACM, Inc.	40
Figure 3-21: Aliasing effect (Baum et al., 1989). © 1989, ACM, Inc.	40
Figure 3-22: Hemi-sphere-Base projection. Copyright © 2009 Wiley. Used with permission from (Yamada et al., 2009).	41
Figure 3-23: Cell registration on Hemi-sphere-Base. Copyright © 2009 Wiley. Used with permission from (Yamada et al., 2009).	41
Figure 3-24: Heat flux standard deviations for view factor rectification (Taylor and Luck, 1995). Copyright © 1995 by AIAA, Inc. Reprinted with permission of the American Institute of Aeronautics and Astronautics.	45
Figure 3-25: Octree (Paulke, 2007).....	47
Figure 3-26: Kd Tree in 2D (Fleischmann, 2007).....	48
Figure 3-27: Occlusion calling with kd tree (Paulke, 2007).	48
Figure 3-28: Kd tree in 3D (Paulke, 2007).....	49
Figure 3-29: BSP tree (Fleischmann, 2007).....	50
Figure 3-30: Bounding volumes modified from (Fleischmann, 2007).	50
Figure 3-31: View factor error for the hexahedron for various programs (Rauch et al., 2007). © 2007, Chandos Publishing (Oxford) Ltd.	52
Figure 3-32: Heat flux error for the hexahedron for various programs (Rauch et al., 2007). © 2007, Chandos Publishing (Oxford) Ltd.	53
Figure 3-33: Benchmark Shapiro with front side removed (Rauch et al., 2007). © 2007, Chandos Publishing (Oxford) Ltd.	54
Figure 3-34: View factor error for Shapiro for various programs (Rauch et al., 2007). © 2007, Chandos Publishing (Oxford) Ltd.	55
Figure 3-35: Heat flux error for Shapiro for various programs (Rauch et al., 2007). © 2007, Chandos Publishing (Oxford) Ltd.	55
Figure 3-36: Benchmark Coimbra without roof (Rauch et al., 2007). © 2007, Chandos Publishing (Oxford) Ltd.	56
Figure 3-37: Memory requirements for Coimbra (Rauch et al., 2008). © 2007, Chandos Publishing (Oxford) Ltd.	58
Figure 3-38: Run-time for Coimbra (Rauch et al., 2007). © 2007, Chandos Publishing (Oxford) Ltd.	58
Figure 3-39: File size for Coimbra (Rauch et al., 2008a). Copyright © 2008 by ASME.	59
Figure 3-40: Number of face entries of face 58758 for Coimbra.....	60
Figure 3-41: RAM usage for Coimbra (Rauch et al., 2008a). Copyright © 2008 by ASME. .	60
Figure 3-42: Runtime for Coimbra with FLUENT.	61
Figure 4-1: Differing mesh topology. (Heinstein and Laursen, 2003).....	64
Figure 4-2: Common refinement mesh. Copyright © 2004 Wiley. Used with permission from (Jiao and Heath, 2004).	65
Figure 4-3: Underbody temperatures with coupling (Tastan, 2008).	65
Figure 4-4: Component diagram of coupling architecture (Rauch et al., 2008). Reprinted with permission from SAE Paper No. 2008-01-0389 © 2008 SAE International.	67

Figure 4-5: Deployment diagram for the standard FLUENT interface in parallel (Rauch et al., 2008). Reprinted with permission from SAE Paper No. 2008-01-0389 © 2008 SAE International.	68
Figure 4-6: Deployment diagram for the parallel architecture (Rauch et al., 2008a). Copyright © 2008 by ASME.....	69
Figure 4-7: Measurement points for the exhaust system (Rauch et al., 2008a). Copyright © 2008 by ASME.....	71
Figure 4-8: CFD coupling interface (Rauch et al., 2008a). Copyright © 2008 by ASME.	72
Figure 4-9: RadTherm coupling interface (Rauch et al., 2008a). Copyright © 2008 by ASME.	73
Figure 4-10: Temperature differences of measurement and simulation at the floor pan heat shield.	74
Figure 4-11: Thermographic image of connector pipe (Rauch et al., 2008a). Copyright © 2008 by ASME.....	75
Figure 4-12: Volume mesh of the exhaust system (Rauch et al., 2008a). Copyright © 2008 by ASME.....	76
Figure 4-13: Simulation temperature differences to measurements at the floor pan heat shield (Rauch et al., 2008a). Copyright © 2008 by ASME.	76
Figure 4-14: Simulation temperature differences to measurements at the exhaust pipe facing the road (Rauch et al., 2008a). Copyright © 2008 by ASME.	77
Figure 4-15: Simulation temperature differences to measurements at the exhaust pipe facing the heat shield (Rauch et al., 2008a). Copyright © 2008 by ASME.	77
Figure 4-16: Simulation temperature differences to measurements at heat shield for $c_p=0$	78
Figure 4-17: Simulation temperature differences to measurements at the exhaust pipe facing the heat shield for $c_p=0$	78
Figure 4-18: Simulation temperature differences to measurements at the exhaust pipe facing the heat shield for $c_p=0$ and coupling time step of 0.02 s.....	79
Figure 5-1: Taxonomy of sensitivity analysis.	81
Figure 5-2: Taxonomy of screening.	82
Figure 5-3: Taxonomy of global SA.	82
Figure 5-4: Subset simulation procedure (Thunnissen et al., 2007). Copyright © 2006 by AIAA, Inc. Reprinted with permission of the American Institute of Aeronautics and Astronautics.....	84
Figure 5-5: Taxonomy of local SA according to Blackwell and Dowding (2006).	84
Figure 5-6: Epistemic and aleatory uncertainty (Guo and Du, 2007). Copyright © 2007 by AIAA, Inc. Reprinted with permission of the American Institute of Aeronautics and Astronautics.....	86
Figure 5-7: Uncertainty $\omega_{R_{ij}}$ for distribution factor R_{ij} Reprinted from (Shuai et al., 2008), Copyright © 2007, with permission from Elsevier Inc.	88
Figure 5-8: Thermal node with heat fluxes.	92
Figure 5-9: Activity diagram for calculation procedure.....	108
Figure 5-10: Case hexahedron.....	110
Figure 5-11: Relative view factor error for the hexahedron from face ‘Bottom’.	111
Figure 5-12: Calculated face temperatures for the hexahedron.	111
Figure 5-13: Radiative heat flux from face ‘Back’ for the hexahedron.	112
Figure 5-14: Radiosity flux from face ‘Back’ for the hexahedron.....	112
Figure 5-15: Dimensionless, normalized sensitivity coefficient of emissivity from face ‘Back’ for the hexahedron.....	113
Figure 5-16: Uncertainty factor of emissivity for the hexahedron.....	113

Figure 5-17: Dimensionless, normalized sensitivity coefficient of form factor from face ‘Back’ to ‘Bottom’ for the hexahedron.	114
Figure 5-18: Uncertainty factor of form factor for the hexahedron.	115
Figure 5-19: Uncertainty factor of T_f for the hexahedron.	116
Figure 5-20: Muffler with two test faces.	116
Figure 5-21: Stability analysis for the radiation term for the muffler (Rauch and Almbauer, 2010). Copyright © 2010 by AIAA, Inc. Reprinted with permission of the American Institute of Aeronautics and Astronautics.	117
Figure 5-22: Stability analysis for radiation and convective terms for the muffler (Rauch and Almbauer, 2010). Copyright © 2010 by AIAA, Inc. Reprinted with permission of the American Institute of Aeronautics and Astronautics.	118
Figure 5-23: Stability analysis for radiation and conduction terms for the muffler (Rauch and Almbauer, 2010). Copyright © 2010 by AIAA, Inc. Reprinted with permission of the American Institute of Aeronautics and Astronautics.	118
Figure 5-24: Stability analysis for radiation, convection, and conduction terms for the muffler.	119
Figure 5-25: Partial uncertainty calculation for node 28 of the muffler system.	120
Figure 5-26: Partial uncertainty calculation for node 96 of the muffler system.	121
Figure 5-27: Difference of new simulation with prediction by uncertainty of the front nodes.	122
Figure 5-28: Difference of new simulation with prediction by uncertainty of the backside nodes.	122
Figure 5-29: Case step.	123
Figure 5-30: Temperatures for Step at $Q=50W$ with changing fluid temperature.	124
Figure 5-31: Temperature differences for Step at $Q=50W$ with changing fluid temperature.	125
Figure 5-32: Temperature differences for Step with different heat sources and changing fluid temperature.	125
Figure 5-33: Temperatures for Step at $Q=50W$ with changing view factor error.	126
Figure 5-34: Temperature differences for Step at $Q=50W$ with changing view factors.	127
Figure 5-35: Temperature differences for Step with different heat sources and changing view factors.	127
Figure 5-36: Temperatures for Step at $Q=50W$ with changing emissivity.	128
Figure 5-37: Temperature differences for Step at $Q=50W$ with changing emissivity.	128
Figure 5-38: Temperatures for Step with different heat sources and changing emissivity.	129
Figure 5-39: Temperature differences for Step with different heat sources and changing emissivity.	129
Figure 5-40: Temperatures for Step at $Q=50W$ with changing thickness.	130
Figure 5-41: Heat flux shares for Step at $Q=50W$ with changing thickness.	130
Figure 5-42: Temperature differences for Step at $Q=50W$ with changing thickness.	131
Figure 5-43: Temperature differences for Step with different heat sources and changing thickness.	131
Figure 5-44: Temperature differences for Step at $Q=50W$ and UFs at a thickness of 0.05m with changing thickness.	132
Figure 5-45: Temperature differences for Step with different heat sources and UFs at a thickness of 0.05m with changing thickness.	132
Figure 8-1: Uncertainty factor for fluid temperature for front nodes of the muffler.	145
Figure 8-2: Uncertainty factor for fluid temperature for back nodes of the muffler.	146
Figure 8-3: Uncertainty factor for emissivity for front nodes of the muffler.	146
Figure 8-4: Uncertainty factor for emissivity for back nodes of the muffler.	147
Figure 8-5: Uncertainty factor for view factor for front nodes of the muffler.	147

Figure 8-6: Uncertainty factor for view factor for back nodes of the muffler.	148
Figure 8-7: Uncertainty factor for conductance for front nodes of the muffler.	148
Figure 8-8: Uncertainty factor for conductance for back nodes of the muffler.	149

Table of Tables

Table 2-1: Thermal radiation solvers.	10
Table 4-1: Emissivity coefficients of the connector pipe (Rauch et al., 2008a). Copyright © 2008 by ASME.	75
Table 5-1: Boundary conditions for hexahedron.....	110
Table 5-2: Boundary conditions for the muffler.	117
Table 5-3: Heat fluxes for two nodes of the muffler.....	120
Table 5-4: Boundary conditions for the step example.	124
Table 8-1: Analytical view factors for hexahedron.....	144
Table 8-2: Normalized sensitivity coefficients with analytical view factors for the hexahedron.	144

NOMENCLATURE

A	Area [m^2]
a	Matrix Entity [-]
a	Vector for Single Area Integration
b	Blockage Factor [-]; Boundary Heat Flux [W/m^2]
b	Vector for Single Area Integration
C	Conductance, Conductor [W/K]
C	Error Bound, Convergence Measure [-]; Contour
C_p	Specific Heat Capacity [$\text{J}/\text{kg}/\text{K}$]
c	Vector for Single Area Integration
D	Distribution Function [-]
D	Diagonal Matrix
d	Correction factor [-]; Factor for Single Area Integration
E	Number of Edges
e	Factor for Single Area Integration
F	View Factor [-]
F	View Factor Matrix
<i>F</i>	Fraction
f	Function
g	Vector for Single Area Integration
h	Convective Heat Transfer Coefficient [$\text{W}/\text{m}^2/\text{K}$]
I	Light Intensity, Radiative Intensity [$\text{W}/\text{Steradant}$]
I	Identity Matrix
i	Radiative Intensity Flux [$\text{W}/\text{m}^2/\text{Steradant}$]
k	Thermal Conductivity [$\text{W}/\text{m}/\text{K}$]

K	Confidence Measure [-]
l	Distance between Node Centers [m]
M	Matrix
m	Number of Nonzero View Factors in a Row; Mass [kg]
N	Number of Elements, Number of Parameters
n	Number of Elements
n	Normal Vector
O(.)	O-Notation
P	Point
p(.)	anisotropic scattering phase function
Q	Heat Flow [W]
q	Heat Flux [W/m ²]
q	Heat Flux Vector [W/m ²]
r	Radius of Gershgorin Theorem [-]; Distance [m]
r	Directional Vector
S	Surface, Geometric Path [m]
T	Temperature [K]
t	Time [s]
u	Uncertainty [-]
UF	Uncertainty Factor [-]
w	Weighting Factor
x	Parameter
y	Result, Weighed Sum-Square Error
Γ	Interface
δ	Kronecker Delta [-]
Δ	Difference

ε	Emissivity [-]
λ	Eigenvalue
ν	Contour Vector Element
ρ	Reflectance [-]
σ	Stephan-Boltzmann Constant [W/m ² /K ⁴]
τ	Optical Depth [-]
θ	Angle
Φ, ϕ	Angle
ω	Uncertainty, Scattering Albedo, Solid Angle [Stearant]
$ \cdot $	Norm
$ \cdot $	Absolute Value

Subscripts:

a	Area
b	Boundary Heat Flux, black body
c	Combined
Cond	Conduction
Conv	Convection
e	Emissivity
f	Fluid
i,j	Index from Element i to j
imp	Imposed
k	Index of Element, Wavelength Band
o	Radiosity, Correction
p	Running Index
q	Heat Flux Specified; Running Index
Rad	Radiation

r,s,t	Running Index
T	Temperature Specified
λ	wavelength
∞	Infinity

Superscripts:

Cond	Conduction
Conv	Convection
e	Estimated
M	Number of Rows with Heat Flux Specified
Rad	Radiation
t	True
T	Transpose
'	Corrected, Current Time Step, Other direction

Heat flows and fluxes described in this thesis are written without the obligated dot such as q , Q , and b instead of \dot{q} , \dot{Q} , and \dot{b} , respectively.

1 Introduction

Thermal radiation as one of the modes of heat transfer is taken into account in the automotive industry with various levels of sophistication. One reason might be its inherent non-linear nature, which makes it less accessible to an engineer accustomed to linear models that depend on information about neighboring elements in a discretization scheme. Radiation affects geometry as long as two geometric entities see each other. While solution matrices of convection and conduction models are sparse, banded or blocked, and symmetric, this cannot be said of radiation matrices. Furthermore, classes in radiation are not offered as abundantly as in computational fluid dynamics (CFD), structural mechanics, or conduction. It is more common to treat radiation as part of a heat transfer class. The number of text books devoted to thermal radiation is also rather small compared to the aforementioned topics. Radiation has found wide acceptance in the space and building industries. Today the role of thermal radiation is also growing in the automotive industry.

1.1 Topical Overview

The aim of this thesis is to provide insight into recent developments in the automotive sector and to derive a method of reducing uncertainties in radiative simulation results that are possibly coupled with convection and conduction.

In the second chapter a survey of thermal radiation models is presented, various radiation solvers introduced, applications in the automotive industry cited, and the role of radiation in the product development cycle is described.

The third chapter introduces the radiation model most commonly used in this industry along with benchmarks for popular commercial tools.

Chapter four gives a brief description of requirements for coupling radiation with convection and conduction together with a proposed software architecture and a test case of industrial size.

In chapter five equations for a local sensitivity and uncertainty analysis are derived. This chapter contributes with this approach to the scientific and industrial communities.

Chapter six gives an outlook on possible future research on this topic followed by a list of literature in chapter seven and an appendix with tables and figures in chapter eight.

1.2 Impact

Research in this thesis has influenced the software industry that is serving thermal engineers. The publication of Rauch et al. (2007) together with corrected diagrams in Rauch et al. (2008a) spurred the need for improvement in view factor calculations for the common commercial software vendor. In these publications some benchmark problems related to accuracy, memory requirements, and run-time behavior were described along with the results of some codes. P+Z Engineering published in its THESEUS-FE Newsletter, Volume 2, October 2007, their response to Figure 3-37.

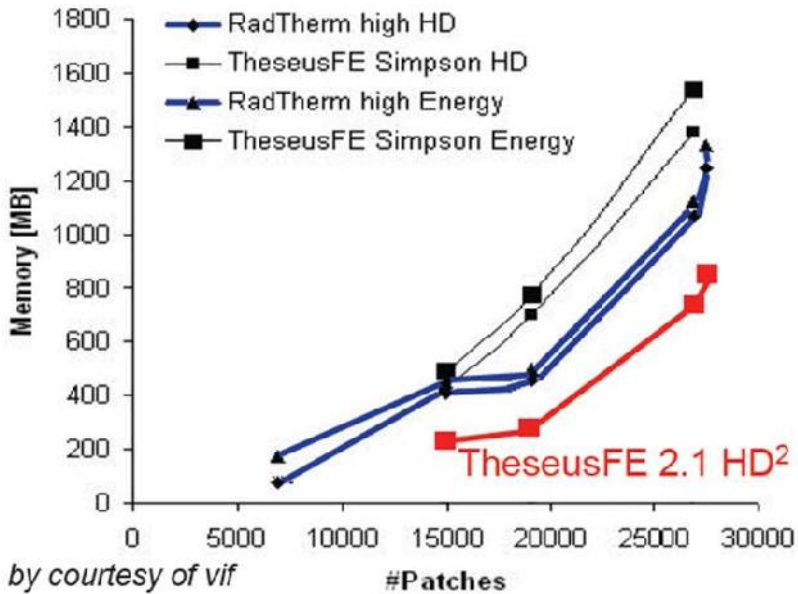


Figure 1-1: Memory requirements TheseusFE versus RadTherm by P+Z Engineering.

The benchmark ‘Coimbra’, which was used in this study, is described in chapter 3.5. The red curve represents the improvements in memory requirement compared to TheseusFE’s rival RadTherm (blue curves) and results of a previous version of TheseusFE. More striking is the claimed improvement in run-time in Figure 1-2 as compared to Figure 3-38. Though the claimed improvements were not validated by the author of this thesis they are plausible considering the discussion on data structures in chapter 3.4.

The author suggested researching this topic which lead to publications such as Fleischmann (2007).

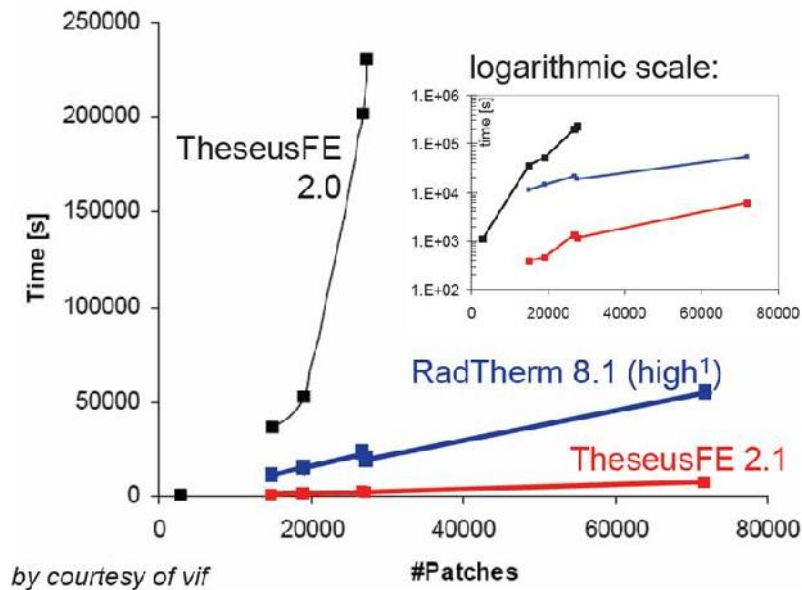


Figure 1-2: Run-time TheseusFE versus RadTherm by P+Z Engineering.

The developer of ESARAD asked for the published benchmarks. The results were not made known to the author. Whether the software passed the benchmarks satisfactorily or not, it can be claimed that some results of this thesis have not only influenced the automotive industry but also thermal software for the space industry.

As P+Z Engineering profited from an improved data structure its competitor Thermoanalytics Inc., developer of RadTherm, was influenced by the very first publication of the author on the topic of thermal radiation (Rauch et al., 2004). The research on radiation and human thermal comfort as mentioned in chapter 2.5 opened up a new field of application and a separately licensed module for their software and the two rivals accelerated their research on improving the predictability of a human thermal comfort model.

2 Thermal Radiation and the Automobile

2.1 Introduction

This chapter presents an overview of various thermal radiation models and introduces some important material properties related to thermal radiation. After listing some programs offering thermal radiation calculations, a range of applications in the automotive industry is shown. The product development process as described in the last section of this chapter demands reliable simulation results in order to minimize or even eliminate costly prototypes. To do so the uncertainties and sensitivities of the results must be known in order to make sound decisions by both management and the thermal engineer. The author became aware of this issue when investigating the impact of radiative heat fluxes on human thermal comfort. The magnitude of thermal radiation on some body parts depends strongly on the boundary conditions such as the position of the sun and the emissivity of the materials in the passenger compartment. This became the starting point of the quest for a method that can predict how important various parameters actually are on the simulation results.

2.2 Material Properties

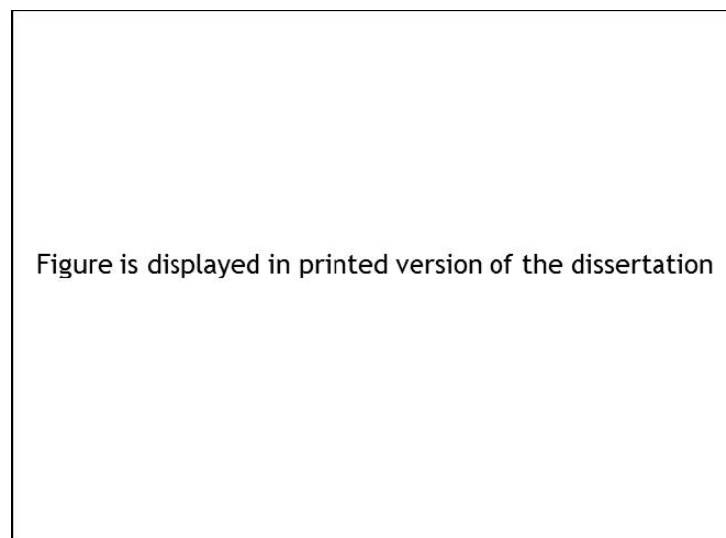


Figure 2-1: Thermal radiation in the electromagnetic spectrum. Reprinted from (Modest, 2003), Copyright © 2003, with permission from Elsevier Inc.

When talking about thermal radiation, the visible and near infrared range of the electromagnetic spectrum is meant.

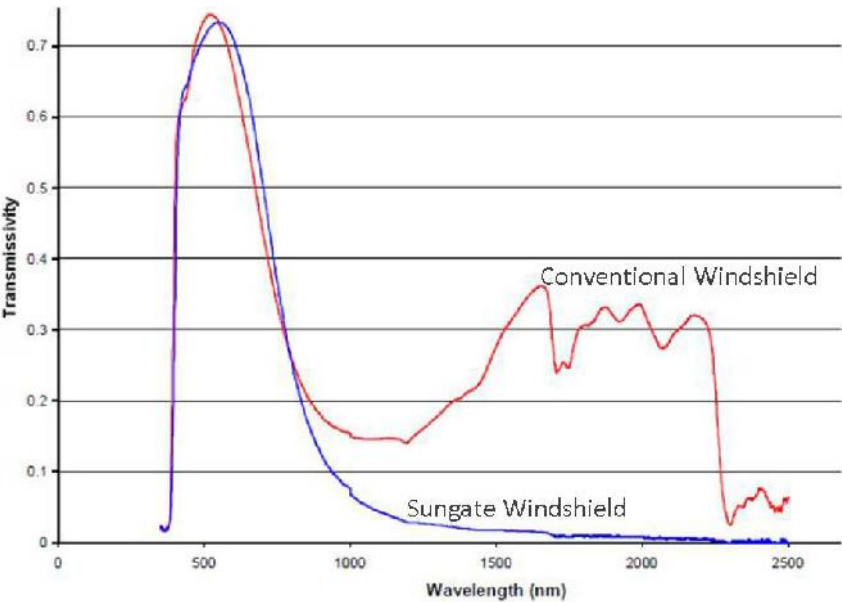


Figure 2-2: Transmissivity of two windshields (Farrington and Rugh, 2000).

Materials transmit and emit energy at different wavelengths in different ways. The greenhouse effect is explained by allowing glass to transmit solar energy. The energy is absorbed by opaque surfaces and transmitted at a different temperature with a different emissivity at different wavelengths. When the transmissivity at different wavelengths is very low, the energy will be either reflected or absorbed by the glass pane. This effect is desirable in greenhouses and solar thermal panels, but undesirable in the passenger compartment of an automobile. Therefore, windshields with a high reflectivity and a transmittance at the visible range due to regulatory requirements are desired in order to reduce heating, ventilating and air conditioning (HVAC) as described by Farrington and Rugh (2000).

Another important material property is reflectivity. A distinction is made between hemispherical and directional reflectivity.



Figure is displayed in printed version of the dissertation

Figure 2-3: Hemispherical directional spectral reflectivity of steel for various reflected directions (Vujić et al., 2006a). Copyright © 2006 Taylor & Francis Group.

Hemispherical means that the energy is summed over the entire hemisphere, whereas *directional* deals with just one direction. For reflectivities the notation holds that the first term refers to the incident energy and the second term the reflected energy. In Figure 2-3, for example, the energy over all incident directions is considered together with a specific direction of reflection over some wavelengths. The reflectivity in this example shows a strong dependence on angle. *Spectral* means that specific wavelengths are considered as opposed to *total*, where the property is summed over all wavelengths.



Figure is displayed in printed version of the dissertation

Figure 2-4: Normal spectral emissivity for Inconel X (Siegel and Howell, 2002). Copyright © 2002 Taylor & Francis Group.

The emissivity describes the fraction of energy the material is able to emit as radiation. The term ‘normal’ means that the energy is radiated in the normal direction from the surface. Figure 2-4 shows that the state of the surface has a great influence on this value. The same holds for temperature and the level of soiling on the surface. Hence, it is very important to get actual measurements of the investigated object instead of relying on textbook values. But how important are these properties for the simulation model? In chapter 5.3.2 a possible answer to this question is provided.

2.3 Thermal Radiation Models

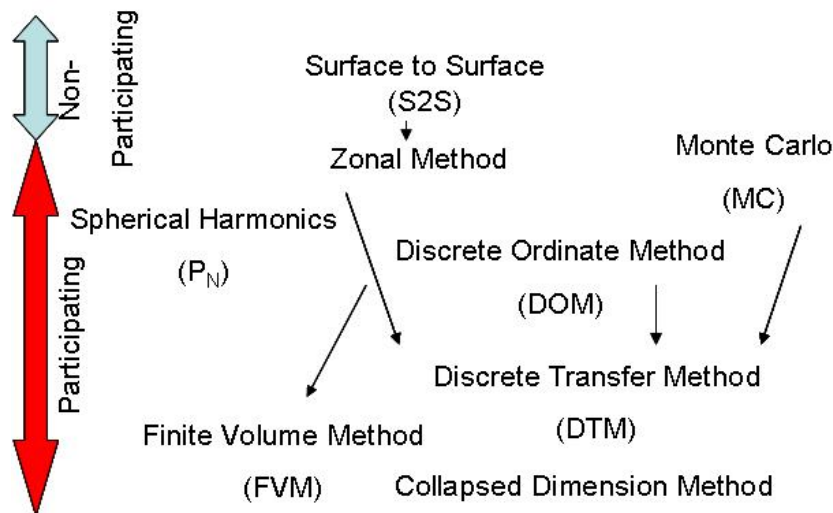


Figure 2-5: Thermal radiation models.

A basic distinction when dealing with thermal radiation exists in whether the fluid between the solids also participates in radiation. The surface to surface model has found wide acceptance in the automotive industry and is described in chapter 3. How thermal radiation passes through participating media must be defined in an equation. This fundamental equation is called the radiative transfer equation (RTE). In its differential form it looks the following way according to Mishra and Prasad (1998).

$$\frac{di(\vec{r}, \mu, w)}{d\vec{r}} + i(\vec{r}, \mu, w) = (1 - \tilde{S}_j) i_{j,b}(\vec{r}) + \left(\frac{\tilde{S}_j}{4f}\right) \int_{w=0}^{2f} \int_{\mu=0}^f i(\vec{r}, \mu', w') \times p((\mu', w') \rightarrow (\mu, w)) \sin \mu' d\mu' dw' \quad (\text{Eq. 2-1})$$

In this formula i is the intensity, τ_λ die optical depth of wavelength λ , θ and ϕ are angles of the ray, ω the scattering albedo, i_b the blackbody intensity, and p an anisotropic scattering phase function which describes the probability distribution of the energy scattered in the direction of the rays traversing the volume from all other directions '. The control volume for the RTE in differential form is depicted in the following figure.

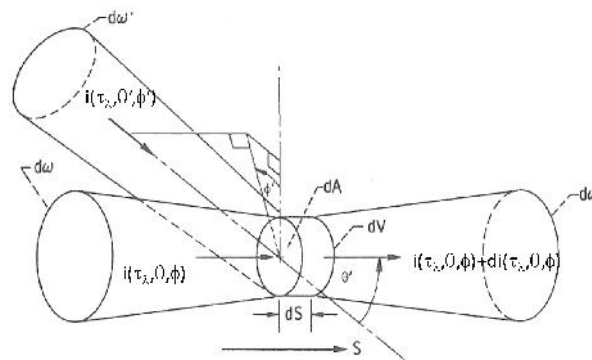


Figure 2-6: Control volume for the differential RTE.

This integro-differential equation is not only difficult to solve numerically, it involves other seven unknowns, namely the three space coordinates, optical depth, frequency, and two coordinates for photon travel. The right hand side (RHS) of the RTE is called the source function, which has the unknown intensity to be integrated over the angles. It is of little surprise that in the automotive industry, this equation is used only in the combustion chamber, the lighting system, and the exhaust system, if at all. Therefore, a very brief description will suffice.

The Zonal Method is a continuation of the surface to surface (STS, S2S) model and enjoys wide usage for radiative applications due to its nearly analytical solution. The difference to S2S is that view factors are not only calculated between surfaces but also between volumes. The model has a simple algebraic equation but is rather difficult to couple with conduction and convection because of the different mesh resolution requirements. Grid coupling schemes have been devised to solve this problem. Temperature dependent properties pose a challenge, as material properties are included in the exchange factors which must be recalculated.

The Monte Carlo (MC) method can be very accurate but also time-consuming. Photons are cast in random directions and their paths followed until all the energy has been absorbed according to the RTE. The path is determined randomly at each point of the medium. One disadvantage is that the solution always statistically fluctuates so that multiphysics coupling becomes difficult when error bounds of convergence are set too tightly, because they cannot be distinguished from statistical fluctuations.

The spherical harmonics method P_N approximates the angular dependent intensities of Eq. (2-1) by a series of functions of direction cosines. N signifies the number of terms in the series approximation. The result is a set of partial differential equations. Due to its complex implementation in 3D, this method is prone to errors in anisotropic conditions and for optically thin media for $N=1$.

The discrete ordinate method (DOM) discretizes the solid angles and expresses the integral term of the RTE with higher numerical integral schemes such as Gaussian quadrature. This equation can be spatially discretized by finite differences.

This method is adversely affected by the ray effect, which means that energy can be lost when a ray does not fall into one of the discrete ordinate directions. The method is also rather difficult to implement for complex geometries.

In the discrete transfer method (DTM) a ray is traced from one surface to another. The RTE is simplified by neglecting scattering and assuming a homogeneous control volume. Consequently, an algebraic equation is obtained. Calculated is the change of intensity within a control volume.

The incident heat flux is expressed by numerical quadrature. Via backtracking of rays that hit a surface, the intensities on the wall can be estimated.

The finite volume method (FVM) uses the same discretization procedures as for CFD and is thus well suited for CFD codes.

A method of great promise is the collapsed dimension method. It transfers all intensities normal to the two-dimensional solution plane and eliminates thus the solid angles, which makes this a fast method.

2.4 Thermal Radiation Solvers

Structural Mechanics	CFD	Buildings	Space	Automotive
ABAQUS	ACE+	BLAST	ESARAD	RadTherm
ANSYS	CFX	CLIM2000	RadCAD	TheseusFE
MSC.Nastran	Fidap	DEROB	SINDA	
TMG	FIRE	DOE 2.1	Thermica	
	FLUENT	SUNCAT	TRASYS	
	STAR CCM+	SUNCODE	TSS	
	PosRad	TRNSYS		
		View3D		

Table 2-1: Thermal radiation solvers.

The above table provides a short overview of thermal radiation solvers or special modules in codes written for other simulations in physics. Structural mechanics codes provide a radiation model, usually S2S, in order to calculate thermal stress. CFD codes offer models usually suited for participating media. PosRad is a module for StarCD.

In chapter 3.5 an example is shown where a surface to surface model of a CFD code is benchmarked against a specialized code which shows that a specialized code usually offers more efficient implementations. In the building industry thermal comfort calculation with its accompanying radiation analysis has a longstanding tradition. But these codes are written for simple geometries with few faces. They include a solar model which is often the primary source of heat in a building. In the outer space environment, thermal radiation is the sole mode of heat transfer. The codes use STS or the Monte Carlo method. Some codes were written by space agencies in the 1960s. These legacy codes tend to be rather slow.

To the author's knowledge there are two codes with the automotive industry in mind. They seek to offer fast results for industrial meshes. They offer manual coupling to CFD results and can calculate conduction.

RadTherm was written for military application and then taken over by Ford. Presently, Thermoanalytics Inc. has the rights on this code. RadThermIR is based on RadTherm with the addition of the postprocessing of wavelength dependent materials. Its surface to surface model is based on a hemisphere method with finite

difference discretization. The reader is referred to chapter 3.3.1 for a description of the various numerical methods for view factor calculations in the surface to surface model. The wall temperatures are calculated in two wave bands when the solar model is used. In this way, the greenhouse effect can be modeled.

One competitive commercial product is TheseusFE by P+Z Engineering. This code is based on numerical integration of view factors in the STS model and uses a finite element discretization. It can handle volume meshes in addition to surface meshes commonly employed for radiative analysis in non-participating media. Originally, it was developed by BMW and includes several thermal comfort models.

In this paper RadThermIR was used by the author. As a benchmark TheseusFE was briefly included.

This chapter has provided only a short overview on radiation solvers both commercial and non-commercial codes. It is assumed that there are other industrial codes developed and used internally such as is the case for AURA by AUDI AG.

2.5 Thermal Radiation in the Automotive Industry

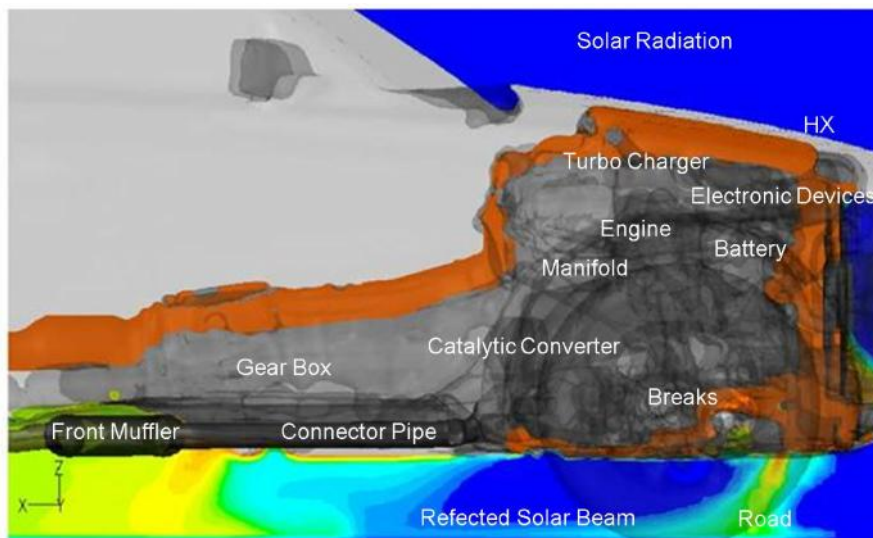


Figure 2-7: Heat sources in the underhood.

Figure 2-7 shows typical components that emit heat in an automobile. The most obvious group of components is the exhaust system due to high temperatures.

In the combustion chamber carbon dioxide and water are the main chemical compounds that participate in thermal radiation.

Therefore, one of the models described in section 2.3 for participating media ought to be employed. The exhaust gas passes through the manifolds, the catalytic converter, a possible particulate filter, a pipe system and the muffler into the environment. Sometimes a simplification is sought and the exhaust gas is treated as non-participating.

Steinkilberg (2006), Arvin Meritor, performed simulations on the conjugate heat transfer of manifolds. For thermal-shock cycle simulations he showed that transient convective heat transfer coefficients are required for more accurate wall temperatures.

He also employed an in-house developed model for a diesel particulate filter (DPF). The model is necessary, as the gas passes through a porosity thereby changing its temperature. A changing gas temperature has an effect on the surface temperature of the DPF.

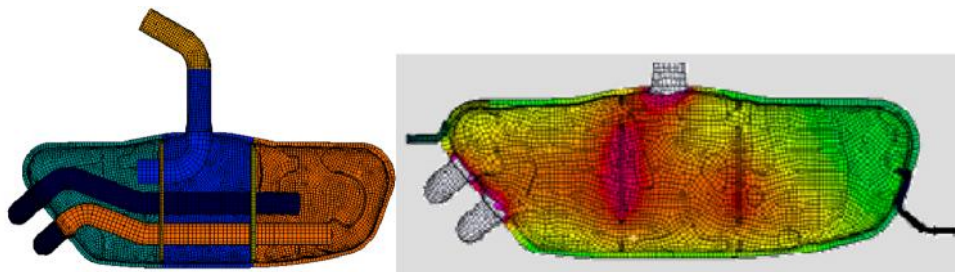


Figure 2-8: Muffler internals (left) and simulated surface temperatures (right) (Herrera and Lund, 2007).

Herrera and Lund (2007), Volkswagen, demonstrated how including the internals of a muffler improved the accuracy of surface temperature calculations.

Frémond (2008), Volvo 3P, demonstrated how temperatures from a thermal image are mapped onto a surface mesh in RadTherm. The mapped temperatures serve as a boundary condition for an underhood simulation. This method is usually applied for components that are difficult to model because of chemical reactions and porous media.

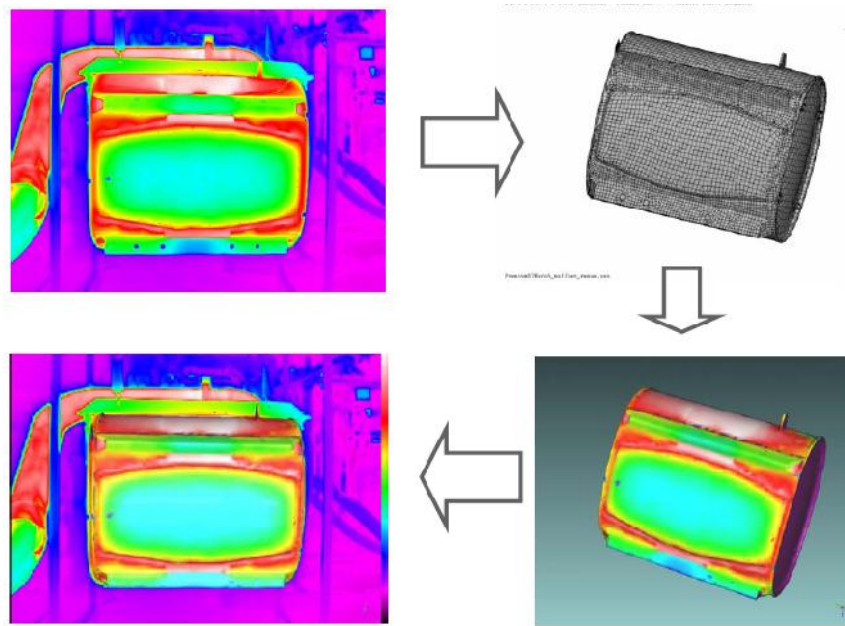


Figure 2-9: Mapping of surface temperatures from IR Thermography (Frémond, 2008).

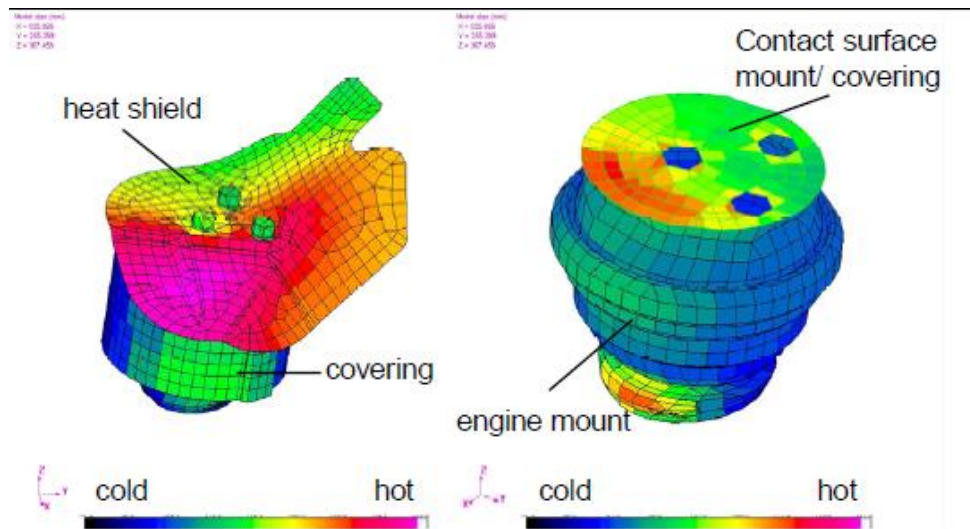


Figure 2-10: Engine mount temperatures (Weidmann et al., 2004).

The purpose of conjugate heat transfer calculations is to find out the thermal load on heat sensitive components. One such component is the rubber mounting of engines. Weidmann et al. (2004) described protective devices which keep the rubber within operating temperatures. This work is interesting because it shows a way of measuring emissivity coefficients in the presence of soiling.

Another rubber part is the hardy disc on the steering shaft. Moshammer (2006) presented results for various manifold configurations, heat shields and convection rates in order to determine the configuration that promises the lowest temperature on the hardy disc, which is denoted as ‘rubber element’ in Figure 2-11.

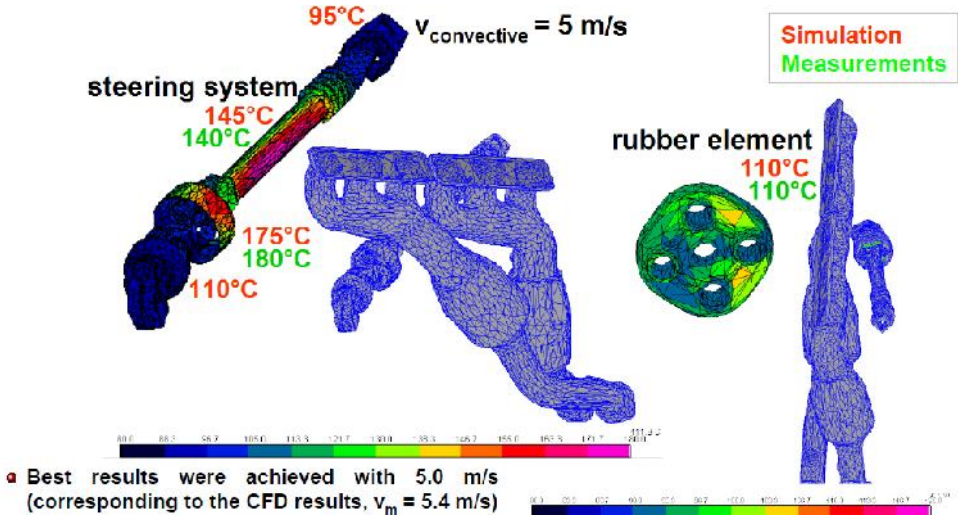


Figure 2-11: Hardy disc temperatures (Moshammer, 2006).

Klaus et al. (2004), Adam Opel, investigated the temperature of the power cable of the compressor of a pressurized proton exchange membrane (PEM) fuel cell and determined appropriate countermeasures.

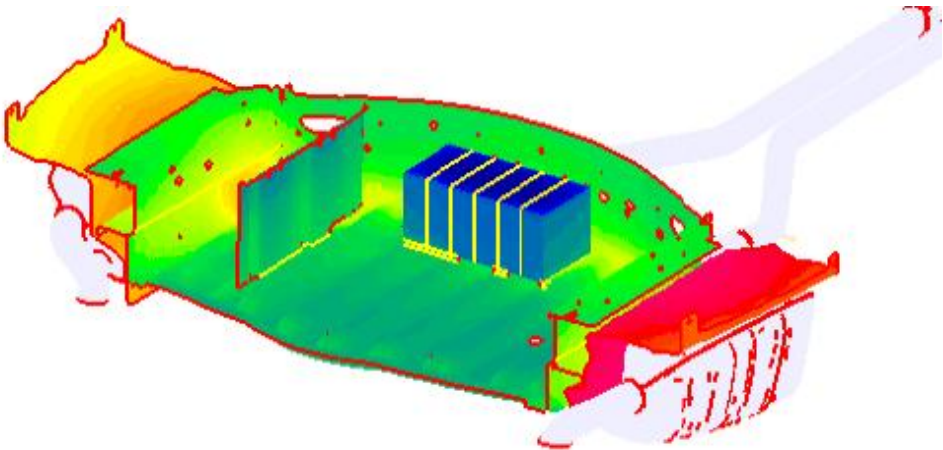


Figure 2-12: Battery temperatures in the trunk of a car (Michel et al., 2006).

The battery is a component that needs to be protected from heat in order to extend its life time and maximize power output. Michel et al. (2006) for Daimler investigated thermal soak of a conventional battery in a trunk which was affected by waste heat from the exhaust system.

Jansen (2008), Jaguar, investigated the noise emission of the compressor of the air conditioning (AC) cycle. When the temperature of the refrigerant increases, the compressor has to perform and more noise is radiated.

By performing a thermal analysis the optimal positions and thicknesses for line insulations can be determined.

Jansen, (2004) also calculated the temperature on the disc brake after a cycle of 25 brakings by calculating the dissipated heat during braking and determining convective heat transfer coefficients with CFD.

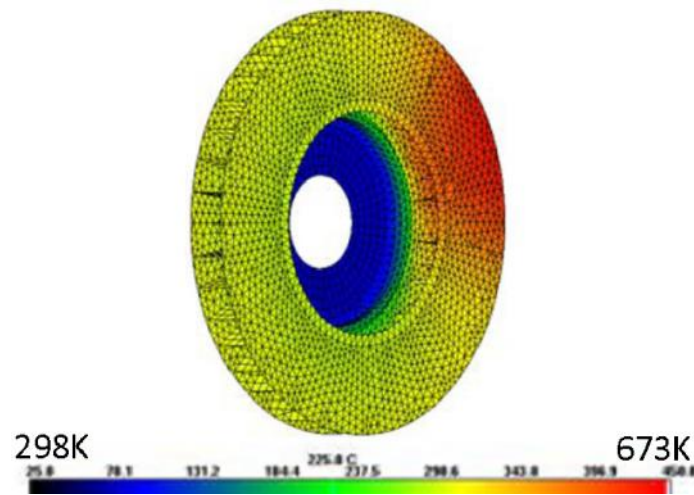


Figure 2-13: Disc brake cooling (Jansen, 2004).

When cars race, some energy is transferred to the road. This is particularly acute in a Formula One race. The right choice of tires is determined by the road conditions. The temperature of the Silverstone racetrack was calculated considering the solar soak (Jussila, 2007).



Figure 2-14: Temperature of Silverstone track (Jussila, 2007).

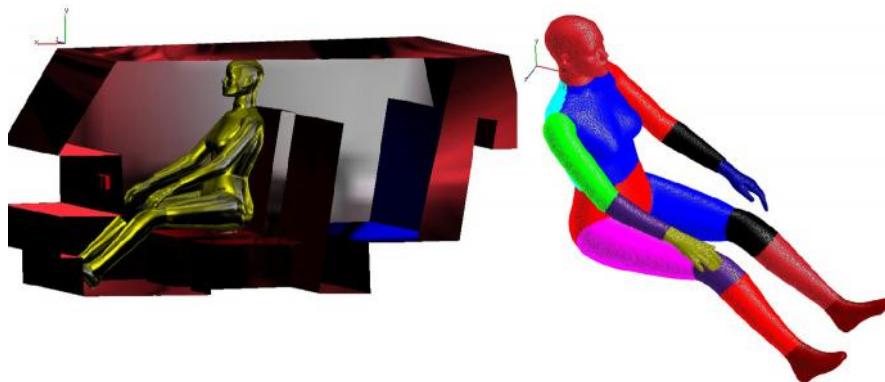


Figure 2-15: Coimbra box with dummy of 16 segments (Rauch et al., 2004).

Another issue in automobiles is estimating human thermal comfort. This topic has received much attention and is worth mentioning in the context of thermal radiation, as the human body is sensitive to radiative heat fluxes even at ambient temperatures. The author (Rauch et al., 2004) performed a simulation with a simplified cabin model as shown in Figure 2-15. The naked dummy was supplied with heat at 16 sections imitating the human metabolism.

With air conditioning switched on, a coupled CFD and thermal radiation simulation was conducted.

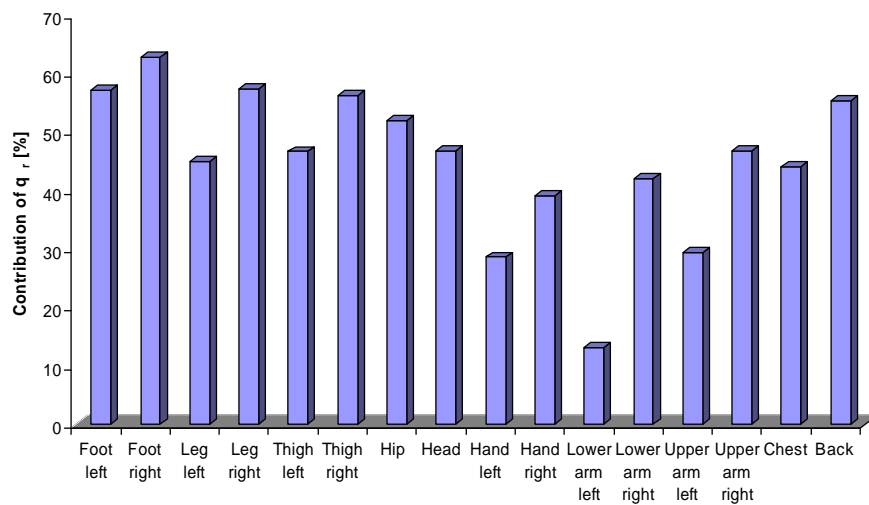


Figure 2-16: Share of radiative heat flux for manikin of 16 segments (Rauch et al., 2004).

The results show that even at low temperature levels excluding solar radiation the share of thermal radiation is quite high. Only the lower left arm had a modest share of radiation because this body segment was exposed to a strong HVAC air stream of 6.36 m/s with 290.65 K.

With known heat fluxes, thermal comfort indices can be evaluated. Clothing protects the body from incoming radiation. As a result a microclimate between body and clothing develops.

Bader et al. (2007), Volkswagen, demonstrated the use of CFD and thermal radiation calculation for defogging issues of the lighting system. It is necessary to know the surface temperatures to locate areas where water vapor condensates.

Kumar et al. (2010), TATA, predicted the top hose temperature, which is the coolant inlet temperature for the radiator, by a coupled CFD, thermal radiation, and 1D power train cooling simulation.

Jussila (2008) calculated the surface temperatures for the paint curing process. In the car manufacturing process, the development of a “skin” of paint is desired before the chassis enters the convective zone of the oven. There, wet paint would be blown out, decreasing the protective layer of the paint layer.

Cold spots such as welding spots or foams delay the formation of the “skin” in the infrared heating zone of the oven. By performing a thermal radiation analysis the transient behavior of the car body can be predicted. The speed of the car moving through the paint oven and the required heating power and oven geometry can be optimized.

2.6 Thermal Radiation in the Product Development Process

Thermal radiation simulation is receiving increased attention in the automotive industries due to the need to reduce the amount of prototypes. An increase in the product portfolio and a stricter emissions legislation of EURO 5/6 can shorten the product development time (Frémond, 2008).

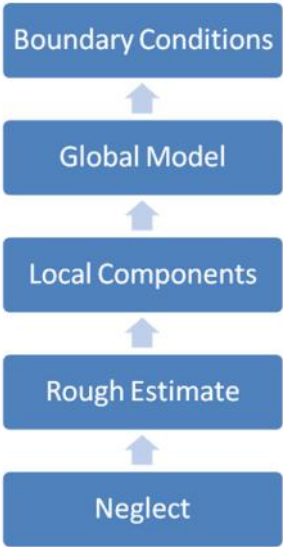


Figure 2-17: Level of awareness for thermal radiation.

The resources an organization is willing to invest on thermal radiation depends on the profit its application promises and the level of knowledge in that subject. It happens that companies do not perform a radiation analysis because decision makers have not heard much about this heat transfer mode or believe that radiation plays no significant role in their process below a certain temperature level.

Once the need for radiation has been recognized, rough estimates can be made. These can be simplified correlations or charts.

The author of this thesis created a simple tool that incorporated an empirical relation for convection, conduction, and a simplified radiation model for a pipe to simulate a turbo charger. At this level companies are not prepared to invest a lot of resources on this topic. The next development step is the simulation of local components. A component that requires a certain operating temperature range is modeled together with a possible heat source or sink. The rest of the system is neglected. At this stage a company either outsources these calculations or starts buying licenses and training a small group of employees which usually do these calculations along with many other computer-aided engineering (CAE) activities.

Employing a global model simulates the entire system and identifies the impact of all components. This requires highly skilled engineers and an established work flow. At this stage multiphysics simulations are an integral part of the development process.

Finally, as skilled engineers become aware of the shortcomings of their global models as boundary conditions are usually not available, the material properties are measured instead of relying on text book values. At this stage the experimental department not only provides validation measurements, but also begins designing experiments together with the simulation department to provide boundary conditions for difficult to simulate zones, such as the internal combustion engine or catalytic converters. The simulation engineer needs to understand the limitations of the models making an immersion into the theory of radiation necessary.

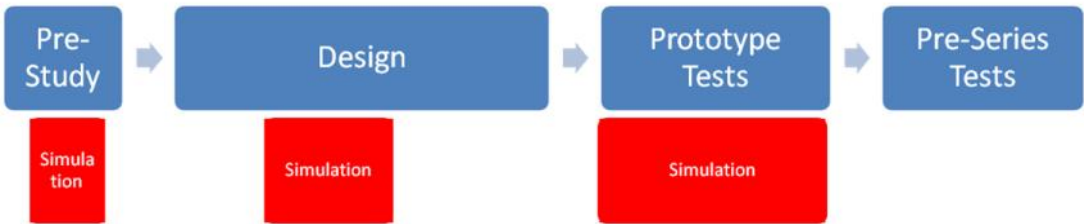


Figure 2-18: Basic development process.

Figure 2-18 refers to a typical development process when confidence in simulation is unsatisfactory. In the pre-study phase basic concepts are investigated and simplified relations and charts will do. In the design phase the simulation of fluid flow and heat transfer can begin when the surface topology of the car is available from computer-aided design (CAD) data.

But unless a prototype is available simulation results are not valuable. Only experiments will provide boundary conditions and validate simulations. The advantage of simulation is not evident at this stage. The situation is even more complicated as this process is highly iterative, for there are many conflicting design requirements.

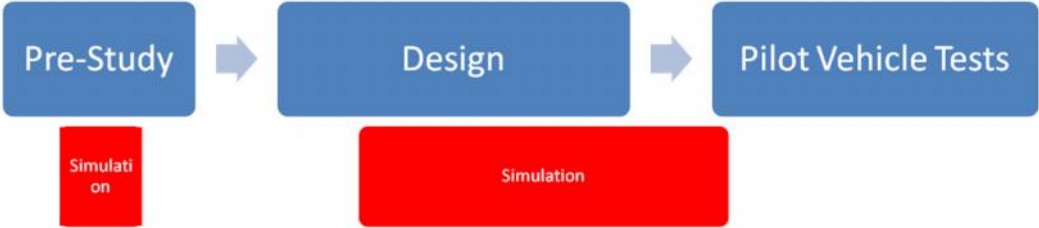


Figure 2-19: Advanced development process.

When the confidence in simulation results is high, a prototype might be omitted, as far as regulation permits, and simulations provide valuable information in the repetitive design process. Even production issues can be incorporated as indicated by the term ‘pilot vehicle tests’ in Figure 2-19. Of course, thermal radiation is only one part in the process but it must be considered in order to shorten development times. For this advanced development process to work, it is not only important to have a thorough knowledge of radiation and multiphysics coupling but the cooperation between the various departments within the company is essential.

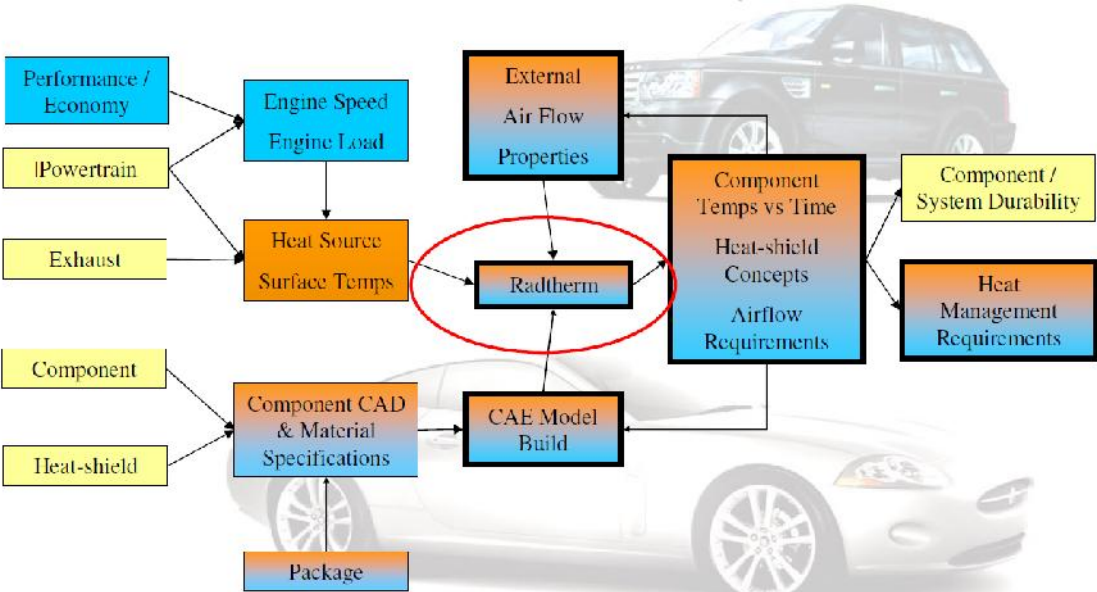


Figure 2-20: Heat protection activity flow at Jaguar/Land Rover (Jansen, 2007).

When all the requirements of various components are available, target heat loads and temperatures can be specified and the model designed. Then the model can be iteratively coupled with airflow requirements and simulated in a thermal solver, such as RadTherm. It is then passed on to other departments to check heat management requirements. Investing amply in communication is essential for minimizing interpersonal friction and reducing iteration cycles.

Sensing the need for adequate and timely simulation results, the question remains to be answered, how one might reduce uncertainties in multiphysics simulations.

3 Surface-to-Surface Model

3.1 Introduction

The surface-to-surface (S2S) model is the oldest model known. Its derivation began in the early 20th century. This model is introduced in the following section. One important parameter is the view factor with methods shown for improving its accuracy and more rapid calculation. This chapter ends with benchmarks on some programs' accuracy and speed of view factor calculations. It was during these benchmark runs when the author seriously challenged the need to calculate view factors up to a certain number of digits. The assumption arouses that view factors need a level of accuracy suited to the boundary conditions. Knowing the parameters involved in the model allows one to estimate their respective influences on the results.

3.2 Energy Balance

The net-radiation formulation for enclosures with finite diffuse-gray areas is shown because this formulation is widely used such as in the solver RadThermIR. The derivation can be read in Siegel and Howell (2002) and shall not be reproduced here. It is sufficient to say that the derivation stems from first-principle thermodynamics in an enclosure.

$$\sum_{j=1}^N \left[\frac{u_{kj}}{v_j} - F_{kj} \frac{1-v_j}{v_j} \right] \frac{Q_j}{A_j} = \sum_{j=1}^N F_{kj} \sigma (T_k^4 - T_j^4) \quad (\text{Eq. 3-1})$$

Q_j is the net heat flow from the outside of face j , A_j the area of j , F_{kj} the form factor from k to j , δ_{kj} the Kronecker delta, σ the Stefan-Boltzmann constant, T the surface temperature, N the number of faces, and ε_j the emissivity. The net heat flow is the amount of energy required to keep a specified temperature. There are two possible boundary conditions. Either the temperature of the face is given, or the heat flow is specified. Correspondingly, the equation above has to be reformulated. In thermal engineering it is common to fill a matrix and solve for all unknowns. The emissivity is not allowed to become zero, as this would create a singularity. The set of linear equations can be solved for T^4 or Q .

When temperature dependent properties are introduced the set of equations becomes non-linear. But when initial temperatures are estimated, one can simply solve the equations iteratively until the estimated temperatures coincide within a tolerance with the calculated temperatures. It should be noted that from the system outgoing radiation is positive contrary to the thermodynamic sign convention.

For the thermal engineer, the other heat transfer modes and transient behavior must be investigated, too. According to Thermoanalytics (2003) the equation is expanded the following way by first rewriting Eq. (3-1):

$$Q_k = \frac{v_k A_k}{1 - F_{kk}(1 - v_k)} \left[\sum_{j=1}^N F_{kj} (T_k^4 - T_j^4) + \sum_{j=1}^N \left[(1 - u_{kj}) F_{kj} \frac{1 - v_j}{v_j} \right] \frac{Q_j}{A_j} \right] \quad (\text{Eq. 3-2})$$

Then one can add:

$$Q_k = Q_{imp,k} + h_k (T_f - T_k) + \sum_{j=1}^{N_{Cond}} \left(-\frac{k_{kj} A_{kj}}{l_{kj}} (T_k - T_j) \right) - m_k c_{p,k} \frac{dT_k}{dt} \quad (\text{Eq. 3-3})$$

T_f represents the fluid temperature, h_k the convective heat transfer coefficient, k_{kj} the thermal conductivity, which in this study is presumed to be independent of temperature, A_{kj} the area bordering a neighboring thermal element, l_{kj} the distance between two thermal node centers, $q_{imp,k}$ the imposed heat, $c_{p,k}$ the specific heat capacity, m_k the mass, t time, and N_{Cond} the number of thermally conducting neighbors. In this way radiation is coupled to convection and conduction but has T and T^4 as unknowns. A popular way to solve the last two equations is by linearization. For example one can use the Crank-Nicholson scheme for discretizing the temperature derivative in time and solve for the temperature of the current time step T' and creating conductors C for Radiation Rad, Conduction Cond, and Convection Conv:

$$T'_k = \frac{\frac{2m_k c_{p,k} T_k}{\Delta t} + \sum_{j=1}^N C_{kj}^{Rad} (T_j + T'_j - T_k) + \sum_{j=1}^{N_{Cond}} C_{kj}^{Cond} (T_j + T'_j - T_k) + C_k^{Conv} (T_j + T'_j - T_k)}{\frac{2m_k c_{p,k}}{\Delta t} + \sum_{j=1}^N C_{kj}^{Rad} + \sum_{j=1}^{N_{Cond}} C_{kj}^{Cond} + C_k^{Conv}}$$

$$Q_{imp,k} + Q'_{imp,k} - \frac{2v_k A_k}{1 - F_{kk}(1 - v_k)} \sum_{j=1}^N \left[(1 - u_{kj}) F_{kj} \frac{1 - v_j}{v_j} \right] \frac{Q_j}{A_j} + \frac{2m_k c_{p,k}}{\Delta t} + \sum_{j=1}^N C_{kj}^{Rad} + \sum_{j=1}^{N_{Cond}} C_{kj}^{Cond} + C_k^{Conv} \quad (\text{Eq. 3-4})$$

$$C_{kj}^{Rad} = \frac{v_k A_k}{1 - F_{kk}(1 - v_k)} \dagger F_{kj} (T_k^2 + T_j^2) (T_k + T_j) \quad (\text{Eq. 3-5})$$

$$C_{kj}^{Cond} = \frac{k_{kj} A_{kj}}{l_{kj}} \quad (\text{Eq. 3-6})$$

$$C_k^{Conv} = h_k A_k \quad (\text{Eq. 3-7})$$

In order to calculate the net heat flow the following equation is used:

$$Q_k = \frac{1}{2} \sum_{j=1}^N C_{kj}^{Rad} (T_j + T'_j - T_k - T'_k) + \frac{v_k A_k}{1 - F_{kk}(1 - v_k)} \sum_{j=1}^N \left[(1 - u_{kj}) F_{kj} \frac{1 - v_j}{v_j} \right] \frac{Q_j}{A_j} \quad (\text{Eq. 3-8})$$

An alternative way of calculating T and Q is by using radiosity q_o . This parameter represents the heat flux emitted and reflected from a face and is actually measured by infrared (IR) detectors.

$$q_{o,k} - \frac{1}{A_k} \sum_{j=1}^N A_j q_{o,j} F_{jk} = q_k \quad (\text{Eq. 3-9})$$

This relation describes the net radiative flux q_k as a function of radiosity $q_{o,k}$, view factor F_{jk} , and area A_k for all N faces and states the first law of thermodynamics for radiation. The relationship between radiosity and temperature is given as:

$$q_{o,k} - (1 - v_k) \frac{1}{A_k} \sum_{j=1}^N A_j q_{o,j} F_{jk} = v_k \dagger T_k^4 \quad (\text{Eq. 3-10})$$

It actually serves as definition for the radiosity. Due to its simplicity these two equations will play a prominent role in chapter 5.

Goral et al. (1984) was the first to use the radiosity concept in computer graphics:

$$\sum_{j=1}^N (u_{kj} - I_{j \dots k} F_{kj}) = I_k \quad (\text{Eq. 3-11})$$

Instead of heat fluxes light intensity I and reflectivity ρ_k are used. Since temperature does not appear there are no temperature dependant properties. As a boundary condition intensity is required as a light source. Eq. (3-11) is always linear. Therefore, publications on solving for the balances in computer graphics cannot be applied for conjugate heat transfer problems. But there is extensive research in the field of computer graphics on calculating form factors as efficiently as possible.

3.3 View Factors

A fundamental task of filling the solution matrix of the S2S model is to compute the form factors F_{ij} . They are also called view factor, configuration factor, shape factor, or angle factor. View factors have been the subject of research for many years. To the author of this thesis, the first known researcher who elaborated on a closed form factor derivation between two rectangles sharing a common edge with an angle of 90 degrees was Lambert and was cited in Schröder and Hanrahan (1993):

“Although this task appears very simple its solution is considerably more knotted than one would expect. For it would be very easy to write down the differential expression of fourth order, which one would need to integrate four fold; but the highly laborious computation would fill even the most patient with disgust and drive them away from the task. The only simplification which I was able to achieve was to reduce the expression to a second order differential, using the above theorems [formula for differential surface element to polygon form factor], with which I was able to perform the computation.”

The following study shall give an overview of the methods to calculate and correct view factors.

3.3.1 Taxonomy of View Factor Estimation

The view factor is defined as the fraction of energy leaving a surface that arrives at the receiver surface. To derive the relation two infinitesimal elements 1 and 2 exchange energy as depicted in Figure 3-1. The differential solid angle $d\omega_1$ is defined as:

$$d\check{S}_1 = \frac{dA_2 \cos \theta_2}{r^2} \quad (\text{Eq. 3-12})$$

With r as the distance between the two differential areas, A area, and θ as angle between normal and connecting line. The total energy Q leaving A_1 is:

$$d^2Q_{d1-d2} = i_1 dA_1 \cos \theta_1 d\check{S}_1 \quad (\text{Eq. 3-13})$$

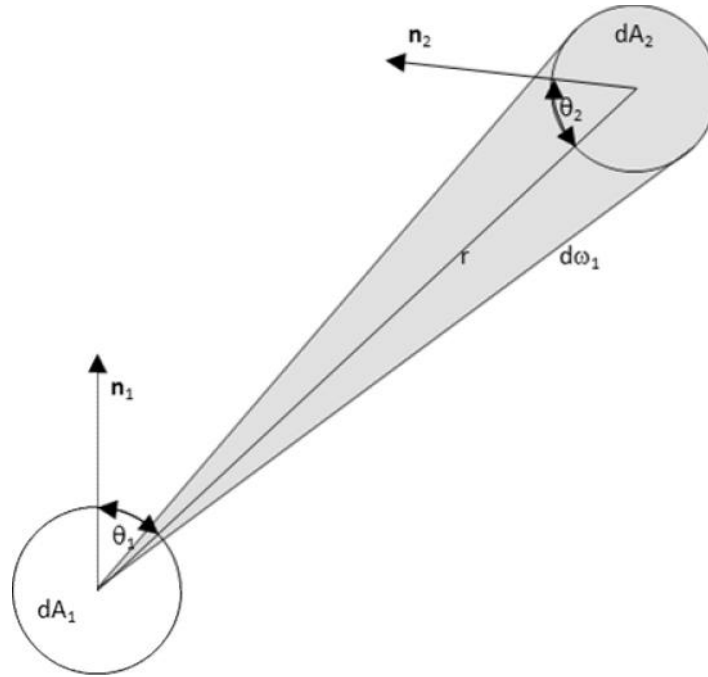


Figure 3-1: Differential solid angle.

Substituting the solid angle with i as intensity:

$$d^2Q_{d1-d2} = \frac{i_1 dA_1 \cos \theta_1 dA_2 \cos \theta_2}{r^2} \quad (\text{Eq. 3-14})$$

The same can be written for area 2. Using the definition of the view factor and assuming a Lambert surface, i.e. the energy is emitted and reflected diffusely, one can write:

$$dF_{d1-d2} = \frac{i_1 dA_1 \cos \theta_1 dA_2 \cos \theta_2}{i_1 r^2 f dA_1} = \frac{\cos \theta_1 \cos \theta_2}{r^2 f} dA_2 \quad (\text{Eq. 3-15})$$

The configuration factor between a differential and finite area requires integration:

$$F_{d1-2} = \int_{A_2} \frac{\cos \theta_1 \cos \theta_2}{r^2 f} dA_2 \quad (\text{Eq. 3-16})$$

Finally, the form factor between two finite areas is:

$$F_{1-2} = \frac{1}{A_1 f} \int_{A_1} \int_{A_2} \frac{\cos \theta_1 \cos \theta_2}{r^2} dA_2 dA_1 \quad (\text{Eq. 3-17})$$

Cohen and Wallace (1993) provide an overview on methods of form factor calculation that are shown in Figure 3-2.

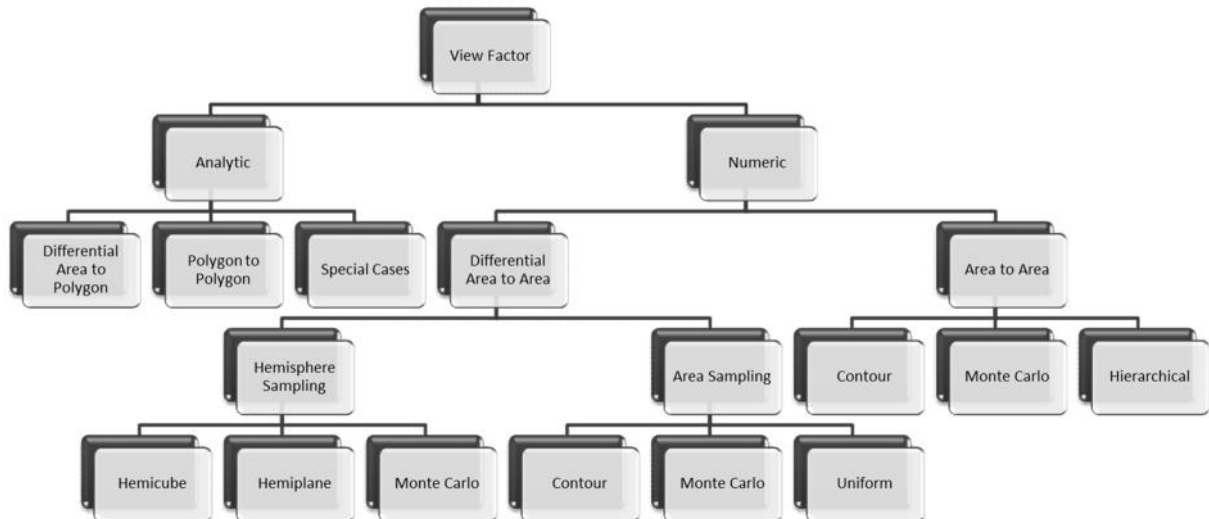


Figure 3-2: Form factor taxonomy according to Cohen and Wallace (1993).

The methods can be divided into how many integrals must be solved. Another distinction is whether a form factor is calculated between two individual faces or all faces at once. First the situation without obstructions shall be considered.

The method to solve Eq. (3-17) is called double area integration (2AI). In order to speed-up the calculation the cosines do not need to be calculated. Instead, they are replaced by a product of the normal vector \mathbf{n} and the vector connecting the centers between the finite areas \mathbf{r} . When expressing the integrals as summations of N subdivided edges it can be written that:

$$F_{1-2} \approx \frac{-1}{A_1 f} \sum_{i=1}^{N_1} \sum_{j=1}^{N_2} \frac{(\mathbf{r} \cdot \mathbf{n}_1)(\mathbf{r} \cdot \mathbf{n}_2)}{(\mathbf{r} \cdot \mathbf{r})^2} \Delta A_i \Delta A_j \quad (\text{Eq. 3-18})$$

Shapiro (1985) describes the operation count as $114N^4 + 86N^2$ which amounts to $O(N^4)$ in the big O-notation for run-time complexity, which renders this method rather unsuitable for large scale problems.

When applying Stokes' theorem the area integrals are converted into line integrals where C is the contour and ϵ the contour vector differential.

$$F_{1-2} = \frac{1}{2A_1 f} \oint_{C_1} \oint_{C_2} \ln(r) d_1 d_2 \quad (\text{Eq. 3-19})$$

When dividing the contours into E segments with Φ as the angle between N contour vector elements it can be seen that:

$$F_{1-2} \approx \frac{1}{4A_1 f} \sum_{p=1}^{E_1} \sum_{q=1}^{E_2} \cos(\Phi_{pq}) \sum_{i=1}^{N_1} \sum_{j=1}^{N_2} \ln(\mathbf{r} \cdot \mathbf{r}) \Delta \epsilon_i \Delta \epsilon_j \quad (\text{Eq. 3-20})$$

Shapiro (1985) describes the time complexity as $464N^2 + 24N$ which amounts to $O(N^2)$. The numerical integration is skipped when the angle Φ is zero, which happens to be at two perpendicular edges. In Figure 3-2 this method corresponds to contour integration between two areas and is called double line integration (2LI).

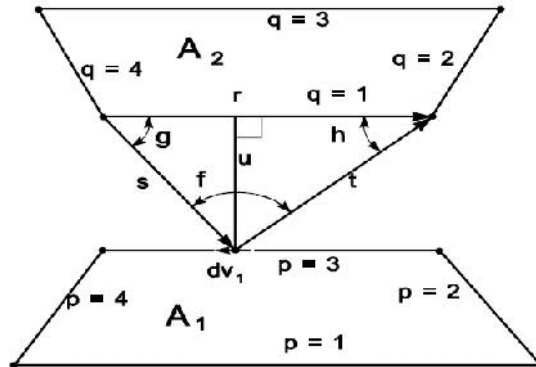


Figure 3-3: Nomenclature for single line integration (1LI) (Walton, 2002).

When one of the contour integrals is solved analytically the following relation is obtained by using the nomenclature in Figure 3-3.

$$F_{1-2} = \frac{1}{2A_1 f} \sum_{p=1}^{E_1} \sum_{q=1}^{E_2} \cos(\Phi_{pq}) \oint_{C_1} (t \cos(h) \ln(t) + s \cos(g) \ln(s) + uf - r) d_1 \quad (\text{Eq. 3-21})$$

Shapiro (1985) counted $864N+288$ operations for the N contour vector segments. This still leads to a run-time complexity of $O(N^2)$ for the single line integration (1LI), though in general, the run-time behavior is linear. In Cohens' taxonomy, this method corresponds to a contour method for area sampling. The time complexity suggests using 1LI. Unfortunately, a singularity occurs when two faces are adjacent. Therefore, a different method needs to be applied in that situation.

There are studies on formulating analytic expressions. Walton (2002) reproduces a closed form solution for a differential element to polygon with the nomenclature of Figure 3-4:

$$F_{1-2} = \frac{1}{2A_1f} \int_{A_2} \mathbf{g}_i \cdot \mathbf{n}_1 \quad (\text{Eq. 3-22})$$

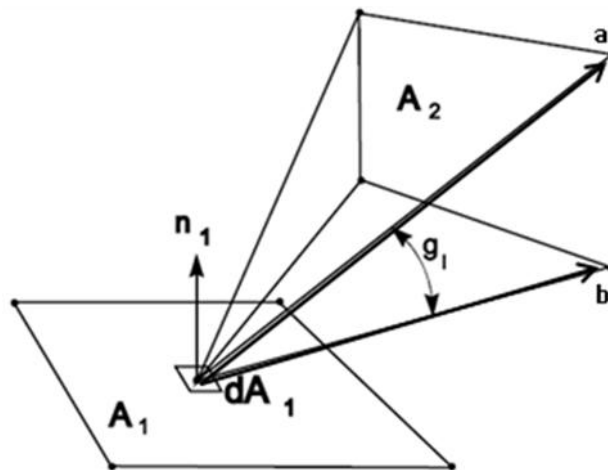


Figure 3-4: Nomenclature for single area integration (1AI) (Walton, 2002).

The magnitude of vector \mathbf{g}_i equals the angle g and the direction is outward of the plane passing through the vectors \mathbf{a} and \mathbf{b} . With \mathbf{c} as the cross product from \mathbf{a} and \mathbf{b} , e the length of \mathbf{c} , d as the dot product of \mathbf{a} and \mathbf{b} , and reformulation in order to avoid some singularities the following simplification can be made:

$$F_{1-2} \approx \frac{1}{2A_1f} \sum_{j=1}^{N_2} \sum_{i=1}^{E_2} \left(\frac{(\mathbf{c}_i \cdot \mathbf{n}_1)}{e_i} \left[\frac{f}{2} - \tan^{-1} \left(\frac{d_i}{e_i} \right) \right] \right) \Delta A_j \quad (\text{Eq. 3-23})$$

Walton (2002) describes this single line integration (1AI) as of the order of $4N^2$, thus being slightly faster than double line integration. This method would best fit to uniform area sampling.

In area sampling in Cohen’s taxonomy, the Monte Carlo method would shoot rays in a random direction and the number of rays hitting a face divided by the number of rays shot would be the form factor. The same applies to the area to area view factor for Monte Carlo with the addition that the starting point of the rays can now vary as well. Hierarchical area to area view factors are calculated by first dividing a face, calculating the view factors for each individual sub-face, and then summing these view factors up.

$$F_{pj} = \frac{1}{A_p} \sum_{i=1}^N A_i F_{ij} \tag{Eq. 3-24}$$

A_p is the area of the original patch and N the number of sub-faces in that patch.

Analytical form factors have been mentioned for single area integration. There are collections of analytically derived view factors in standard text books on thermal radiation such as Siegel and Howell (2002) and Modest (2003). Howell (2010) has published a collection on the internet which continuously undergoes correction. The collections are usually divided into view factors between area to area, differential area to area, and special cases. Schröder and Hanrahan (1993; 1993a) have actually derived an analytic relation between two arbitrarily oriented polygons. In certain situations it uses a dilogarithm which slows down the algorithm significantly. When using the aforementioned methods of view factor calculation, namely 2AI, 1AI, 2LI, and 1LI numerical integration must be performed. This can be done by regularly distributed areas or lines.

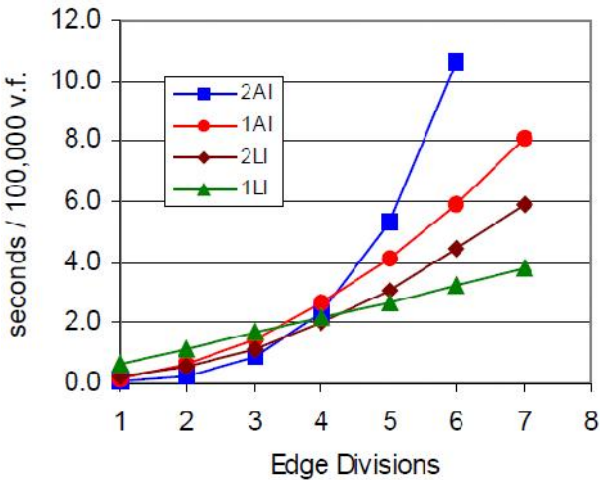


Figure 3-5: Run-time behavior for view factor models (Walton, 2002).

The figure above shows the run-time for a hundred thousand view factors as a function of edge divisions for two opposed squares. The curves follow the operation count and time complexity estimation. For very crude approximations double area integration is the fastest, but it quickly reveals its power-of-four behavior. Single line (1LI) and single area (1AI) integration follow a power-of-two curve. Single line integration is the fastest approach because of its linear time complexity.

When introducing Gaussian quadrature formulas instead, Walton (2002) observed that for the same number of divisions, accuracy improved by several orders of magnitude. The integration points are specially selected as shown in the following figure.

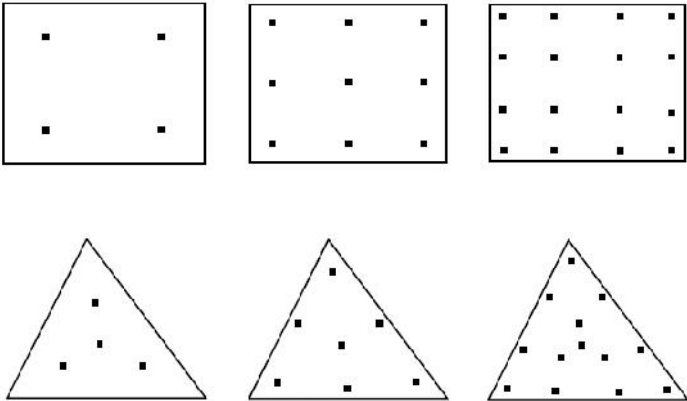


Figure 3-6: Point locations for Gaussian area integration (Walton, 2002).

The points tend to be placed towards the edges of polygons. Krishnaprakas (1998) demonstrated the use of double area integration for triangles by transforming the area integrand to area coordinates. This resulted in reducing the number of summation loops from four to two. Rao and Sastri (1996) used Gaussian integration for the double line integration. For curved edges, a non-linear transformation was developed.

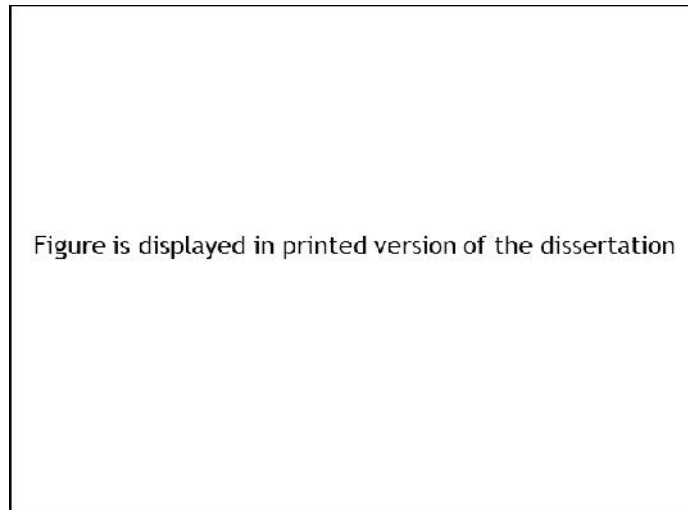


Figure 3-7: Study of point source shadows by da Vinci. Copyright © 2003 Wiley. Used with permission from (Hasenfratz et al., 2003).

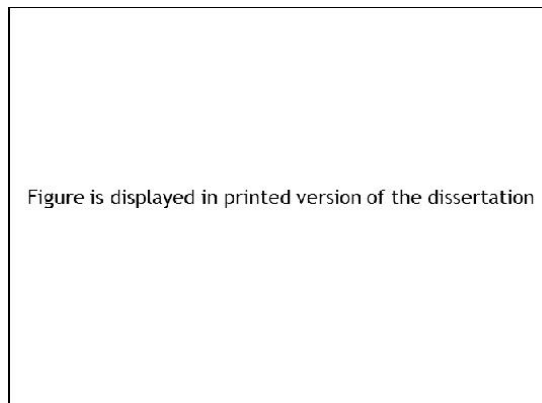


Figure 3-8: Shadow construction by Lambert. Copyright © 2003 Wiley. Used with permission from (Hasenfratz et al., 2003).

Leonardo da Vinci observed the casting of shadows from point sources as shown in Figure 3-7. Lambert constructed shadows with geometric considerations as in Figure 3-8.

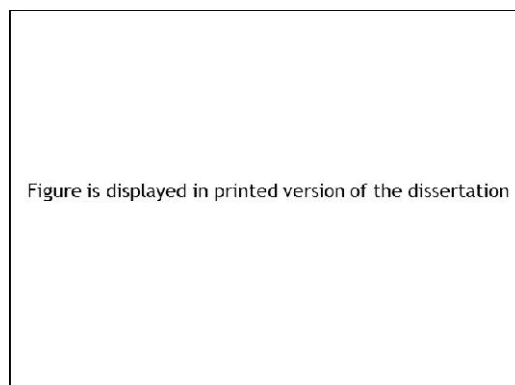


Figure 3-9: Hard shadow. Copyright © 2003 Wiley. Used with permission from (Hasenfratz et al., 2003).

The construction of a hard shadow is quite simple. When there are several occluders, the shadow area is the union of all individual shadows. In computer graphics a light source might be considered as a point source, when the distance from the emitter is much larger than the distance from the occluder to the receiver. But even the sun is an area light source. There are very few analytical expressions for occluded view factors. One such derivation known to the author between a differential element and a rectangle with a single rectangle as an occluder was done by Deiveegan et al. (2004) using contour integration. Even there, the assumption was made that the angle between the normal vectors of the occluder and receiver is zero.

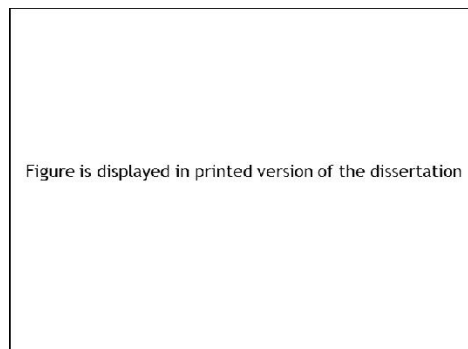


Figure 3-10: Soft shadow. Copyright © 2003 Wiley. Used with permission from (Hasenfratz et al., 2003).

The more common area light source casts several shadows. For polygonal objects, shadows must be traced from the vertices and the edges. The penumbra is the area on the receiver from one point source. The union of all penumbrae is the umbra where the light source is completely blocked.

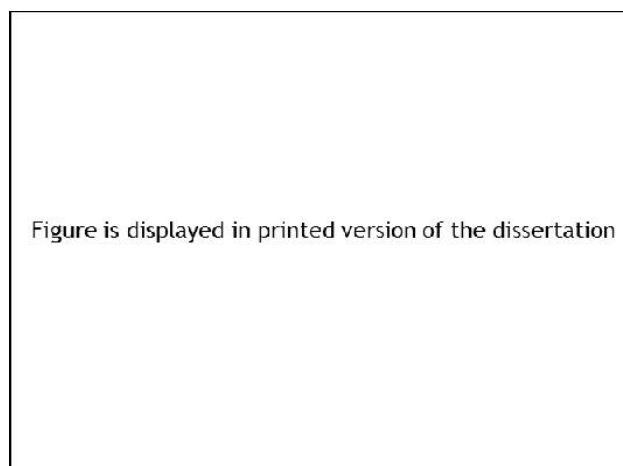


Figure 3-11: Soft shadow with two obstructions. Copyright © 2003 Wiley. Used with permission from (Hasenfratz et al., 2003).

Combining the shadows of two occluders is not simply the sum of the two shadows as shown in Figure 3-11. The umbra can be larger as indicated by the red highlighted zone. Even though both occluders individually would allow some light to pass into the red zone, acting together they block it completely.

In terms of thermal radiation, there are two strategies to obtain view factors with occlusions. The simplest strategy is to expand Eq. (3-18) by a blockage factor b .

$$F_{1-2} \approx \frac{-1}{A_j f} \sum_{i=1}^{N_1} \sum_{j=1}^{N_2} \frac{(\mathbf{r} \cdot \mathbf{n}_1)(\mathbf{r} \cdot \mathbf{n}_2)}{(\mathbf{r} \cdot \mathbf{r})^2} b_{i,j} \Delta A_i \Delta A_j \quad (\text{Eq. 3-25})$$

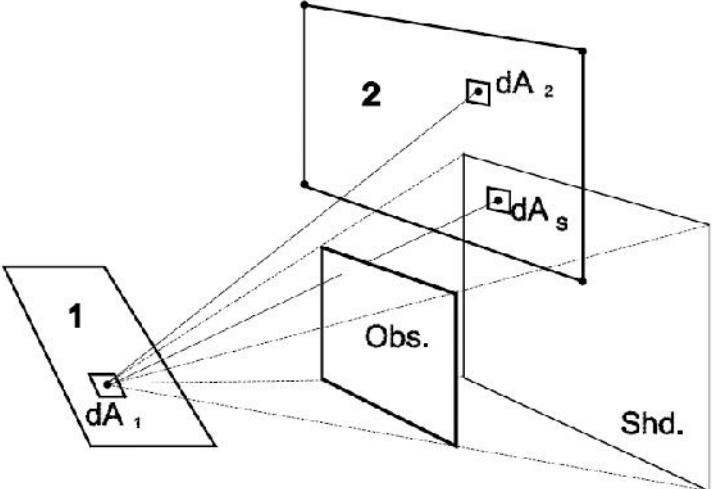


Figure 3-12: Partially obstructed view for blockage factor (Walton, 2002).

The blockage factor $b_{i,j}$ can be either one or zero. It is determined by casting a ray from each differential source to each differential receiver. If the ray hits a different element that is located between emitter and receiver the blockage factor is zero.

The second strategy is projecting a shadow on the receiving face as shown in Figure 3-12.

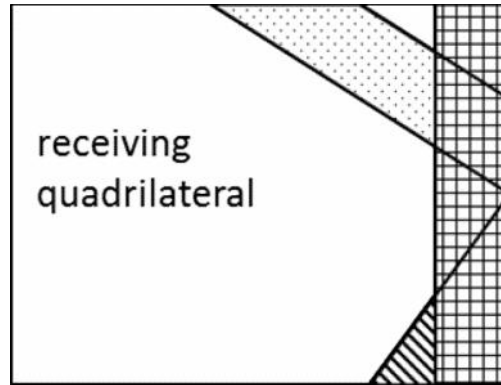


Figure 3-13: Shadow projection.

Walton (1986) used shadow projection for each obstacle and double line integration. For each shadow the view factor is calculated and subtracted from the unoccluded view factor. Care must be taken that only the fraction of shadow that has not been cast by a previous occluder is taken into account.

This process is very time consuming as the resulting polygon in general is not convex and has many edges. This method is problematic because a negative view factor might occur by subtracting them. Walton (2002) modified this approach by employing single area integration. All obstacles are first projected on the receiver and then numerical integration occurs.

In one of the first studies on radiosity, Nishita and Nakamae (1985) determined umbra and penumbrae by the blockage factor as shown in Figure 3-10 and Figure 3-14.

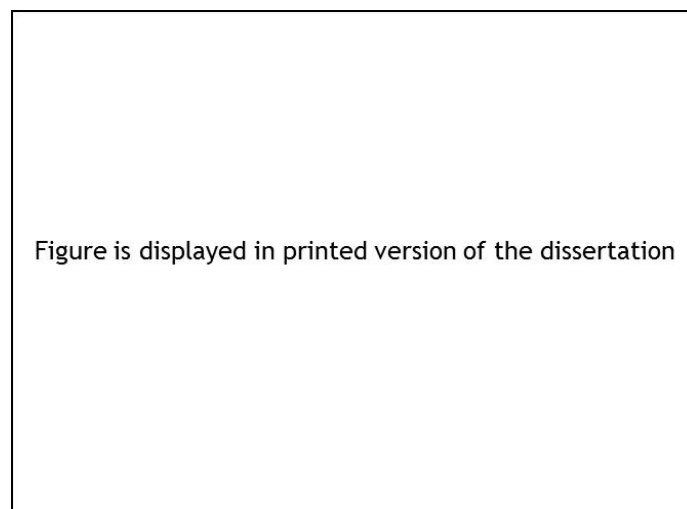


Figure 3-14: Determination of blockage factor (Nishita and Nakamae, 1985). © 1985, ACM, Inc.

The visibility is checked by considering the triangle P_i , P_{m1} , and P_{mk} . The obstacle is projected on S_a and the line source clipped against the contour line.

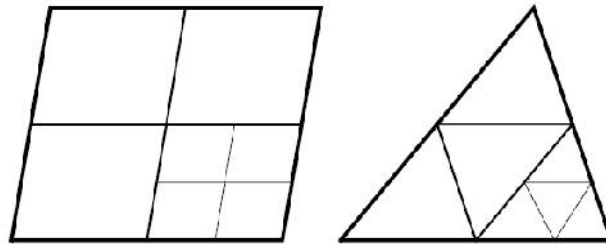


Figure 3-15: Adaptive subdivision (Walton, 2002).

Adaptive integration is also used. When Gaussian integration for two different numbers of weighing points gives similar results, calculation stops. Otherwise the surface is divided as shown in Figure 3-15. This procedure is repeated recursively.

Saltiel and Kolibal (1993) used adaptive grid generation to improve view factor accuracy and a blockage factor for possible obstructions. They employed two different amounts of weighing points (p-refinement) and mesh (h-) refinement as a first criterion, depending on which method causes an error tolerance to pass a threshold. As a second criterion under- and oversampling is considered. Undersampling can occur when the first criterion is satisfied, no refinement is made the last two iterations, but the contribution of the refined view factor is significant. Oversampling happens when a single view factor has no significant impact on the row sum of the view factor of the subelements after refinement. Finally, a third criterion checked whether the first two criteria failed due to poor error thresholds. By adapting the first two thresholds with the third one they obtained the following results for two planes at an angle of 60° with k as the number of iterations, N the number of elements on one plane, E the error of the view factor, and t the run-time:

Figure is displayed in printed version of the dissertation

Figure 3-16: Adaptive mesh refinement (Saltiel and Kolibal, 1993). Copyright © 1991 by AIAA, Inc. Reprinted with permission of the American Institute of Aeronautics and Astronautics.

It can be seen that by this method run-time rises significantly when the maximum error of the view factor is set too tightly.

Up to now, only view factor calculations whose obstructions needed to be taken into account, separately, were considered. Figure 3-2 shows a family of methods that do consider view factors and obstructions simultaneously. In its original form they are projection methods between a differential element and a finite surface. A plane, a hemi-cube, or a hemisphere is constructed around the differential element with unit length or diameter. This results in a base with unit area around the differential element. Therefore, this family of methods bears the name hemisphere sampling.

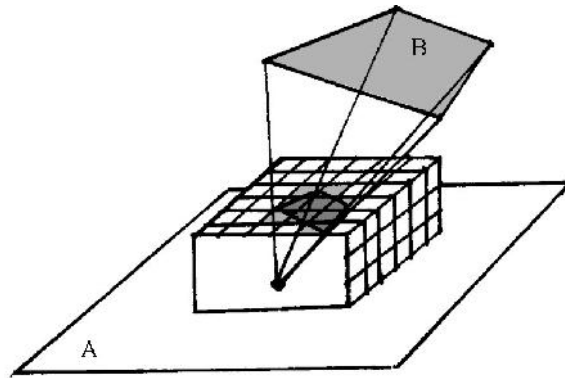


Figure 3-17: Projection on a hemi-cube (Fleischmann, 2007).

The existing surface around the differential area is divided into sub-elements. The view factors of those sub-elements are called δ -view factors and can be pre-computed. The polygon B is projected on those sub-elements and the sum of the δ -view factors gives the form factor. When there are occluders, these are projected too and for each sub-element the face that is closest to it is recorded. In computer graphics this is usually done by z-buffering. In this way possible occluders are taken care of, for they reduce the number of sub-elements between A and B. The justification to use a hemisphere, hemi-cube, or hemi-plane lies in Nusselt's analogy, that the projection of a sub-element B_H of a hemi-cube yields the same result as the projection on the hemisphere B_S as shown in Figure 3-18. This assumption cannot be true in situations where a face is situated near the base of the hemisphere. In that case a hemi-plane simply would not have any sub-elements to project on. This leads one to investigate the possible errors of the hemisphere sampling methods with the hemi-cube method as an example.

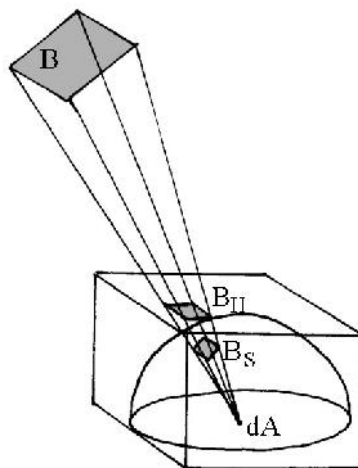


Figure 3-18: Nusselt's analogy (Fleischmann, 2007).

Baum et al. (1989) performed a study on this subject and defined three errors:

- 1) Proximity Assumption: Eq. (3-16) presumes that the source is infinitesimally small and, consequently, only one integral of the destination area needs to be resolved. The more a source surface deviates from this idea, such as long-stretched rectangles, the greater the error, as shown in the following figure:

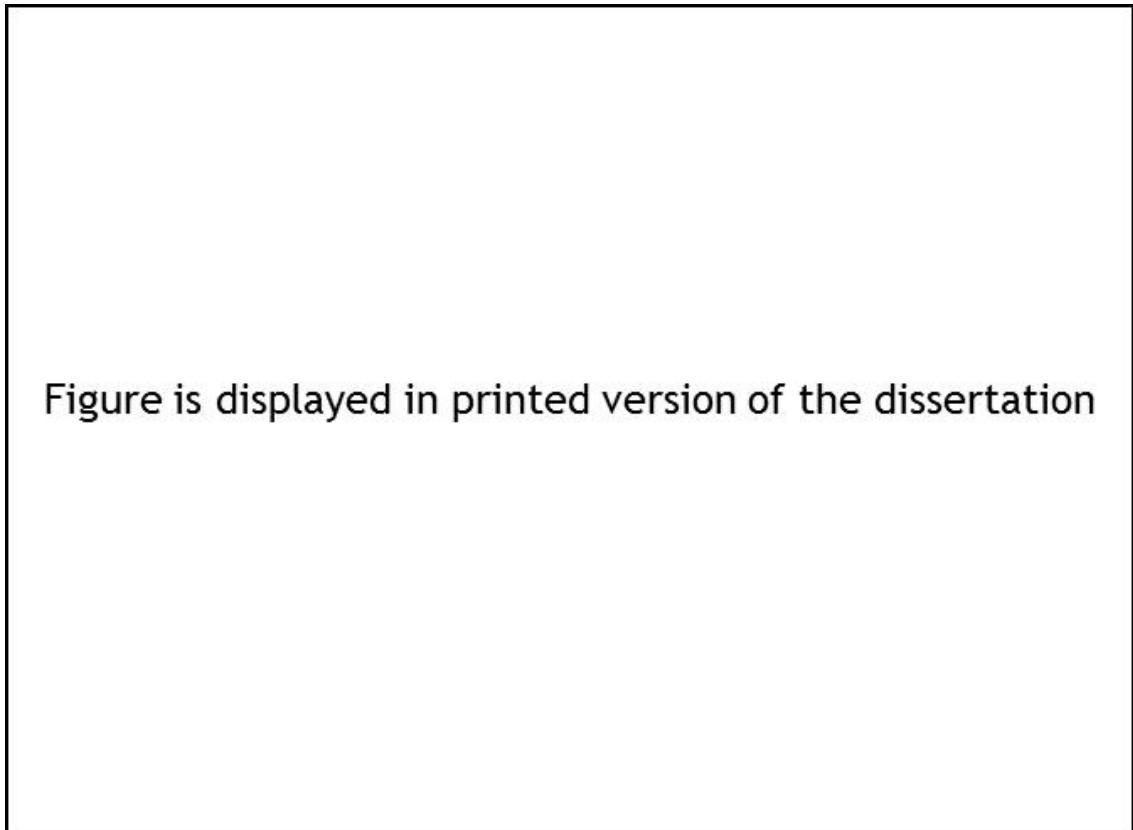


Figure 3-19: Relative error in view factors for hemi-cube by Baum et al. (1989). © 1989, ACM, Inc.

Figure 3-19 shows several possible orientations between faces and ray positions. The diagram plots a relative error between view factors and a normalized distance. This distance is defined as the distance between the element and patch centers divided by the patch diameter. Though not stated explicitly in Baum et al.'s work, it is custom to define the relative error as the difference between calculated and analytical value divided by the analytical value. In this plot, the parallel-center curve coincides with the radial-center curve. This plot between two squares would suggest that a normalized distance less than one would create great deviations, whereas over a distance of five all view factor errors tend to become negligible.

2) Visibility Assumption: Because of the simplification by the differential element 1 all occlusion tests are conducted from the center of the face only. As a result, surface 1 in Figure 3-20 can see the complete surface 2, because the ray cast from the center misses surface 3. The view factor from 1 to 2 will be overestimated.

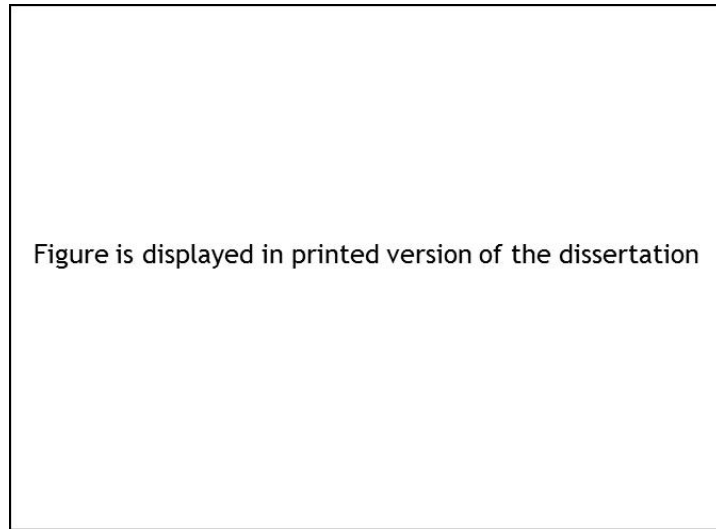


Figure 3-20: Visibility assumption (Baum et al., 1989). © 1989, ACM, Inc.

3) Aliasing Assumption: The third assumption stems from computer graphics terminology. Because all subelements have the same size, partial covering of a projection will cause an overestimation of the δ -factor if the center of the subelement is just covered as in Figure 3-21, whereas if the centers are not inside the projection areas, those δ -factors are not counted.

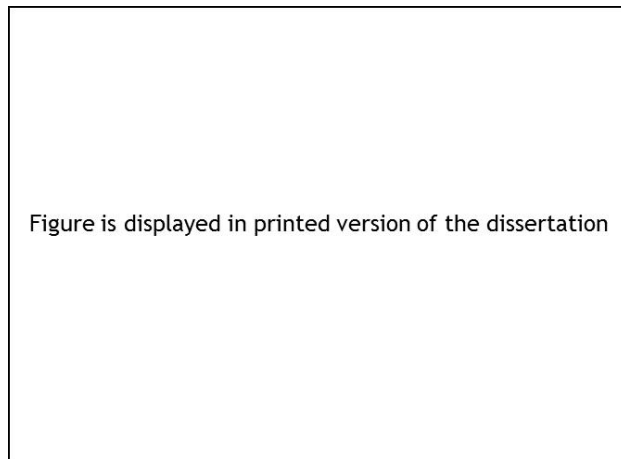


Figure 3-21: Aliasing effect (Baum et al., 1989). © 1989, ACM, Inc.

Belonging to the same family of methods is the hemi-sphere-base method.

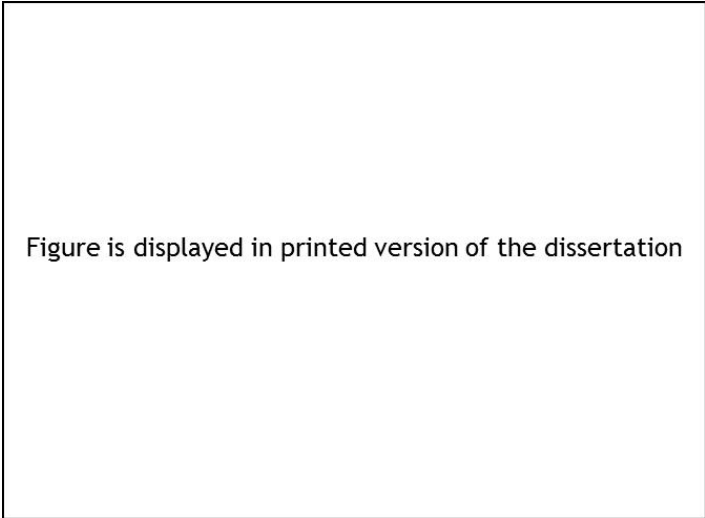


Figure 3-22: Hemi-sphere-Base projection. Copyright © 2009 Wiley. Used with permission from (Yamada et al., 2009).

The figure above shows how a face is projected onto the unit base by projecting vertices and edges. Doi and Itoh (1998) introduced the discretization of polygons into triangles before projection in order to reduce the aliasing error. On the one hand the projection takes quite a few operation counts, on the other hand it must be done only once per surface, whereas the hemi-cube method must undergo the projection test possibly on all sides of the hemi-cube. The edges are assigned to an element of the screen by a meridian test. This procedure is easily parallelizable.

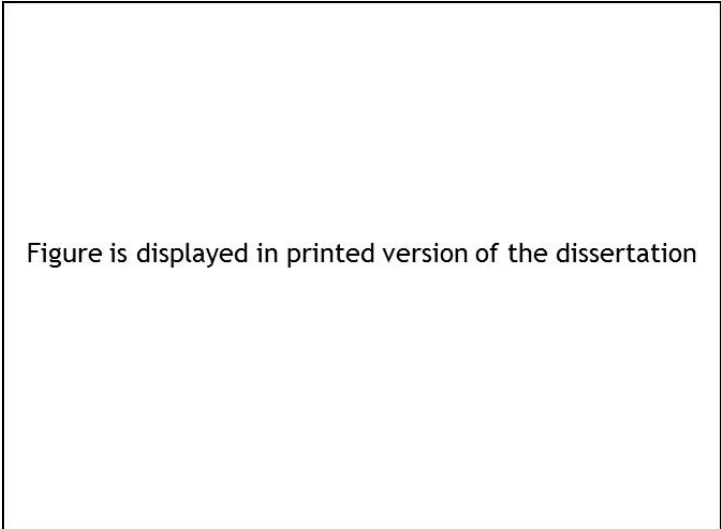


Figure 3-23: Cell registration on Hemi-sphere-Base. Copyright © 2009 Wiley. Used with permission from (Yamada et al., 2009).

Another method of the hemisphere sampling base is a Monte Carlo (MC) method based on the hemi-cube, hemi-plane, or hemi-sphere. Projection does not occur. Instead, rays are cast from the base to the subelements for the first aforementioned methods and then, as done for the hemisphere, oriented in radial direction to the surrounding. Thus, MC involves a ray-surface intersection for each ray and surface.

Pellegrini (1997) states that the hemisphere sampling methods have a linear worst time complexity.

Comparing Monte Carlo (MC), double area integration (2AI), and base-hemisphere (HS) for a simple cube, Yamada et al. (2009) found that MC was slow and yielded the largest error. 2AI had the highest accuracy but was also the slowest. HS was the fastest and the range of error was between the other two methods.

Sakai and Maruyama (2003) simplified their view factor calculations by assuming two differential elements in the spirit of Figure 3-19. Only neighboring faces used an analytical equation. This way they speeded-up their calculations but lost in accuracy.

3.3.2 View Factors and Thermodynamics

Two very important relations concerning form factors need to be satisfied:

$$\sum_{j=1}^N F_{ij} = 1 \quad (\text{Eq. 3-26})$$

The sum of all receiving view factors F_{ij} should be one. This represents first-principle thermodynamics. The reciprocity relation comes from the following reasoning as mentioned in Loehrke et al. (1995):

$$Q_{i-j}^k = \varepsilon_i^k F_{ij}^k A_i \sigma T_i^4 F_{b,i}^k \quad (\text{Eq. 3-27})$$

This equation describes the heat flow Q_{i-j}^k from the face i to j , with ε_i^k as emissivity at wavelength band k , A_i the face area, σ the Stefan-Boltzmann constant, T_i^k the temperature at wavelength band k and $F_{b,i}^k$ as the fraction of blackbody emission in wavelength band k . For each wavelength band a separate calculation must be made. Therefore, the superscript k is omitted. When two surfaces i and j have the same

temperature and emissivity one can write the same Eq. (3-27) for surface j, set them equal, and simplify:

$$A_i F_{ij} = A_j F_{ji} \quad (\text{Eq. 3-28})$$

This very important reciprocity equation comes from fixing two faces to the same temperature. In this situation the net heat flux is zero and thus obeys second-principle thermodynamics.

3.3.3 Correcting View Factors

There are two main reasons for correcting or smoothing form factors.

- 1) Reducing the error and thus adhering to the first and second law of thermodynamics.
- 2) Allowing for a compact storage of view factors when symmetry of the view factor matrix **F** is achieved.

There are several possibilities for correcting view factors. Clarksean and Solbrig (1994) came up with one of the more simple ways to determine view factors and relied on the reciprocity and summation relations to fill the view factor matrix. Very similar is a method called ‘naive’ by Taylor and Luck (1995) which discards the entries below the diagonal of the view factor matrix as well as employing the summation rule to the diagonal entry:

$$F_{ii} = 1 - \sum_{\substack{j=1 \\ j \neq i}}^N F_{ij} \quad (\text{Eq. 3-29})$$

F is the view factor and N the number of elements. This simple method has the disadvantage that it might give physically meaningless negative values.

Van Leersum (1989) describes a simple method that avoids negative form factors.

- 1) A correction factor d_i is calculated with m being the number of nonzero view factors in row i:

$$d_i = \frac{1 - \sum_{j=1}^N F_{ij}}{m} \quad (\text{Eq. 3-30})$$

- 2) This correction factor is added to each nonzero view factor in the row. For the number of negative factors obtained, m is reduced by the number of negative values in the row and d_i is recalculated, bypassing negative view factors. Steps 1) and 2) are repeated until there are no more negative factors.
- 3) Apply reciprocity relation for column i . Steps 2) and 3) are repeated for each row-column pair.
- 4) Repeat Steps 1) to 3) for each row.
- 5) Repeat Steps 1) to 4) until d_i is sufficiently small.

This procedure is reported to have good convergence behavior by Taylor and Luck (1995).

Lawson (1995) modified this procedure by substituting steps 1 to 3 replacing each view factor in the row with the following equation:

$$A_i F'_{ij} = A_i F_{ij} + \frac{A_i F_{ij}}{A_i \sum_{j=1}^N F_{ij}} \left(A_i - \sum_{j=1}^N A_i F_{ij} \right) \quad (\text{Eq. 3-31})$$

This procedure with F'_{ij} being the corrected form factor is claimed to prevent negative view factors and maintains reciprocity by taking the relative areas into account.

Taylor and Luck (1995) also mention a least-squares optimization problem:

$$y = \sum_{i=1}^N \sum_{j=1}^N w_{ij} (F_{oij} - F_{ij})^2 \quad (\text{Eq. 3-32})$$

Here, y corresponds to the weighted sum-square error, w_{ij} to a weighting factor, and F_{oij} to corrected view factors. Employing these methods for view factor rectification in a simple test case gave the following results:

Figure is displayed in printed version of the dissertation

Figure 3-24: Heat flux standard deviations for view factor rectification (Taylor and Luck, 1995).
Copyright © 1995 by AIAA, Inc. Reprinted with permission of the American Institute of Aeronautics and Astronautics.

In this figure view factors were randomly generated and additional variances added from left to right for the columns in Figure 3-24: diagonal dominant, counter diagonal, row dominated, column dominated, upper triangle, and random. These view factors were corrected with the naive method, van Leersum's method, and least-squares optimization with and without a weighting function. Overall, weighted least squares yielded the best results. If weighting factors are not available, the unweighted optimization would be the choice. Van Leersum's method yielded good results and is considered to be a simple method. Naive enforcement of closure and reciprocity is not recommended.

Loehrke et al. (1995) used a modified least-squares method for view factors by the Monte Carlo method. They defined the error bound C_{ij} very similar to Eq. (5-2):

$$C_{ij} = K \sqrt{\frac{1 - F_{ij}}{N_i F_{ij}}} \quad (\text{Eq. 3-33})$$

With K being a confidence measure and N_i the number of rays shot from face i . New estimates for F'_{ij} are obtained with the following equation:

$$A_i V_i F'_{ij} = \left(\frac{C_{ji}^2}{C_{ij}^2 + C_{ji}^2} \right) A_i V_i F_{ij} + \left(1 - \frac{C_{ji}^2}{C_{ij}^2 + C_{ji}^2} \right) A_j V_j F_{ji} \quad (\text{Eq. 3-34})$$

Following this step again energy must be conserved. It would be tempting to correct the main diagonal entry, because in this way reciprocity would not be violated. But this procedure could produce negative view factors. Therefore, Loehrke et al. (1995) resort to least-squares optimization. For the convergence measure C_i serves:

$$C_i = \frac{K}{N} \sum_{j=1}^N \sqrt{\frac{(1 - F_{ij})F_{ij}}{N_i}} \quad (\text{Eq. 3-35})$$

N is the total number of faces. They found that this procedure yields an overall improvement in the root mean square (RMS) of the difference of the view factors to their analytic solutions.

3.4 Data Structures for View Factor Calculation

Data structures are such an important issue that they would deserve entire dissertations. For the purpose of this paper only a very brief overview of this topic is given.

3.4.1 Space Partitioning

In order to speed-up calculation of view factors data needs to be arranged in a way that makes access to information as fast as possible. Trees offer such an arrangement. This is necessary for determining the obstructions between two faces. The ray-face intersections should be as few as possible. Consequently, only faces in the vicinity of the two faces and the shaft between should be examined. Examining possible obstructions is called obstruction culling or view culling in computer graphics.

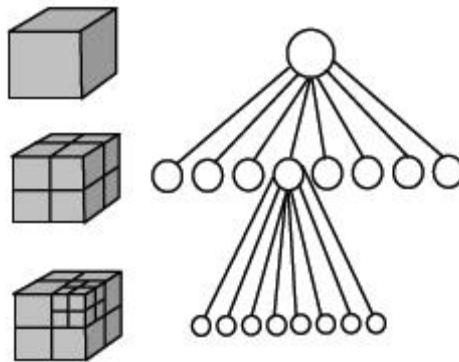


Figure 3-25: Octree (Paulke, 2007).

A tree is a set of nodes. In the case of an octree each node either has none or 8 children nodes as shown in Figure 3-25. The top circle is the root node which corresponds to the entire space as shown as the cube on the left side. The second row of circles stand for nodes representing sections of the original cube. The lines between the nodes are called edges. In level three of the nodes, edges are drawn only from one node. That means that one level two node has eight child nodes and each level three node shares one parent node. The level one node is called the root. The nodes without children are called leaves. The other nodes are called internal nodes. The leaves contain the actual faces in one octant of their parent cubes. In all nodes the planes bordering the respective space are saved.

Traversing the nodes in such a way that no node is visited twice is called a path. The longest possible path, which must be from the root to a leaf, is called the height of the tree. The reason why a tree provides fast access lies in its height. The octree above has the height 2 meaning two edges must be traversed from the root to a leaf in a worst case scenario. The tree has a search time of the order $O(\lg_2 N)$ with \lg_2 being the logarithm of the base two and N the number of nodes. This is valid only under the assumption that the tree is balanced. The ideal would be if all nodes on level two had their children nodes. Then, on level three, the tree would contain $8^2=64$ leaves. In that case all paths from the root to each leaf would have the same length and the tree would be perfectly balanced. In the example the tree is not balanced, because of level three leaves. This situation would be aggravated if additional nodes were inserted on the level three nodes as it would enlarge the height of the tree.

Another important tree is the kd tree. With the octree the space is evenly subdivided. As a result, it might be that some octants contain many elements and some none at all. The kd tree can circumvent this, for it is desirable that the elements are evenly distributed among the leaves.

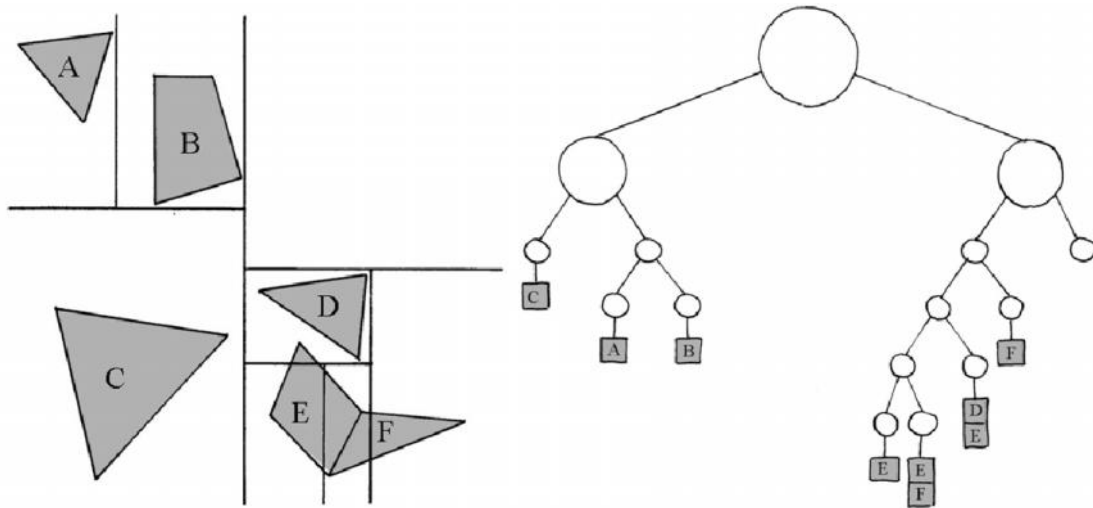


Figure 3-26: Kd Tree in 2D (Fleischmann, 2007).

The kd tree has at most two children. Subdivisions are done sequentially along the coordinate axis. In 2D the x-direction is used first followed by the y-axis which is followed again by the x-axis.

Crucial is the choice of the position of the partitioning plane. One possibility is the object median, a plane dividing the set into an equal number of elements.

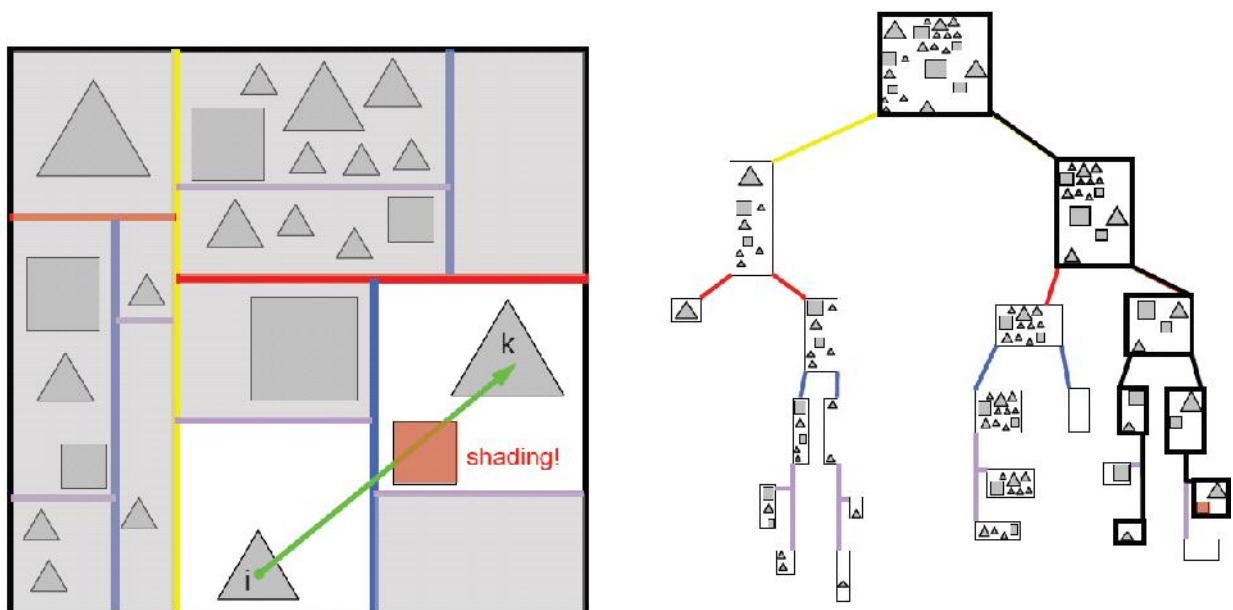


Figure 3-27: Occlusion calling with kd tree (Paulke, 2007).

Figure 3-27 demonstrates an advantage of this tree for occlusion culling. After building the tree shading detection can take place between the two bold leaves. In this tree one can give the range in which the possible occluders might be investigated allowing a great saving without incurring inaccuracies. The more apart the leaves are the more ray element intersection tests might have to be done. A possible danger in using this tree lies in the build-up phase as the tree might not be well balanced.

Figure 3-28 shows a kd tree in 3D for a passenger compartment.

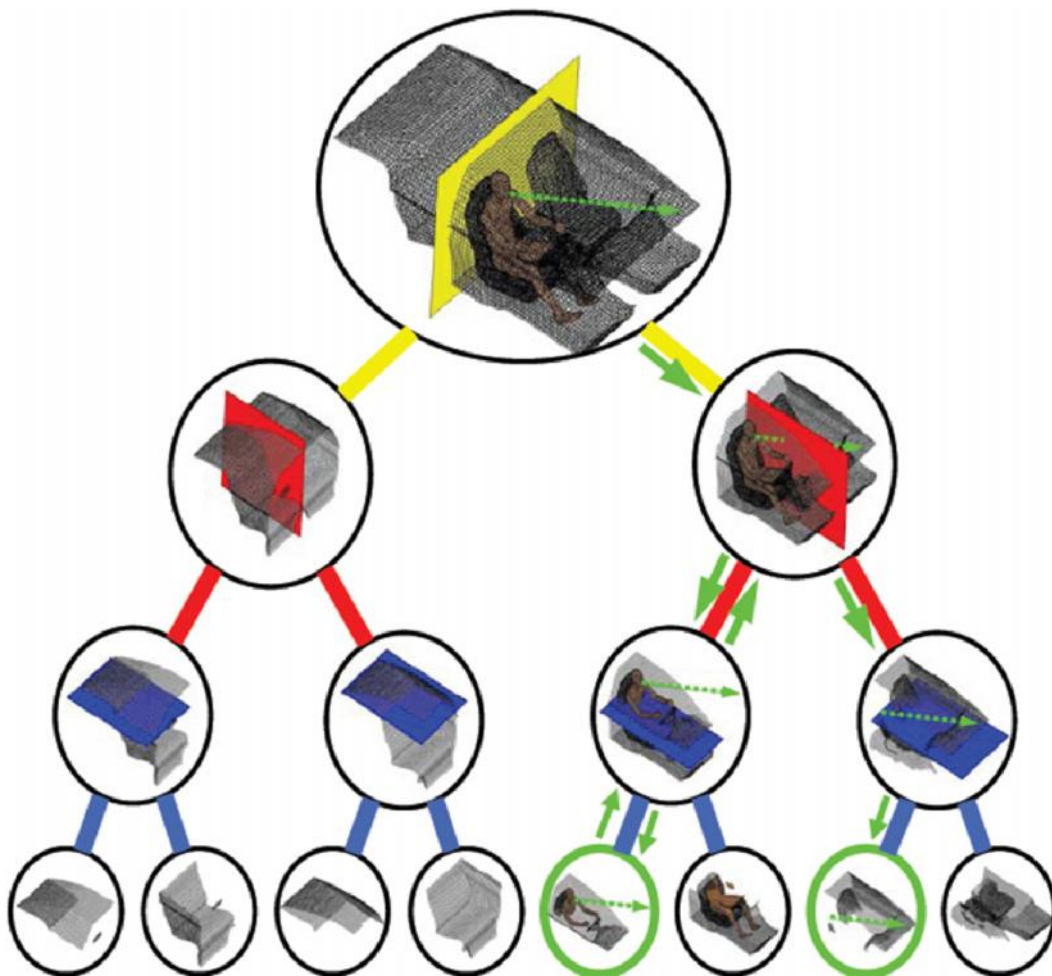


Figure 3-28: Kd tree in 3D (Paulke, 2007).

The binary space partitioning tree (bsp) is even more flexible than the kd tree as it does not require axis aligned partitioning planes. This tree is often used for backface culling. This procedure determines which elements are facing each other. Those pairs that do not face each other do not need to be included in view factor calculations.

Bittner (2002) describes an occlusion tree which basically is a bsp tree in 5D. This tree is built from the source element emanating rays. The leaves contain the rays that are either blocked or unoccluded.

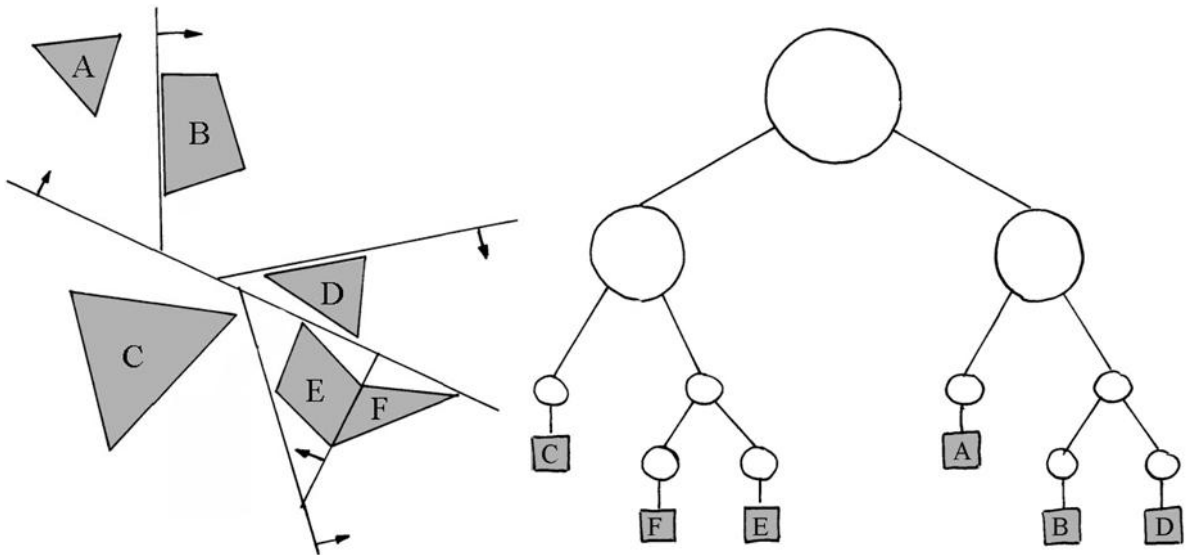


Figure 3-29: BSP tree (Fleischmann, 2007).

3.4.2 Bounding Volumes

The aim of bounding volumes is to further reduce the number of ray intersection tests. In order to determine visibility between two elements a shaft is created that includes the two elements. Possible obstructions are tested to determine whether a ray hits a simplified volume that wraps an element within the shaft. If the ray does not hit the bounding volume no further ray intersection tests need to be done for that element.

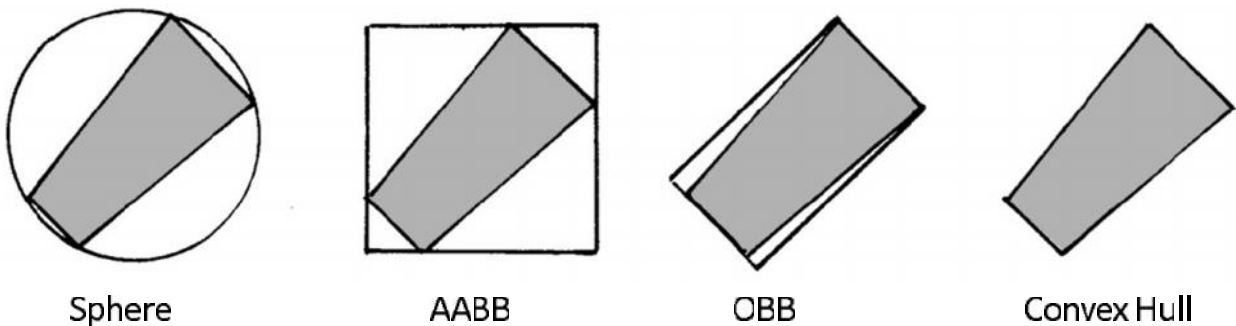


Figure 3-30: Bounding volumes modified from (Fleischmann, 2007).

The Sphere has the simplest ray intersection test but also the largest void volume. An axis aligned bounding box (AABB) is a simple hexahedron with planes aligned

with the axis. Oriented bounding boxes (OBB) have the hexahedron aligned with the element. Convex hulls make sense when there are several elements combined but the construction takes $O(N \lg_2 N)$ with N being the number of elements. The more void space in the bounding volume, the easier the ray intersection tests, but one risks more hits by rays calling for ray element intersection tests. These bounding volumes can be structured in trees further reducing the amount of tests if a leaf of a tree is not hit.

3.5 Benchmarks

Having looked at various methods and data structures to calculate view factors for the surface to surface method, the thermal engineer must now test the accuracy and speed of the code employed, made either by himself or commercially. Emery et al. (1991) was the first known to the author, who compared various thermal radiation programs. He created among other cases randomly oriented and positioned quadrilaterals of the same size with varying package density. He recommended employing the hemi-cube method for complex scenes.

Malalasekera and James (1993) and later Tuomaala and Piira (2000) presented some benchmark cases. They used simple geometries such as a cube and simplified rooms as thermal comfort calculations. The solar load of buildings has been of broad interest to the building industry. The wall temperatures in these benchmarks were fixed and radiation heat contours were published. Heat flows are more susceptible to errors than temperatures.

Vujičić et al. (2006) investigated two parallel plates that were successively refined. They found by employing Monte Carlo that refining the mesh without increasing the number of rays will produce less accurate results. This may seem counterintuitive at first. The surface to surface method is based on the assumption of constant temperature for a face. This assumption is met for differential elements. Therefore, refinement as in CFD seems to be a proper choice. Unfortunately, view factors are susceptible to round-off errors. The smaller the sub-elements the more likely the errors will sum up. In the extreme case, the sub-elements do not see each other. For methods involving rays intersecting an element that is either further apart or smaller becomes increasingly difficult.

The other extreme of calculating primitive shapes such as parameterized cylinders was investigated by Walker et al. (2010). The aim was to prevent the creation of surface meshes, thus speeding up the workflow. But the calculation time reported was unacceptable.

The author (Rauch et al., 2007) performed an analysis on view factor accuracy and speed for two thermal radiation solvers specialized in the automotive industry, namely RadThermIR 8.1 and TheseusFE 1. A third code View3D from the National Institute of Standards (NIST) serves for comparison purposes. It cannot solve the balances.

The first test case is a simple hexahedron as shown in Figure 5-10 with two three by three units length for the opposite squares holding a distance of 90 units to each other. The emissivity is set to 0.9 for all faces and the temperature of all faces is kept at 293.15K except the one opposing square which is kept at 333.15K. No conduction or convection is allowed and radiation is permitted only inside the enclosure. The difficulty lies in the correct estimation of the form factor of these opposite planes. The system of linear equations was solved by using successive over-relaxation (SOR) with a relaxation factor of 1.25 and a maximum tolerance of 10^{-9} . Figure 3-31 shows the results for view factors from the hot wall to the opposite side. The relative error is defined as the difference between the given and the analytical solution, divided by the analytical solution and multiplied by one hundred.

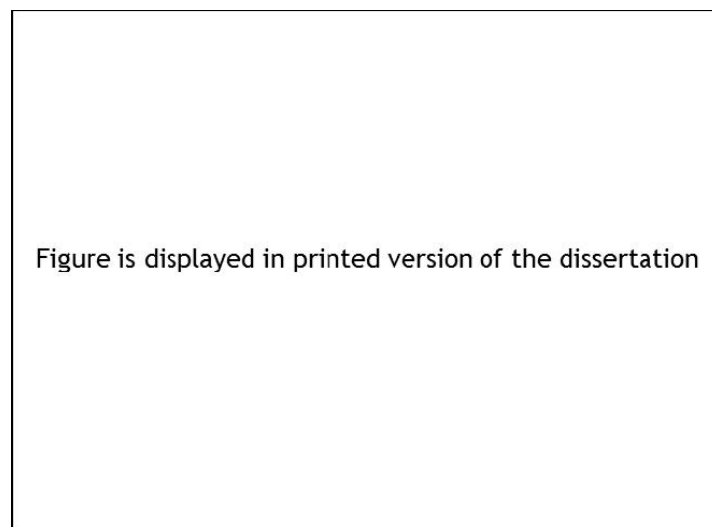


Figure 3-31: View factor error for the hexahedron for various programs (Rauch et al., 2007). © 2007, Chandos Publishing (Oxford) Ltd.

Here, programs using ray tracing techniques as used by RadTherm suffer a disadvantage, because emanating rays are more likely to hit the sidewalls. Usually there are statistically less rays cast at the normal angle of the emitting surface.

This accounts for the large deviation of both form factors and fluxes for RadTherm. 'RadTherm low' and 'RadTherm high' refer to settings employed in RadTherm: The lowest setting emanates about 512 rays and the highest setting 294912 rays per quadrilateral.

Theseus solves the double area integration in equation five by Simpson's integration and optionally Gaussian quadrature. Also, an 'analytical' and a 'mixed' method is offered, which switches between methods according to a factor based on differences between cells. It is possible to change the threshold for this switching which offers the specialist a fine tuning for a specific problem. Because of the increase in complexity this feature has not been investigated more closely. Both methods investigated offer very good results. View3D shows excellent agreement with the analytical solution of 0.00316205683875.



Figure is displayed in printed version of the dissertation

Figure 3-32: Heat flux error for the hexahedron for various programs (Rauch et al., 2007). © 2007, Chandos Publishing (Oxford) Ltd.

For the heat flux the energy balance with the view factors of View3D were used. Again, it showed the smallest deviation from the analytically determined heat flux of 1.3392 W/m^2 . The reason why the commercial tool show an increase in the relative error compared to the error of the view factors can be explained by the errors of other view factors in the system. A closer examination of the case of 'Theseus Simpson' revealed that the configuration factors for the perpendicular large sides deviated up to 50%. Even though these sides have the same temperature as the small receiving plate, they still contribute to the other sides' radiative heat fluxes by their reflectances as the emissivity permits 10% reflection.

Walton (2002) used a benchmark first described in a textbook by Shapiro (Reference in Walton, 2002). Originally, two opposing squares with unit lengths and distance had a two-dimensional plate three fourths of a unit away from the first plane in between them. This time Rauch et al. (2007) created a cube with unit length and placed the plate inside. The square plate has a length of 0.75 and is placed centrally in front of the opposite square as shown in Figure 3-33.

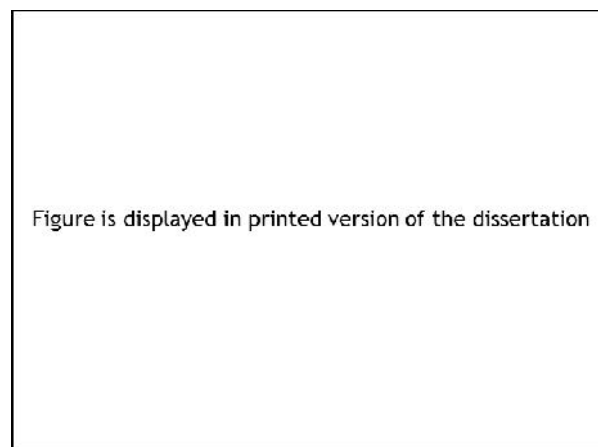


Figure 3-33: Benchmark Shapiro with front side removed (Rauch et al., 2007). © 2007, Chandos Publishing (Oxford) Ltd.

To simplify calculation the emissivity is set to 1 because the energy matrix is now an identity matrix and each row can be solved independently. The temperatures are chosen to be the same as for the hexahedron where the source with 333.15K is the side furthest away from the plate opposing it. The side facing away from the source is thermally insulated.

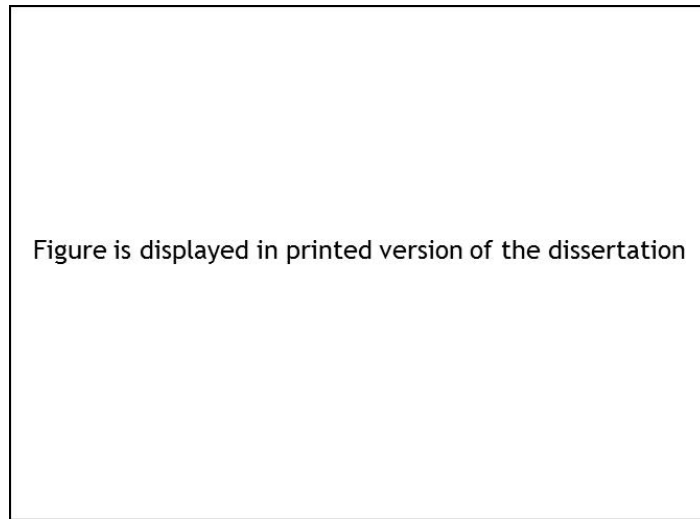


Figure 3-34: View factor error for Shapiro for various programs (Rauch et al., 2007). © 2007, Chandos Publishing (Oxford) Ltd.

The source plate and its opposing, partially hidden face are investigated. In this case Theseus fails to detect the obstruction, because partial occlusions are not supported. RadTherm, on the other hand, does quite well here, because many rays hit the unobstructed area of the receiving plate. It is more likely to cast rays to the side than exactly to the front of the face.

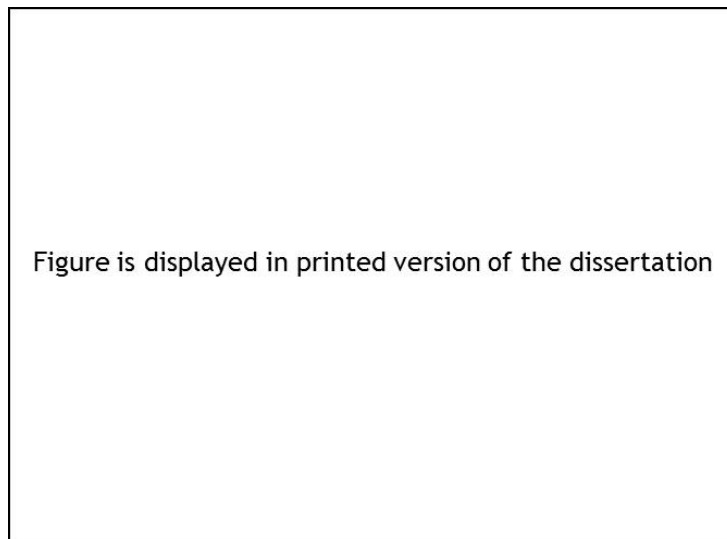


Figure 3-35: Heat flux error for Shapiro for various programs (Rauch et al., 2007). © 2007, Chandos Publishing (Oxford) Ltd.

A search was conducted to discover the reason why the heat flux for 'RadTherm low' failed so badly. After examining the view factor from the hot plate to the obstructed plate which did not show much error, the view factor from the obstructed to the hot plate was scrutinized. It was observed that RadTherm ignored

the reciprocity relation which states that a view factor from surface '1' to '2' times the area of '1' equals the form factor of '2' to '1' times the area of '2'. Instead, RadTherm predicted no view from the obstructed plate to the hot plate. Older versions of RadTherm were able to import view factors. Therefore, the author (Rauch et al., 2007) imported the view factor RadTherm calculated for the hot plate to the obstructed plate and the resulting heat flux for the obstructed plate correlated with the error of the view factor as expected.

The third case is a study of a cabin with a dummy sitting on the right side. Several meshes with various resolutions were created ranging from 30 to 40 mm in length for each side of a quadrilateral of the cabin walls. The resulting meshes consisted of 14993, 19056, and 26860 predominantly quadrilaterals and two meshes consisted of 27504 and 71918 triangles.

All but the mesh with the highest number of elements were created by SPIDER. The mesh with the largest number of cells was created by CFD-VisCART distributed by ESI GmbH. The emissivity was set to 0.9 for all surfaces with a wall thickness of 1.5 mm. This time no temperatures were given but there was a heat source of 100W at the windscreen and a heat sink of -100W at the rear screen. All walls were considered adiabatic and conduction and convection neglected as much as possible. In this setting the energy balance matrix was solved for the temperature. The calculations were carried out for steady state.

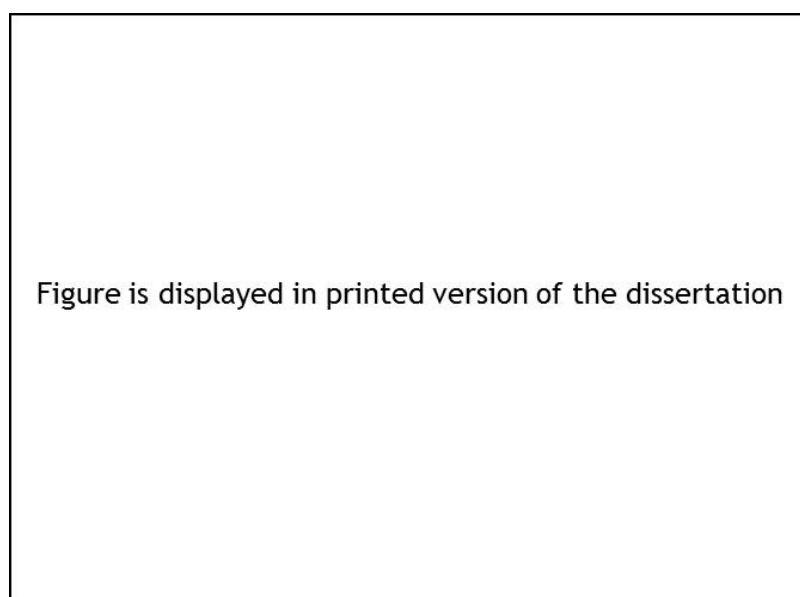


Figure 3-36: Benchmark Coimbra without roof (Rauch et al., 2007). © 2007, Chandos Publishing (Oxford) Ltd.

In this benchmark series memory requirements and run-time are of interest for the user of such software tools. Figure 3-37 displays the results for various mesh resolutions. Here the term 'patches' means the number of cells or the number of patches created if explicitly stated.

The RAM requirement for the view factor (VF) calculation for both commercial tools is negligible. Computer memory must be sufficient to store only the mesh. A totally different matter is the disk space (HD) to save the view factors. Theseus saves the lower triangular matrix of view factors including zeros as floating numbers by default (10). Thus, the memory requirements can be estimated in advance. A mesh with 71000 surfaces would require roughly 10 GB of space or more accurately the product of the number of cells times the number of cells minus one multiplied by two.

In the big O notation this means an order of two for the number of patches $N O(N^2)$. RadTherm, on the other hand, does not save zero entries and thus the size of the view factor file depends on the complexity of the geometry. The moderate increase in size between 14993 and 19056 cells can be explained by the mesh. The finer resolution was obtained by refining the dummy, keeping the surfaces of the cabin the same. The sizes of the view factor files also affect RAM requirements. Even though both codes use SOR for solving the radiative balances both load the whole matrix into memory at once, thus forgoing the main advantage of iterative solvers, namely memory savings. Consequently, about the same amount of RAM is needed allowing for some disk space for SOR.

Both programs offer patching as a means of avoiding too large memory requirements. In RadTherm each view factor is calculated individually and then put together with an area factor. Theseus puts cells together and calculates a common view factor. This results not only in memory savings but also in a significant calculation time reduction. On the other hand these patches form the basis of the energy balances which in terms of radiation means using a coarser mesh.

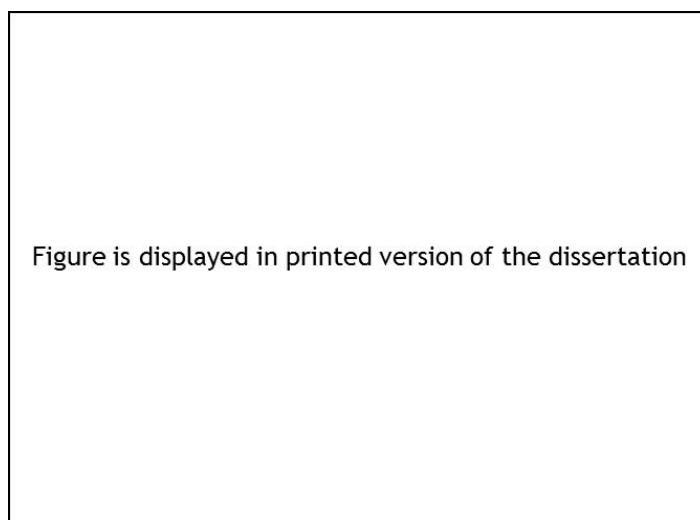


Figure 3-37: Memory requirements for Coimbra (Rauch et al., 2008). © 2007, Chandos Publishing (Oxford) Ltd.

According to Figure 3-38 the runtime for Theseus follows the order of the power of three, because it is programmed naively and does not employ any data structure.

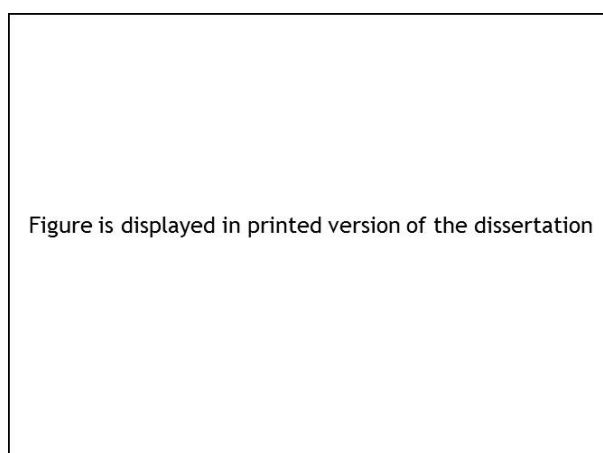


Figure 3-38: Run-time for Coimbra (Rauch et al., 2007). © 2007, Chandos Publishing (Oxford) Ltd.

The single point at 2909 patches is the runtime requirement for a patched case of the highest resolution mesh. RadTherm employs voxels, which are evenly spaced volumes resulting in a runtime behavior of the order of n or even $n \log_2 n$ which would be the best possible case according to current software engineering. In Figure 3-38 the curve for RadTherm actually possesses two slopes. Because the two cases with the highest number of cells consist of triangles only and RadTherm subdivides a triangle into three instead of four parts as it does for quadrilaterals, fewer rays are cast in total.

The CFD Code FLUENT also offers a surface to surface model. Consequently, a comparison with RadThermIR was made. The mesh consisted of a total of 58758 faces of a mixture of quadrilaterals and triangles. FLUENT offers the selection of the number of faces on the hemi-cube and the number of subdivisions for a face. RadThermIR offers the choice of the number of subdivisions and the number of rays cast from a sub-face. The mesh contains obstructions resulting in a less dense view factor matrix indicating when the two models have reached a similar level of accuracy because zeros are not stored. The more accurate, the more faces will actually be seen until the size of the view factor matrix does not change anymore. Given the time spent to calculate this matrix it can be seen that this approach is not practical. Therefore, a few settings were tried and the file sizes compared.

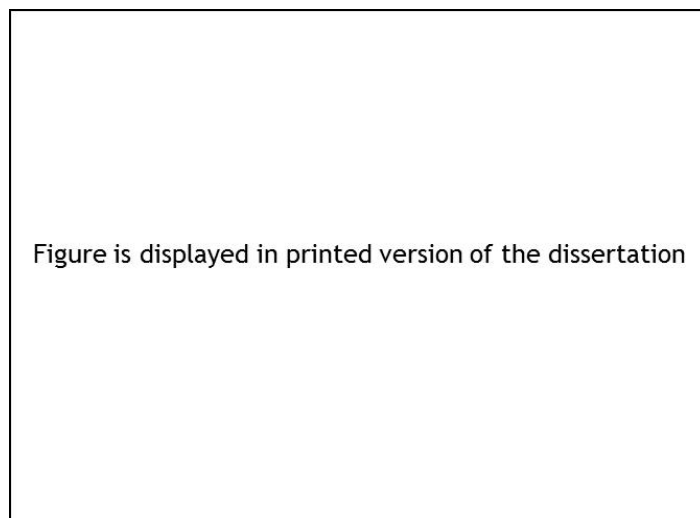


Figure 3-39: File size for Coimbra (Rauch et al., 2008a). Copyright © 2008 by ASME.

Figure 3-39 shows the binary file sizes for various settings. For FLUENT the first number signifies the number of faces of the hemi-cube. The second number represents the number of sub-faces. RadThermIR 9.0.1 was used with a setting of 2048 sub-faces and 4608 rays cast from each sub-face. RadThermIR has the biggest file size indicating the most accurate calculation. In FLUENT the hemi-cube faces have the most substantial influence on the results.

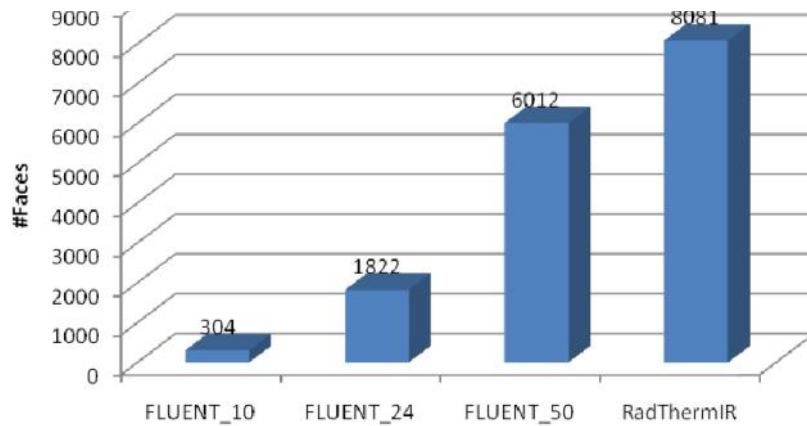


Figure 3-40: Number of face entries of face 58758 for Coimbra.

Figure 3-40 shows the number of faces seen from a particular face. The highest setting used for FLUENT comes closest to the number of faces recognized by RadThermIR.

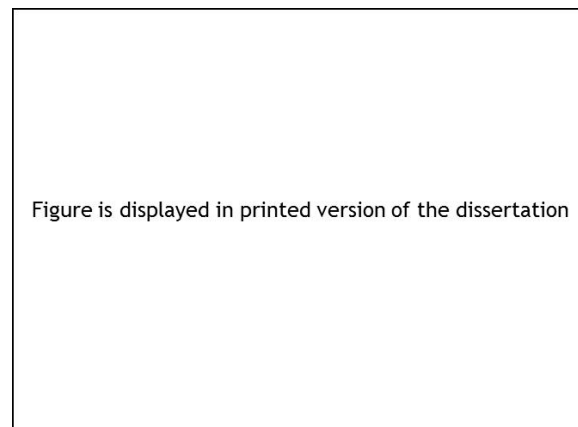


Figure 3-41: RAM usage for Coimbra (Rauch et al., 2008a). Copyright © 2008 by ASME.

The RAM usage for 4 CPUs shows that FLUENT occupies more memory with rising hemi-cube faces. RadThermIR mainly needs the memory for the file and a small overhead. When trying to increase the hemi-cube faces further, the memory per CPU exceeds 2 GB thus forfeiting the distributed memory ability, for many clusters are limited by their RAM per CPU. RadThermIR is more memory efficient but only available on shared memory process (SMP) systems.

The runtime for the view factor calculation is presented in Figure 3-42.

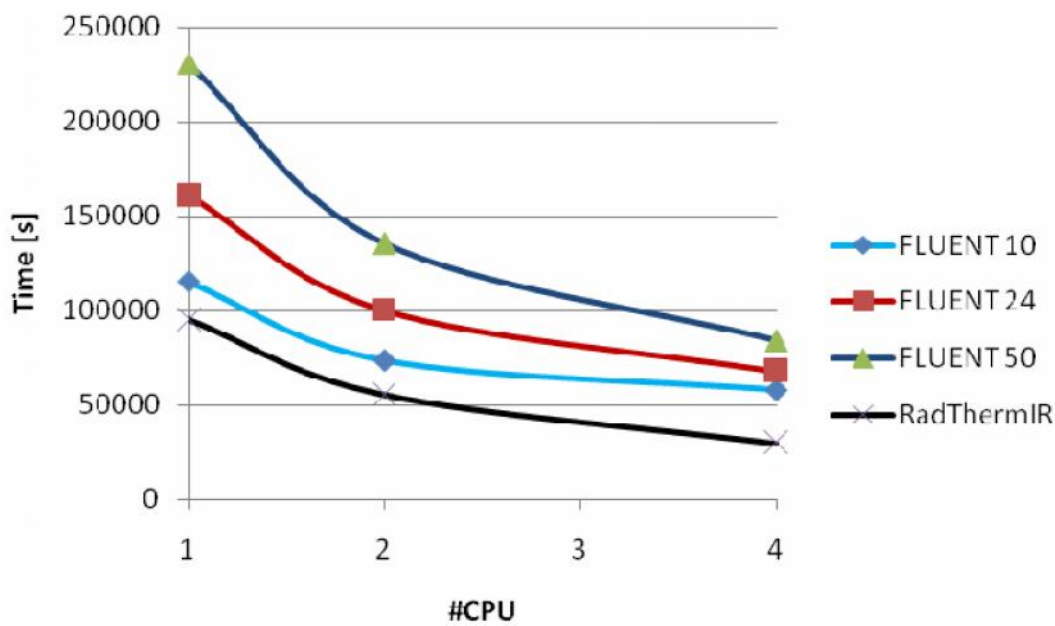


Figure 3-42: Runtime for Coimbra with FLUENT.

Although RadThermIR is able to detect more view factors it is considerably faster than the models in FLUENT. RadThermIR is able to finish within 8 hours whereas FLUENT 50_10 takes 23 hours for four CPUs.

FLUENT also offers a method using Gaussian quadrature for the view factor calculation. It is not only slower but also unable to calculate the benchmark presumably due to the quality of the mesh. In industrial applications a fast as well as a robust method is needed.

These findings show that specialized programs must be used and consequently coupling is necessary.

This chapter described diffuse view factors. In reflective materials such as heat shields and hydrogen tanks, directional view factors are more appropriate. Ambirajan A. et al. (2010) presented a directional view factor which is much more time-consuming to calculate than its diffuse equivalent. Therefore, directional view factors do not find use in everyday radiation simulation in the automotive industry.

Considering all the efforts in obtaining speedy and accurate view factors, the question remains just how accurate those factors need to be for each given situation.

4 Coupling of Thermal Systems

4.1 Introduction

In order to provide the research engineer with valuable tools some effort has been put into CAE development. A fundamental design question is whether all equations of the physical phenomena are to be solved together which is called the monolithic approach. Usually, better convergence is achieved but often the memory requirement is prohibitive and one has to write his own code. Alternatively, one can apply partial coupling, employing state-of-the-art commercially available software. This paper deals with this kind of approach. The following sections are concerned with a system requirements analysis and a proposed architecture. Following, a test drive is presented that, as a proof of concept, is being compared with calculation results using the coupling strategy described in this chapter by coupling a CFD code with a thermal radiation solver. Most thoughts have been published in Rauch et al. (2008; 2008a). It was the example in section 4.4 and more particularly Figure 4-10 that made me search for a systematic way of finding out just how much each parameter contributes to the results.

4.2 Systems Requirements

From the systems development point of view several issues have to be taken care of for a successful industrial application.

The first and foremost requirement is the automation feature of the coupling. Many programs provide an interface for exchanging files, but research engineers should be freed from the task of checking whether a program has finished its task in order to start another program with those results. Writing script files is a first approach to that problem. The problem with scripting lies in the fact that one has virtually no way of checking whether the calculation is performing as desired and to react accordingly. Also, one is limited to the feature provided by the program of importing files. Thus, a program has to be written, that recognizes the condition of the simulation software whether it has converged or an unprecedented error occurred and, consequently, is able to react in an appropriate way.

The second issue deals with files. Large files are difficult to handle. Especially ASCII files can become corrupted and thus interrupt the exchange of information. Avoiding those files would require a direct communication with the respective software tool. For this purpose an Application Programming Interface (API) is usually provided.

The third requirement is independence from using a specific code. There are solutions provided already such as the ANSYS Workbench, MDICE by CFDR, or EXA PowerFLOW. The disadvantage is of being pinned down to specific solutions and variables for data transfer provided by the developer. Simulation departments have good reasons to use their codes acquired over time. An industrial organization usually is focused on increasing gains and therefore, there is little inclination to spend money and time on new licenses, training, validation, and development of a new working methodology.

The next requirement is distributed simulation. One reason for distributing a calculation among different computers lies in having node locked licenses for specific codes or that the code was written on a specific platform, only. Another, more subtle, reason is memory usage. The present author showed in Figure 3-37 that the memory usage for thermal radiation codes is quite demanding. It can be seen that for cases of industrial size the memory need will rise extensively. Interestingly, the codes in Figure 3-37 do not offer parallelization for distributed systems. For this reason, these programs need to run on separate machines. There are parallelized radiation solvers, too, offered by CFD codes but usually they are better suited for radiation in participating media and less usable for large scale automotive applications such as the passenger cabin or the exhaust system. Therefore, a coupling tool should be able to communicate with the other program across a network.

There are systems available that will fulfill the requirements so far such as MpCCI. Another issue concerns the license for the data transfer system. It is desirable to forfeit extra expenses, since annual license fees are burdening research and development budgets.

Mapping of surface and volume data on meshes with different resolution is also a concern. Data should be transferred between the codes in such a way that not only the global balances of the whole system remain conservative, but also the local balances. For example, weighting factors help in achieving global conservatism when the sum of the weighting factors equals one. But this does not guarantee that on a local scale data is mapped on a surface or volume in a correct way because the individual weighting factor for a face could have been corrected for global conservatism's sake.

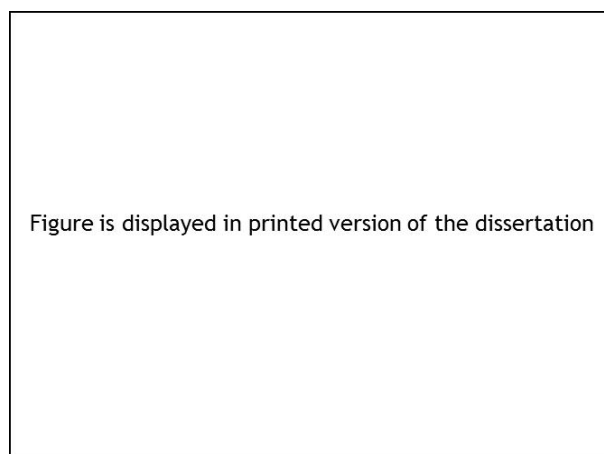


Figure 4-1: Differing mesh topology. (Heinstein and Laursen, 2003).

Figure 4-1 shows the dilemma. The two meshes have their discrete surfaces Γ_c^h . They distinguish themselves not only in their discretization but also in their topology. There are gaps and overlaps. The question remains, when do two surfaces still coincide. The difference in topology can occur, because different physics require different mesh resolutions.

Jiao and Heath (2004) gave a brief taxonomy on data transfer methods.

- (1) With a pointwise interpolation an interpolant is created from available data. Consistent interpolation creates a function of the same order as the source function, whereas alternative interpolations uses basis functions of higher order than the source basis function. A disadvantage is that most interpolation methods are not conservative.
- (2) Area-weighted averaging evaluates intersections, sometimes with integration. This form is the simplest conservative method.

- (3) Mortar element methods chose one interface as the mortar side. The non-mortar side sends data to the mortar side by weighted residuals.
- (4) Common-Refinement-Based method refines both meshes, so that for each vertex on one mesh there is a corresponding vertex on the other mesh.

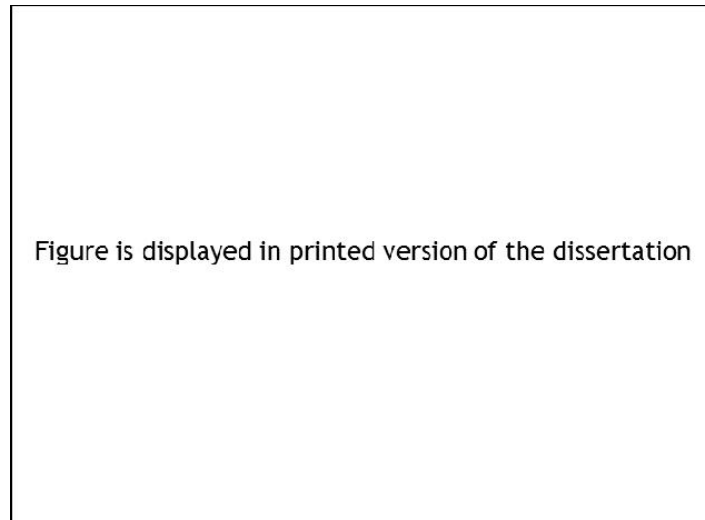


Figure 4-2: Common refinement mesh. Copyright © 2004 Wiley. Used with permission from (Jiao and Heath, 2004).

These considerations have significant practical implementations for the automotive industry.

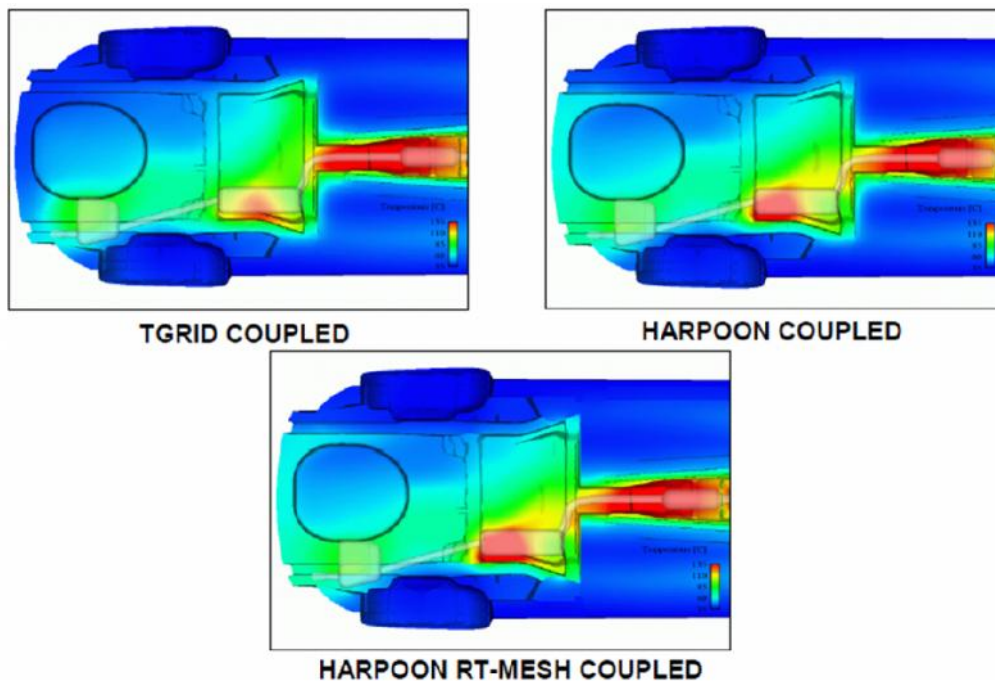


Figure 4-3: Underbody temperatures with coupling (Tastan, 2008).

Tastan (2008) showed a coupling between a CFD code and the thermal radiation solver RadTherm. As a coupling tool MpCCI v3 was used. Figure 4-3 top left shows the result of the coupling, when TGrid was employed for the CFD mesh and RadTherm surface grid was meshed in ANSA. Top right shows the results with Harpoon used for the CFD grid. The bottom picture used Harpoon for both meshes. Tastan (2008) reported differences in the results of up to 20 K.

The next requirement that would benefit in coupling simulations with different time step sizes or significant step changes in the boundary conditions would be the ability to couple the systems in an implicit way. Thus, if there is a change in the values in between time steps the coupling tool should be able to repeat a certain time step with more time accurate boundary conditions. Valli et al. (2008) investigated the coupling of multi-physics systems and stated that in the case of nonlinear couplings a pseudo transient approach might be more effective than it solving the stationary equations iteratively. In this way larger time steps to steady-state, that do not yield time-accurate solutions, might promise faster convergence.

It also should be possible to send data of different dimensions such as arrays and tensors, data with and without a connection to geometry, such as spray, and without the need for a specific ordering of the data. By that it is meant that some codes order the data in a relative way on each processor without disclosing an absolute index for an entity. In that case data should be able to be sent in a relative context such as for each processor.

The last significant requirement for a successful coupling between two codes is its ability to handle large amount of data that is parallelized in an efficient way.

If we sum up all the requirements a system is considered to be desirable if it can handle the coupling automatically, without writing and reading large files. It should be independent from any specific code, with the ability to communicate with computers on a network. Additionally, it should cost little or nothing at all in terms of license fees. The conservative mapping of data on a local and global scale for different mesh resolutions is a must. It should offer the option of implicit coupling, transferring data of different dimensions, and handle large amount of parallelized data.

4.3 Coupling Architecture

The authors have worked on a coupling between the CFD code FLUENT 6.3 and RadThermIR 8.1.1, and later version 9.1, which is a thermal radiation solver. In order to meet the requirements mentioned above, a software architecture was designed, as depicted in Figure 4-4.

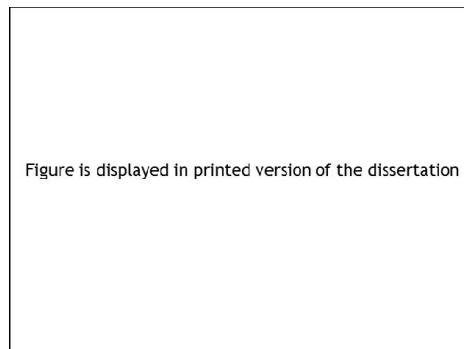


Figure 4-4: Component diagram of coupling architecture (Rauch et al., 2008). Reprinted with permission from SAE Paper No. 2008-01-0389 © 2008 SAE International.

In the component diagram three big components can be seen. On the right hand side the coupling interface for RadThermIR is shown as component 'RadThermInterface'. On the left hand side the component 'FluentInterface' is drawn to represent the interface for Fluent. In the center a certain data transfer tool with the name 'ACCI' developed by AVL is shown. Its purpose is to transfer data between the interface components. It has the ability to transfer data of various dimensions at certain time or iteration steps and provides 3D surface and volume mapping by area-weighted averaging. It does not use files and communicates with anyone applying the interface as named 'ACCI' by network communication. At the time of development, the coupling tool required no separate license and was able to be employed for parallelized tools. Therefore, ACCI was chosen for the basic exchange of data. But it should be mentioned that other exchange tools such as MpCCI could be used in principle, as long as the necessary features are supported or added by the user.

All that is left to do is to describe the interfaces. The idea is to split the component 'RadThermInterface' and 'FluentInterface' into two components as shown in Figure 4-4. This splitting enables implicit coupling. Since neither FLUENT nor RadTherm offers the feature to redo a calculation of a time step one has to break off the calculations and do a restart at the appropriate time step. If one

would employ a traditional data transfer tool such as ACCI the stopping of one code would cause the other code to be stopped as well. Now, the respective server interface has the responsibility to keep in touch with ACCI. Therefore, a stopping of the client does not necessarily lead to a termination of the coupling procedure.

Other duties of the server are the communication with the client, starting the code to be coupled, and checking whether the boundary conditions are good enough and to interrupt the calculation if necessary.

When we turn our attention to the deployment diagram of Figure 4-5 we see how the objects that are part of the components of the FLUENT interface are distributed.

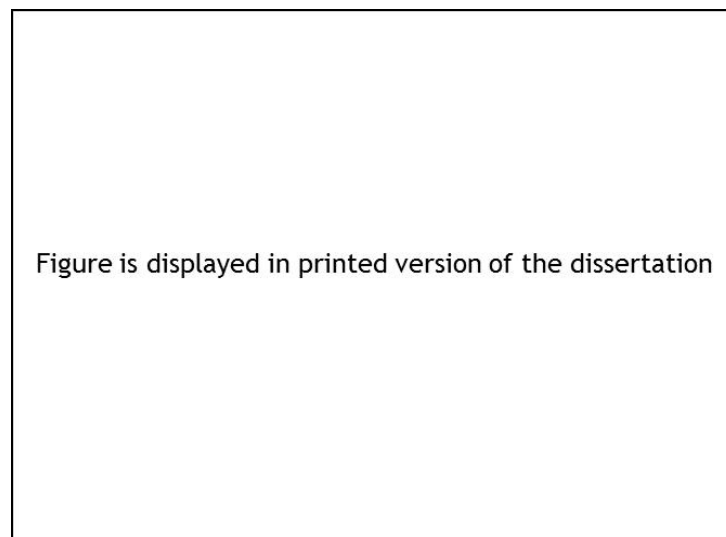


Figure 4-5: Deployment diagram for the standard FLUENT interface in parallel (Rauch et al., 2008). Reprinted with permission from SAE Paper No. 2008-01-0389 © 2008 SAE International.

FLUENT creates a host process when it is run in parallel and the desired numbers of compute nodes are being created. Each compute node and the host call the subroutine which generates objects of the client interface. In Figure 4-5 a sample object is shown of this component as working on each node and the host.

The server interface communicates with the host by special pipes called “FIFOs” and shared memory (SMP). This is possible because the host process always runs on the cluster node with the client server.

The host can send messages to all the compute nodes but only node zero can send messages to the host. If one wants a piece of information from a node, the host

sends a query to all compute nodes. The appropriate node fetches the information and sends it to node zero which in turn delivers it to the host. This indirect communication is very time consuming and was applied by the prototype of the client interface, only. It has been proven to be too slow for large applications due to the massive amount of inter-process communication.

Figure is displayed in printed version of the dissertation

Figure 4-6: Deployment diagram for the parallel architecture (Rauch et al., 2008a). Copyright © 2008 by ASME.

The reason rests in the massive amount of inter-process communication. Referring to Figure 4-6, FLUENT starts a host process which does not do any calculations on its own. The compute nodes are doing this.

Node 0 is responsible for communicating with all other compute nodes and transferring their data to the host. This approach slows down the data exchange,

significantly. Therefore, a new architecture for parallel runs was devised. Now, the client interface has an additional responsibility. It has to start its own slave server. Each compute node communicates now with its own slave server. The slave server has the responsibility of the original server interface with the exception of not starting the CFD code anymore. The original server interface is now called master server interface with its duty of starting the CFD code and checking for a restart.

Only when initializing the slave server this architecture employs message passing for a view bytes of data. After that MPI is not used by this interface thus reducing inter-process communication drastically. Since ACCI now starts a process for each compute node each slave server can transfer data of the node without waiting for other nodes. Also, data management has been eased, because FLUENT uses relative cell, face, and vertex numbers. With the original proposal an absolute index had to be stored for faces and cells. Now, only relative vertex indices need to be handled with care.

4.4 Test Case

A series of measurements have been conducted for validation purposes. The test car is a BMW X3 3.0 D SUV. The exhaust system has received numerous thermocouples of type K with a wall thickness of 1.5 mm to assure that the wall temperature is being measured. Those thermocouples have been placed in such a way that one sensor is attached on the exhaust pipe looking to the ground 'Bot', one sensor being attached to the pipe facing the floor pan 'Top', and one sensor being attached to the floor pan facing the sensor on the pipe. In that way one can get insight into the temperature distribution fairly well. An overview of the locations of the sensors at the exhaust system is depicted at Figure 4-7.

Figure is displayed in printed version of the dissertation

Figure 4-7: Measurement points for the exhaust system (Rauch et al., 2008a). Copyright © 2008 by ASME.

The track chosen was a section of a highway of about 19 km on the 23rd June 2006. The track is without any significant inclinations. At one point of the track the temperature of the lane was given with 280.15 K and the air temperature was measured to be 287.25 K. The sky was clouded and the lane dry. A lambda probe together with the measured exhaust gas temperature TAGnKAT with 679.71 K gave a calculated mass flow of 0.07 kg/s with a specific heat capacity of 1.12 kJ/kg/K. The car was driven at a speed of 130 km/h without switching on the HVAC system. For each of the measurement points a thermocouple had been placed on the bottom of the tube facing the road which is named 'Bot'. The thermocouple opposite to it and facing the heat shield is named 'Top'. Finally there is a sensor placed on the heat shield opposite to the one just mentioned described as 'Plt'.

4.5 Simulation

In order to apply the described systems architecture a simulation run is conducted and compared with the measurements. The volume mesh of the car aerodynamics consists of 12 million volume cells created by SPIDER an automated unstructured mesh tool. In Figure 4-8 the surface mesh of the coupling selection is shown to demonstrate how well the actual surface is resolved.

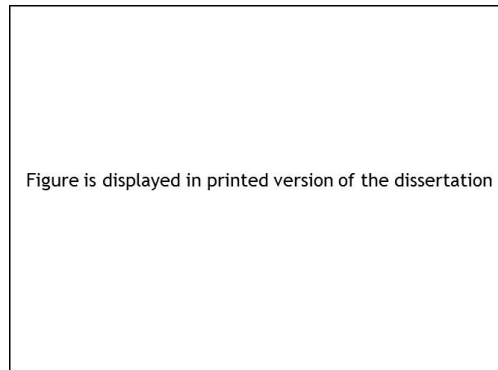


Figure 4-8: CFD coupling interface (Rauch et al., 2008a). Copyright © 2008 by ASME.

Before starting the coupled run a cold run was being conducted to speed up convergence and give estimates for the initial conditions. The CFD code FLUENT 6.3 was used with the realizable $k-\varepsilon$ turbulence model and the enhanced wall model which was found to be quite satisfactory for heat transfer calculations of industrial sized problems with a y^+ above 5. In order to employ SST or $k-\omega$ mesh refinement would have been necessary for decreasing y^+ below 5. The convergence condition for the turbulent energy was set to 10^{-4} . The inlet velocity was taken as 36.1 m/s and the FLUENT fan model with an intake of 1.55 kg/s at 373 K was chosen in order to estimate the velocity distribution in the engine compartment which in turn affects the flow situation at the floor pan. This value for the intake reflects the author's experience in taking into consideration the characteristic curve of the fan. The run was done in steady state. The results of this run were fed into the coupled simulation as an initial condition for the transient run. 60 time steps with a time step size of 0.005 and a maximum of 25 iterations were calculated where the coupling happened to be at every twentieth time step. The convergence rate for the energy balance was set to be 10^{-9} . The coupling interface consisted of 1.1 million surface faces at the lower half of the car.

The upper half of the car is considered to not affect the energy balance around the exhaust system since no heat source terms for the passengers or solar irradiance were considered. FLUENT provides for the convective heat transfer coefficient and the corresponding fluid temperature at the first cell next to the face. Also, the face geometry is retrieved by the coupling interface at the beginning as required input for the mesh mapping. In turn it imports the wall temperature provided by RadTherm.

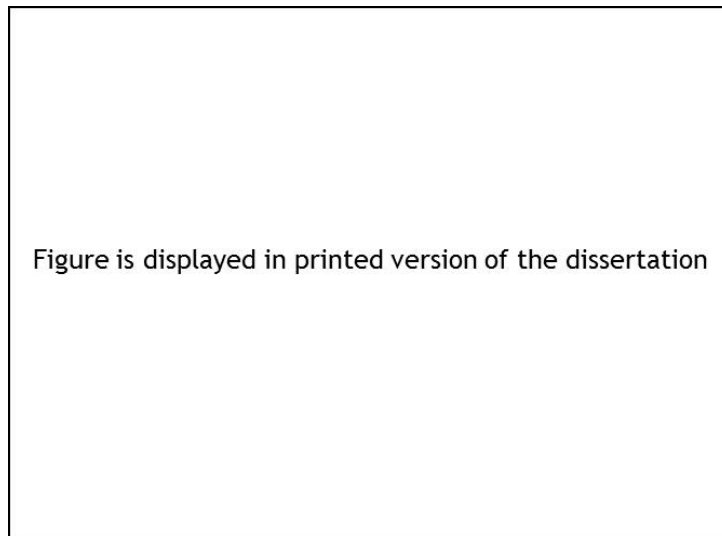


Figure 4-9: RadTherm coupling interface (Rauch et al., 2008a). Copyright © 2008 by ASME.

RadTherm on the other side provides for the wall temperature values and imports the convective heat transfer coefficient and fluid temperature of FLUENT. RadTherm actually performs the energy balance for the walls. For this run surface temperatures of the aforementioned measurements were set on the pipe. RadTherm interpolates temperatures along the exhaust system from those points. An emissivity factor of 0.7 was presumed and a constant road surface temperature of 280.15 K was used. The convergence parameter of 0.01 K was chosen for the wall temperatures. The exchange surface consisted only of the lower part of the car since the sun was not modeled as it was hidden by clouds. There were 340,000 faces created by VisCART v2006.

FLUENT with its interface, RadTherm and its interface, and the ACCI server were all located on different machines. The FLUENT mesh was distributed among 8 CPUs. RadTherm was run on two CPUs as a shared memory process.

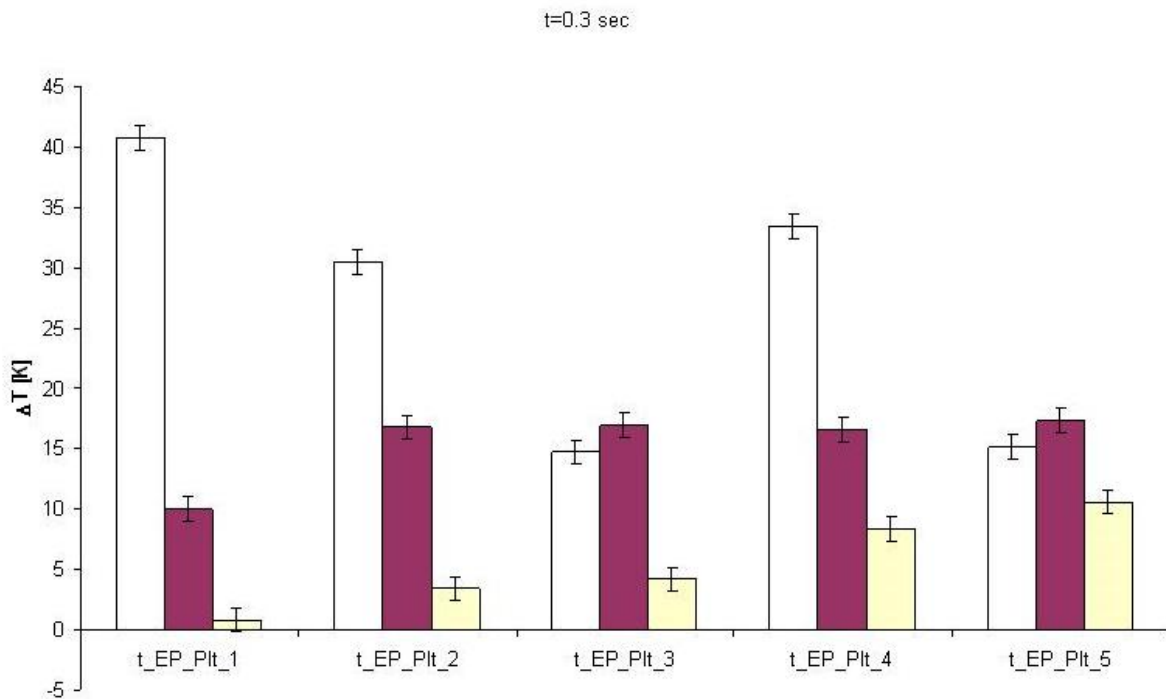


Figure 4-10: Temperature differences of measurement and simulation at the floor pan heat shield.

The results of the coupling for sensor positions at the floor pan heat shield are shown in Figure 4-10 for the third time step. Here, e.g. t_EP_Plt_1 signifies the sensor on the floor pan heat shield facing t_EP_Top_1 in Figure 4-7. Because of the explicit nature of the coupling with three time steps only three updates at the coupling interface were being performed. After examining the geometry close to the position where the connector pipe is breaking through the floor pan it was found that the coarse mesh for the radiation solver was connected to the floor pan at the catalytic converter resulting in an unrealistic high temperature distribution both at the floor pan and the sensor on the pipe opposite to the floor pan. There was also a high input via conduction at the pipe clamp of the kick-up pipe giving to high temperatures for t_EP_Plt_4. The unwanted thermal conduction was prevented by setting the thermal conductivity coefficient almost to zero where unwanted mesh connections occurred. This resulted in the red bars of Figure 4-10.

Another issue was choosing an appropriate emissivity factor. Therefore, thermographic pictures were taken after a test drive. Emissivity stickers for calibration purposes were attached and the temperatures measured. When adjusting the camera to the temperature of a thermocouple one obtains an emissivity factor.

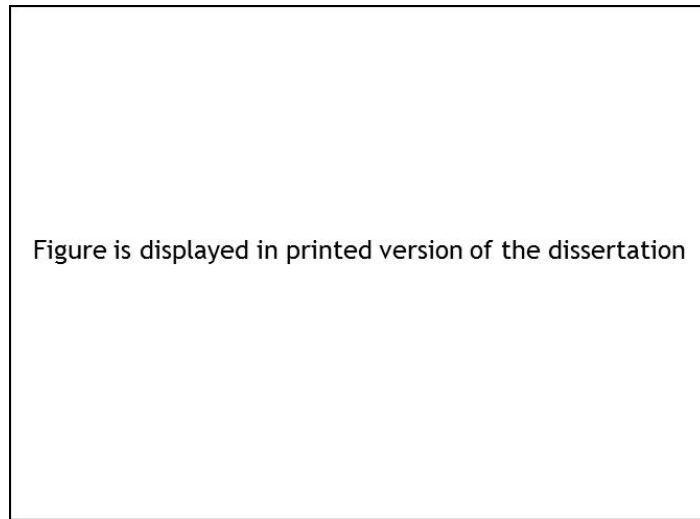


Figure 4-11: Thermographic image of connector pipe (Rauch et al., 2008a). Copyright © 2008 by ASME.

Figure 4-11 shows the very in-homogenous temperature distribution. One gets the following emissivities ε for the encircled values in Table 4-1:

A rectangular box with a black border, containing the text "Table is displayed in printed version of the dissertation". The box is empty of any data or figures.

Table 4-1: Emissivity coefficients of the connector pipe (Rauch et al., 2008a). Copyright © 2008 by ASME.

It can be argued that with this method, heat losses from convection and complicated 3D conduction is neglected. This is indeed the case. Nevertheless, this method provides much better values for complex geometries than textbooks do because one gets the values at the actual temperature needed including soiling and current level of corrosion.

Since RadTherm can only set one emissivity value for each selection and the number of selections is practically limited, the authors chose to set a value of 0.75 for the exhaust tubes and mufflers and a value of 0.4 for the heat shield. These corrections resulted in the yellow bars of Figure 4-10.

Increasing the complexity of the coupling the interpolation of measured temperatures on the exhaust pipes were replaced by a third coupling client.

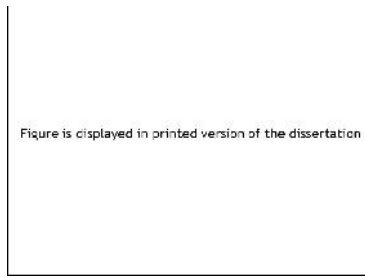


Figure 4-12: Volume mesh of the exhaust system (Rauch et al., 2008a). Copyright © 2008 by ASME.

The exhaust system consisted of 666,000 cells and 83,000 boundary faces. The mesh is being shown in Figure 4-12. It was resolved with 5 boundary layers. Since no temperature profile was known, an average temperature of 592 K was used. For this purpose the average of $t_{OCC_CON_1}$ in Figure 4-7 with 504 K and TAGnKAT was calculated. The realizable $k-\epsilon$ turbulence model was chosen with 60 time steps of time step size 0.005 s. FLUENT 6.3 was used.

The original architecture in *Figure 4-5* took 13 minutes for exchanging 100,000 values because of the message passing bottleneck. The new architecture in *Figure 4-6* can do this well under one second giving a speed-up of more than 7,000 for the actual data exchange.

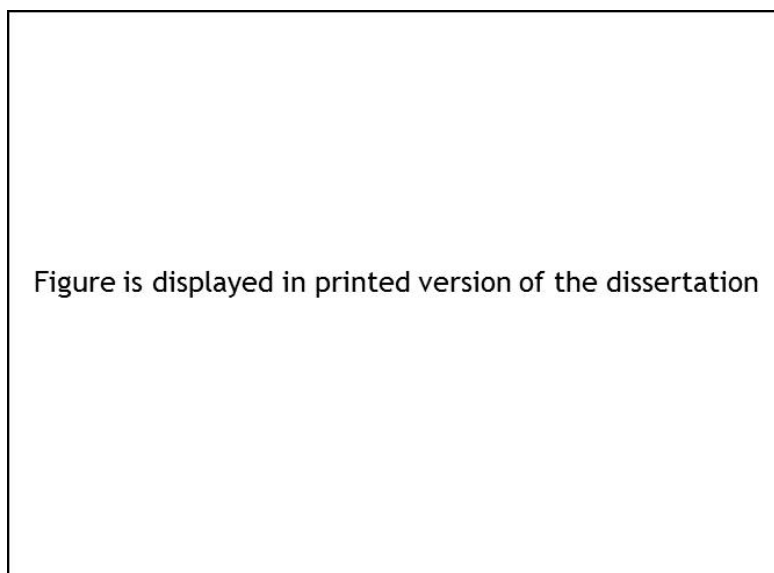


Figure 4-13: Simulation temperature differences to measurements at the floor pan heat shield (Rauch et al., 2008a). Copyright © 2008 by ASME.

The heat shield temperatures at the connector pipe correspond well with measurements.

The temperatures at the height of the kick-up pipe show greater discrepancies. Because of the third coupling client the system takes more time for convergence.

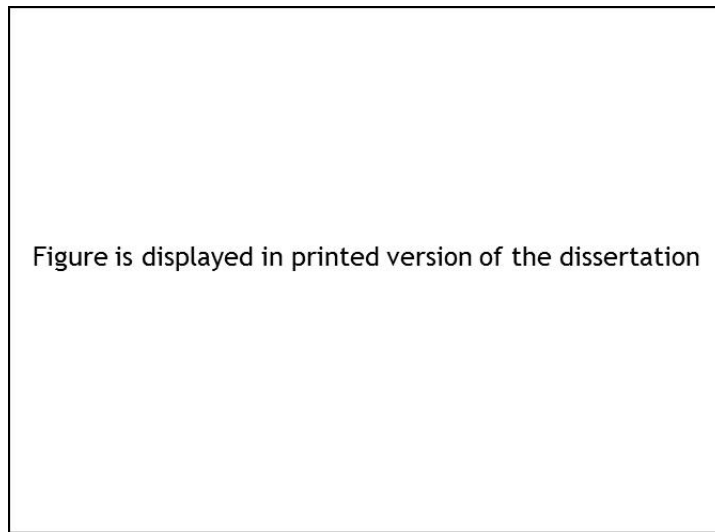


Figure 4-14: Simulation temperature differences to measurements at the exhaust pipe facing the road (Rauch et al., 2008a). Copyright © 2008 by ASME.

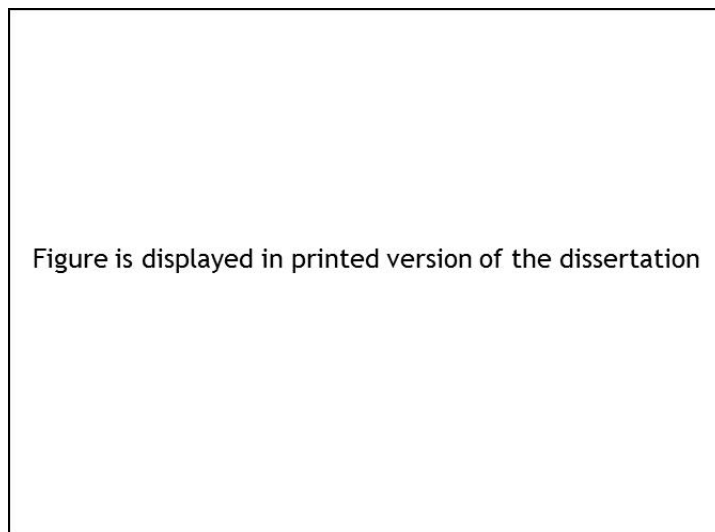


Figure 4-15: Simulation temperature differences to measurements at the exhaust pipe facing the heat shield (Rauch et al., 2008a). Copyright © 2008 by ASME.

Since the last results do not show satisfactory results another coupling run was performed. This time, the heat of the main water cooler was included with 31 kW. This means, that a warm stationary calculation for initialization was done. Additionally, the thermal inertia of the solid was removed by assigning a zero specific heat capacity to all the surfaces in RadTherm. In this way, the results are less dependent from initial guesses. 200 time steps were calculated and after every other time step a coupling performed.

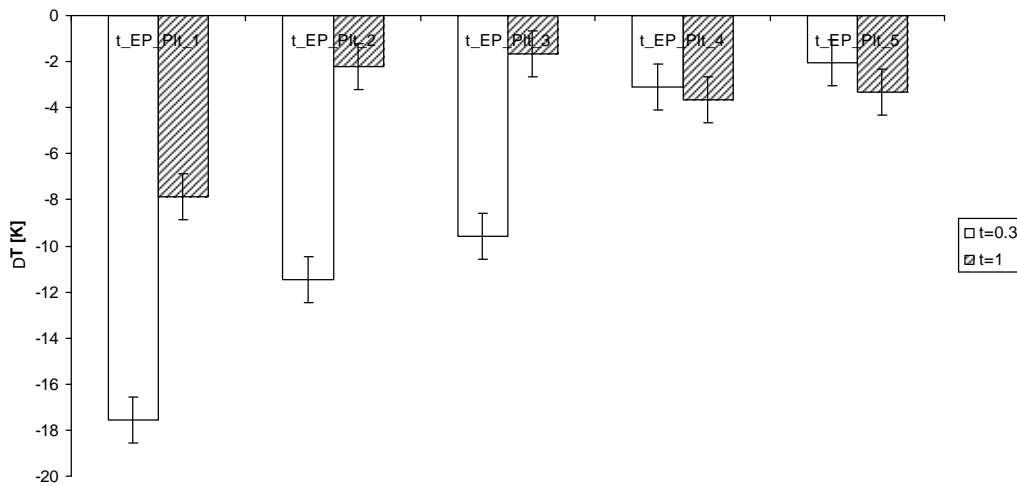


Figure 4-16: Simulation temperature differences to measurements at heat shield for $c_p=0$.

Compared to Figure 4-13 results show great improvements and a trend of lower levels of error at the connector pipe.

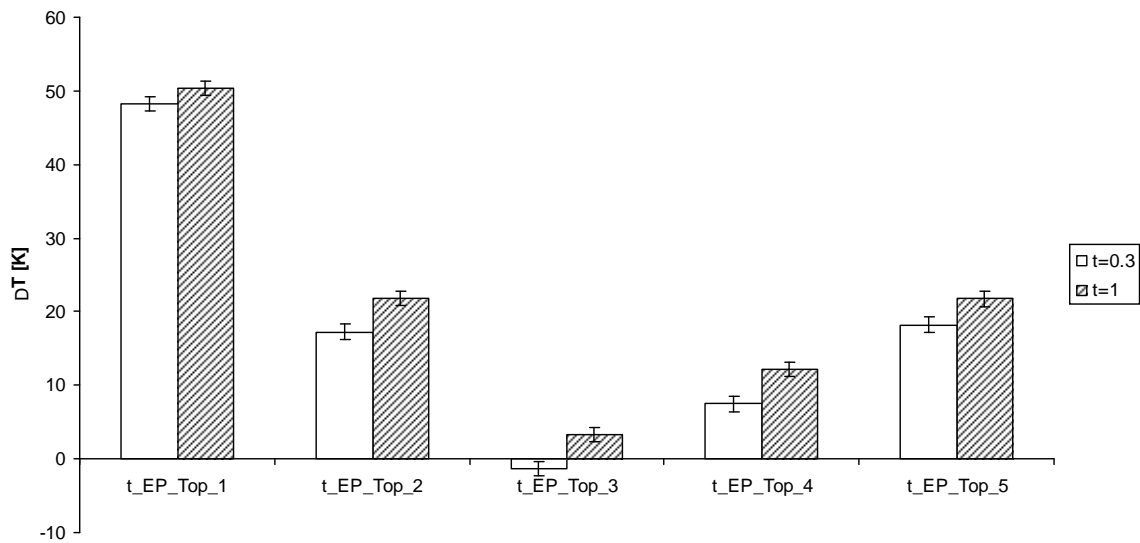


Figure 4-17: Simulation temperature differences to measurements at the exhaust pipe facing the heat shield for $c_p=0$.

Figure 4-17 shows the greatest deviations from measurements. Compared to Figure 4-15 the overall results have been improved with the exception of the first measurement location.

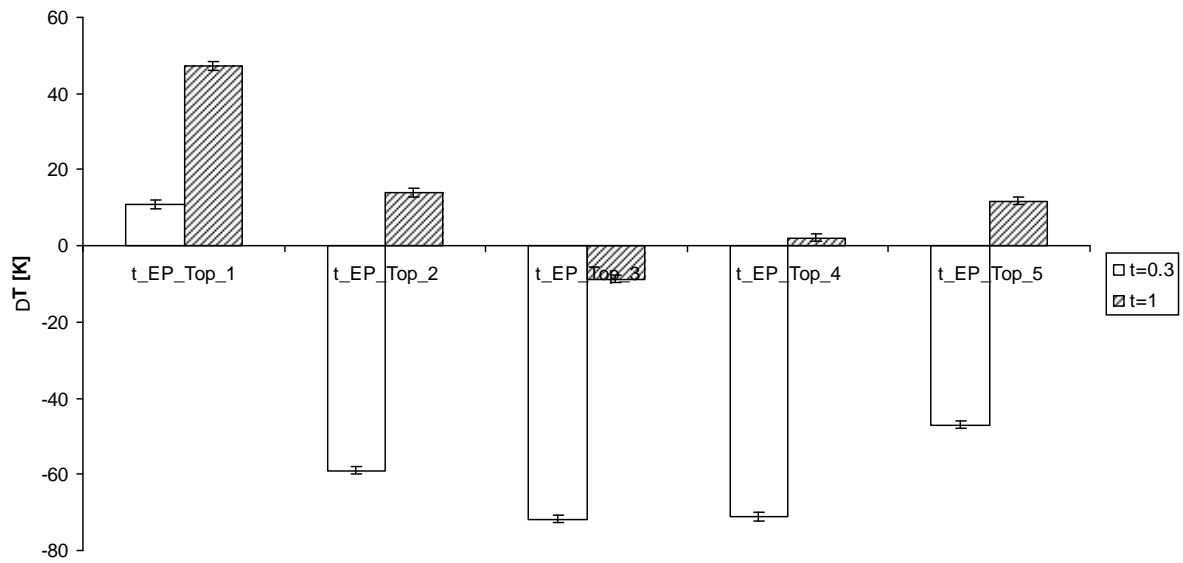


Figure 4-18: Simulation temperature differences to measurements at the exhaust pipe facing the heat shield for $c_p=0$ and coupling time step of 0.02 s.

The last figure shows the results when the coupling is done every 20 time steps. This figure suggests that it is better to use greater coupling time steps. The fact, that after one second simulation differences are actually increasing suggests that convergence has not been achieved.

The results of this test case, especially Figure 4-10 raises the question, what parameters deserve more attention in order to improve coupled simulation results.

5 Sensitivity and Uncertainty Analysis

It is in the interest of the thermal simulation engineer to estimate how well his predictions coincide with the real system. Unfortunately, measurements are expensive and not always feasible. Also, there is a need to understand the entire system at hand, for the number of measurements is limited and the thermal behavior of the complete system should be known. A convergence in one place does not necessarily guarantee the convergence in the whole realm of investigation. For example, there might be numerical diffusion, or the nonlinear behavior of thermal radiation dominates, locally. Therefore, the purpose of this chapter is to introduce sensitivity and uncertainty analysis.

5.1 Taxonomy

According to Saltelli et al. (2008) “*sensitivity analysis studies the relationship between information flowing in and out of the model*”. Closely related to sensitivity analysis is uncertainty analysis, which seeks to quantify uncertainties in the response as a consequence of uncertainties in the model input. In other words, it is investigated how uncertainties are propagated from the input to the output of a model.

There are various reasons for using sensitivity analysis.

- (1) Model Validation: It is investigated, whether all significant effects are taken care of and whether some parameters are just tuned in order to suit the proposed model in a way that is not physically justified.
- (2) Most Influential Model Parameters: The parameters that affect the model the most are identified. It can serve as a guide for measurements.
- (3) Insignificant Model Parameters: These are parameters that might be eliminated from the model.
- (4) Locating the region of parameters that vary the model output the most.
- (5) Which regions of the parameter space to use for calibration.
- (6) Determining the Interaction of parameters.

Espinar et al. (2009) refer to the General Law of Uncertainty Propagation according to an ISO standard. It introduces the following notation for uncertainties:

$$u_c(y) = \sqrt{\sum_{s=1}^N \left(\frac{\partial f}{\partial x_s} \right)^2 u^2(x_s)} \tag{Eq. 5-1}$$

Here, $u_c(y)$ is termed the combined standard uncertainty (CSU) of y , y being the result of the function f and N input parameters x . The partial derivative $\partial f / \partial x_s$ is the sensitivity coefficient and describes how y varies with a change in x_s . If all variables are used for uncertainty calculations CSU is called total CSU, partial CSU otherwise. The term $u(x_s)$ is called standard uncertainty (SU). In Type A uncertainties this term is derived from statistical analysis such as a probability distribution function. A Type B uncertainty is non-statistical. Expert knowledge, look-up tables, or analytic solutions are used for the SU quantification. Espinar et al. (2009) explain the term uncertainty as “... an estimate of the likelihood of nearness to the best value that is consistent with presently available knowledge”.

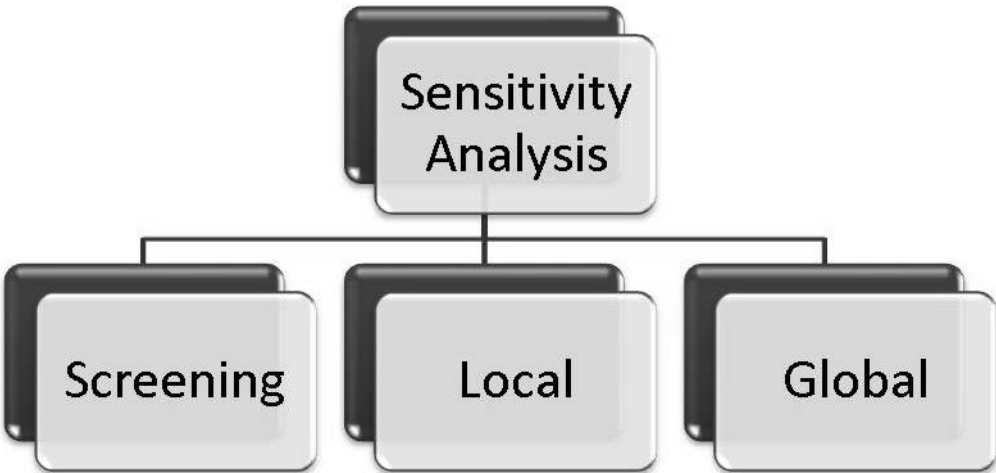


Figure 5-1: Taxonomy of sensitivity analysis.

Following the taxonomy of Saltelli et al. (2008) sensitivity analysis (SA) can be categorized into screening, local, and global SA. It should be noted, that screening could as well be attributed to local and global SA. Thus, this taxonomy represents the opinion of Saltelli et al. (2008) and is subject to change in this young discipline.

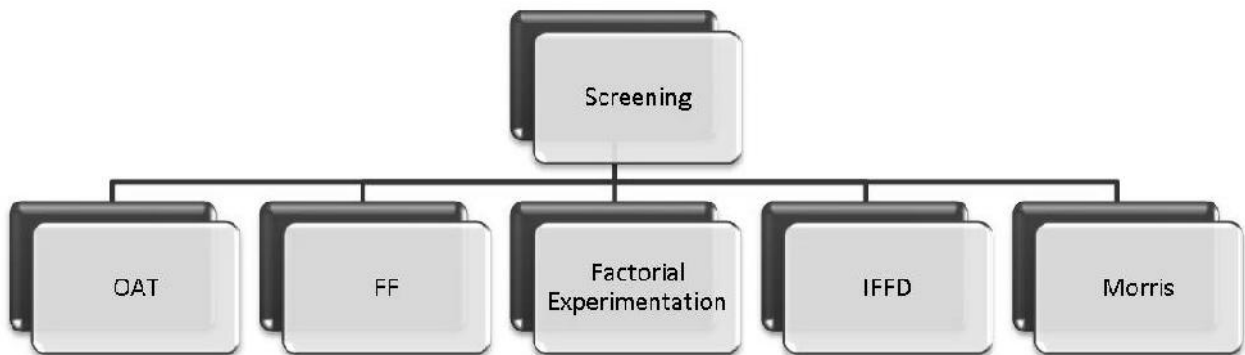


Figure 5-2: Taxonomy of screening.

Screening is employed when dealing with a large factor space, where factors can be parameters from outside the model or variables inside the model. It seeks to reduce the number of calculations. The disadvantage is that they only yield qualitative results in ranking the input factors according to their importance. The most basic one is one-at-a-time (OAT) approach, where one factor is changed and the outcome calculated at a time. Opposed to it is Factorial Experimentation in which all factors are perturbed simultaneously in a way that all possible values are covered. Because full factorial simulations often are too time consuming fractional factorial (FF) only examines some of the possible interactions. Even more aggressively, the iterated fractional factorial design (IFFD) prescribes a set of statistical simulation runs that reduce the number of required simulation runs to less than the number of factors under investigation. Morris performs randomized OAT runs in such a way, that the entire factor space is covered.

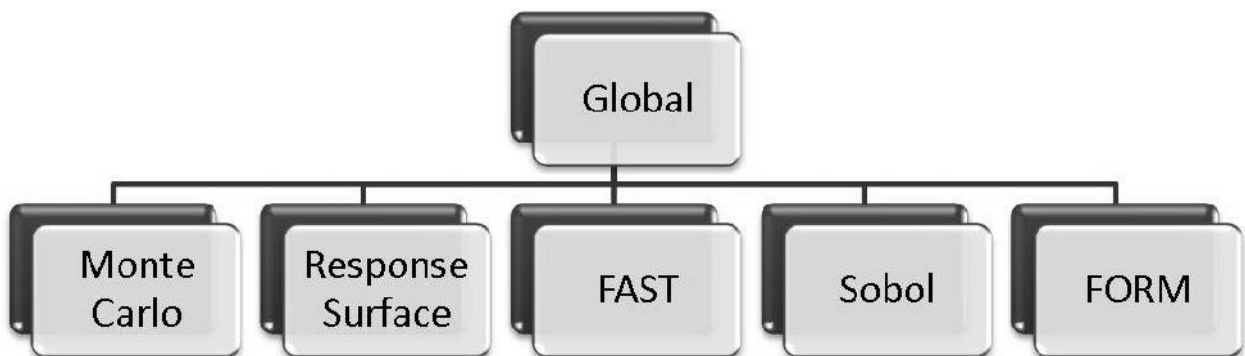


Figure 5-3: Taxonomy of global SA.

Global Methods differ to screening methods in that they calculate uncertainties, thus providing a quantitative analysis. Monte Carlo analysis performs simulations with randomly selected input parameters. From the results uncertainties in form of expected values and variances are calculated and correspondingly apportioned to the input parameters by sensitivity analysis. Sobol's method decomposes the parameter space into summands of increasing dimensions. Therefore, the variance can be decomposed, as well. Each summand is computed by Monte Carlo integration. With the variances known sensitivity factors are estimated.

The Fourier Amplitude Sensitivity Test (FAST) also calculates the same sensitivity indices as Sobol's method. A multidimensional integral over the entire parameter range is transformed to a one-dimensional integral by scanning the whole parameter range with a single frequency for each parameter. The fractional sensitivities are obtained by Fourier decomposition.

The response surface methodology is very similar to Monte Carlo with two distinctions: First, there are no probabilistic weights assigned to the factors for determining the simulation runs. Second, a response surface is constructed from the simulations results from which uncertainties are calculated.

The First-Order Reliability Method (FORM) deals with a hyper-surface of input parameters that should not exceed a certain value.

An interesting derivative of a Monte Carlo simulation, called subset simulation, provided Thunnissen et al. (2007), recently. When the task is to quantify uncertainties in the extreme ranges such as critical component temperatures for failure analysis, it is advantageous to express a small failure probability as a product of larger failure probabilities. First, a screening is done by Monte Carlo and the responses sorted. A threshold level is selected that reduces the parameter space for further calculations. In the next refinement level 1 a series of Markov Chains determine the next simulations. The goal is to limit the parameter space in such a way that higher values on the ordinate are reached. With each level, smaller failure estimates on the abscissa are reached for subsequently more critical response values, assuming normal distribution. In this way, a significant reduction in model evaluations can be achieved compared to Monte Carlo analysis.

Figure is displayed in printed version of the dissertation

Figure 5-4: Subset simulation procedure (Thunnissen et al., 2007). Copyright © 2006 by AIAA, Inc. Reprinted with permission of the American Institute of Aeronautics and Astronautics.

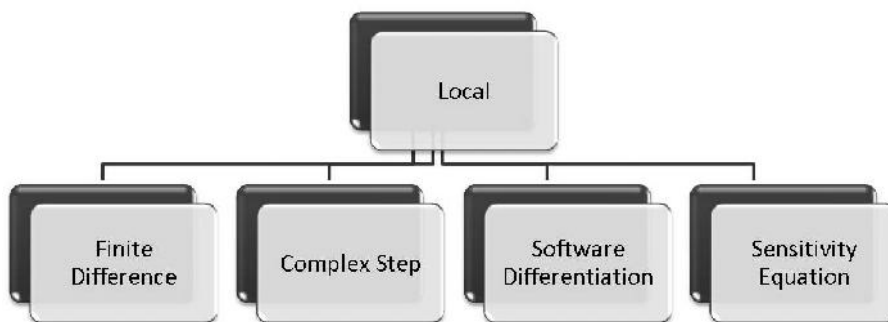


Figure 5-5: Taxonomy of local SA according to Blackwell and Dowding (2006).

In local methods the sensitivity coefficients are calculated for a specific parameter set instead of covering the entire parameter space as in global methods.

According to Blackwell and Dowding (2006), the finite difference method seeks to approximate the derivatives by finite differences in a post processing step. For each

parameter it needs an additional simulation. The derivatives are dependent on the step size change. In order to circumvent the step size issue the complex step method treats the equations in the complex plane. By automated software differentiation a compiler does the differentiation from the source code. In the sensitivity equation method the equations are differentiated manually.

Lange and Anderson (2010) choose to further classify the last method mentioned in continuous, where the derivatives are first derived and then discretized, and discrete, where the governing equations are first discretized and then differentiated.

An increased measure of complexity adds the consideration of spatial data. Phillips and Marks (1996) considered an evapotranspiration model over a certain region. Since data of three input parameter were available only at discrete locations, these data sets were interpolated by kriging. The resultant uncertainties were determined by calculating 100 Monte Carlo simulations for each grid point. Watanabe et al. (2010) used a parallelized finite element method (FEM) formulation for coupled heat, fluid flow, and solid displacement. Because spatial and time dependant parameters over a long time period were considered, a screening Monte Carlo procedure limited to 10 runs first determined the most influential parameters. Then, more Monte Carlo runs followed with the parameters just obtained.

When considering time dependant sensitivity coefficients, two methods are mentioned by Lange and Anderson (2010). In forward mode direct differentiation the sensitivities are calculated as the solution advances in time. The reverse mode adjoint method starts with the last solution in time and recedes in time for each sensitivity coefficient. Lee et al. (2003) solved the governing equations and sensitivity equations simultaneously as a set of ordinary differential equations (ODE). Korycki (2010) used a finite element method (FEM) formulation for an objective heat and mass transport optimization using the adjoint sensitivity method. Recently, there has been made a distinction between aleatory and epistemic uncertainties.

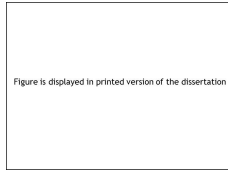


Figure 5-6: Epistemic and aleatory uncertainty (Guo and Du, 2007). Copyright © 2007 by AIAA, Inc. Reprinted with permission of the American Institute of Aeronautics and Astronautics.

Aleatory uncertainties are stemming from measurement uncertainties or other irreducible uncertainties. They are being described by random variables or probability theory. Epistemic uncertainty, on the other hand, describes a lack of knowledge which can be reduced if further investigations are being conducted. It is often associated with the model itself but can also contain uncertainties from boundary conditions or material properties which could be reduced by further sampling of data. There is another way of looking at uncertainties by separating model from input data uncertainties. The method chosen in this work for estimating uncertainties for coupled thermal systems neglects the distinction of epistemic and aleatory uncertainties because it would yield a range of ranges which might not be straightforward for interpretation for the thermal engineer. A single range of temperatures is a desirable outcome for the practicing engineer in determining if and what sub-model or coupling client promises the greatest benefit for improvement. Since the equations for a finite difference method of thermal radiation can be easily formulated promising greater insight into the thermal model, direct discrete first order local sensitivity and uncertainty analysis was chosen as a research topic. First order sensitivity has been selected because higher derivatives would be more time consuming. In this way the method behaves like a Taylor approximation and higher order derivatives describe interdependencies between the parameters.

5.2 Previous Research on View Factor Uncertainties

Williams (2010) examined non-equilibrium thermal radiation phenomena as derived from the radiative transfer (RT) equation. In his formulation he uses configuration factors, both between two surfaces, and between a surface and a fluid volume. Because of complex geometries the integral term in the RT may not always yield

simple expression by the variational method. Consequently, he resolved to polynomial chaos expansion in order to solve the integral term numerically.

Sánchez and Mahan (2010) examined distribution factor uncertainty from the Monte Carlo method with purely statistical methods. In that method distribution factors are defined as the ratio of the number of energy bundles absorbed from one face to another and the number of energy bundles N emitted from that face. They can be either gray or represent a band of wavelengths. The idea in their formulation is that tracing a ray in Monte Carlo behaves like a binomial experiment, where success is related to absorbing a ray on the surface, thus relating the distribution factor D_{ij} to a sample proportion. From the definition of confidence interval the following relation for the uncertainty u is derived:

$$|D_{ij}^t - D_{ij}^e| \leq u = W_c \sqrt{\frac{D_{ij}^e(1 - D_{ij}^e)}{N}} \quad (\text{Eq. 5-2})$$

Here, W_c is the critical value of the W-Test and the superscripts distinguish between true t and estimated e distribution factors. They even derived the mean uncertainty bound for all distribution factors for the total number of faces n :

$$u \leq W_c \sqrt{\frac{n-1}{Nn^2}} \quad (\text{Eq. 5-3})$$

One should note that this result is independent of the actual geometry. They demonstrated this method on a surface of up to 150 faces and calculated a necessity of 4 million rays in order to keep the mean uncertainty below one percent. They employed Shapiro-Wilks W-Test tests for normal distribution of samples. Unfortunately, the recommended sample size should not exceed 2000 according to De Muth (2006), which makes it unusable for industrial sized geometries. Alternatively, the chi-square goodness-of-fit test suffers from susceptibility to small deviations from normality.

Shuai et al. (2008) derived the same expressions. They focused on the influence of random number generators on the uncertainties of the distribution factors, which they called R_{ij} . Figure 5-7 graphs the uncertainties between two distribution factors R_{ij} according to Eq. (5-2). For a randomly determined distribution factor the highest uncertainties are expected in the middle range of values. This effect is more pronounced when fewer rays are cast.

They also stated that calculating distribution factors in the Monte Carlo method nowadays is less of a concern related to speed of calculation but more to accuracy because statistical fluctuations can be in the range of the accuracy of a convergence criterion during thermal coupling.

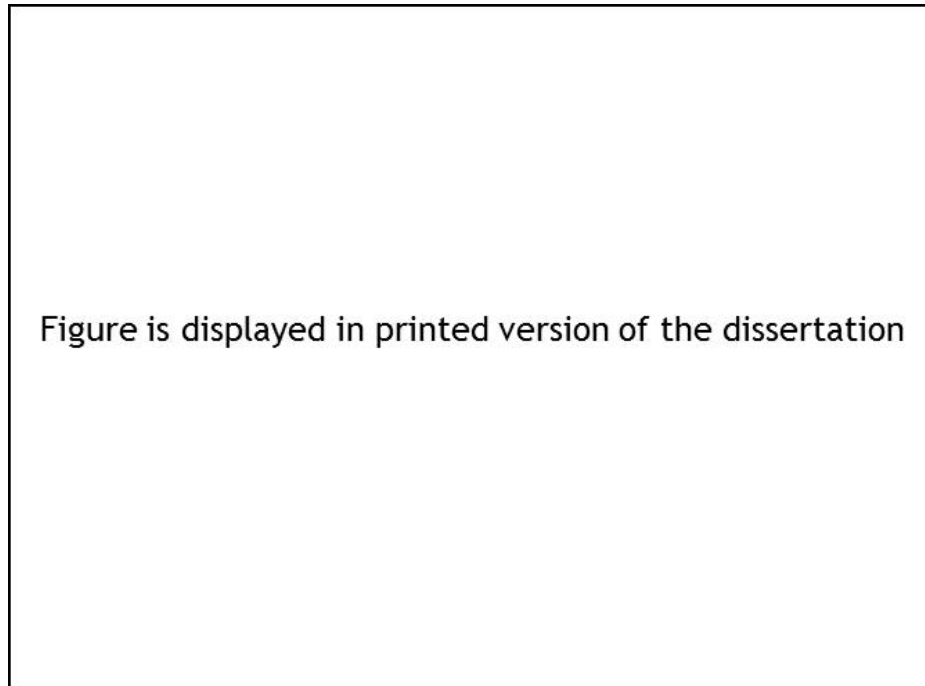


Figure 5-7: Uncertainty \check{S}_{Rij} for distribution factor R_{ij} Reprinted from (Shuai et al., 2008), Copyright © 2007, with permission from Elsevier Inc.

Turning the attention to the surface-to-surface method (S2S) in the author's opinion the first known treatment on view factor uncertainties were done by Taylor et al. (1993). They gave an excellent treatment on the impact of view factors on the outcome of the energy balances. They were able to show by an academic example, that the accuracy of some form factors might influence the whole system, significantly. They developed sensitivity balances for emissivity and temperature for diffuse-gray radiation when a temperature is set as boundary condition. They observed, that by adhering to the reciprocity and closure relation of view factor algebra, sensitivities can be reduced, significantly. They further elaborated on this topic by expanding the sensitivities to changes in area and heat flux boundaries (Taylor et al., 1994; Taylor et al., 1995).

$$\frac{\partial \mathbf{q}_o}{\partial F_{ij}} = \left[\mathbf{I} - (\mathbf{I} - \mathbf{D}_e^M) \mathbf{D}_a^{-1} \mathbf{F}^T \mathbf{D}_a \right]^{-1} \left[(\mathbf{I} - \mathbf{D}_e^M) \mathbf{D}_a^{-1} \frac{\partial \mathbf{F}^T}{\partial F_{ij}} \mathbf{D}_a \mathbf{q}_o \right] \quad (\text{Eq. 5-4})$$

This equation is the derivation of the radiosity \mathbf{q}_o with respect to the view factor F_{ij} . \mathbf{I} is the diagonal identity matrix, \mathbf{F}^T the transpose view factor matrix, \mathbf{D}_a a diagonal matrix for area, and \mathbf{D}_e^M the diagonal matrix for emissivity. The superscript M means that the first M rows are zero.

Taylor and Luck (1995) published a paper that compared several view factor correction methods. They found that the weighted least squares correction for view factors gave the most promising result in producing meaningful configuration factors out of approximate view factors. Korycki (2006) derived local sensitivity factors of the first order in the context of the finite element method (FEM). He derived quite lengthy expressions for conjugate heat transfer including the effect of changing view factors due to shape optimizations as well as a radiation formulation for participating media. He formulated both an adjoint approach as well as the direct method to sensitivity analysis. Bhatia and Livne also (2008) developed sensitivity equations in the context of the finite element method. They employed two sets of meshes. On the coarser mesh, external boundaries were calculated using FEM whereas the finer mesh was used for radiation in a cavity. Both meshes were coupled by a connectivity matrix. Since thermal stresses and deformations were investigated, deformed view factors were approximated by a first order Taylor series expansion using first order sensitivity factors of the view factor in relation to a shape design variable, which showed some descent results. In another paper Bhatia and Livne (2009) also showed a way to put all temperature dependent parameters into the main diagonal of a matrix with consequent Taylor series expansion to get the inverse of a matrix. It should be noted that their biggest mesh size for radiation consisted of merely 3072 elements. Furthermore, they treated transient heat transfer.

5.3 Mathematical Formulation

I am employing a commercial radiation solver based on an element centered finite difference method (FDM) as a starting point of my investigations. Therefore, I proceed by deriving the balances of first order local sensitivity factors for view factors for the element centered finite difference formulation. Siegel and Howell (2002) in their standard work show how to formulate the net-radiation method, which is based upon first principle thermodynamics in non-participating media. More precisely, the Poljak approach is taken and as such this treatment can be regarded as a continuation of Taylor's et al. (1995) work by expanding their approach for combined conduction and convection. The reason for taking Poljak's approach is its simplicity. There are no fractions and the problem is split into two equations which allows for a more simple derivation.

5.3.1 Sensitivity of View Factors

The following treatment was first published in Rauch and Almbauer (2010) as uses scalar notation instead of the matrix notation by Taylor et al. (1995). I start with the relation for a given boundary heat flux b_k as a function of radiosity q_o , view factor F_{ij} , and area A_k :

$$q_{o,k} - \frac{1}{A_k} \sum_{s=1}^N A_s q_{o,s} F_{sk} = b_k \quad (\text{Eq. 5-5})$$

Equation (5-5) shows the relation of the k^{th} face between the boundary flux b_k and radiosity q_{ok} to all other N faces in the enclosure. For more convenience in differentiation, the k^{th} radiosity is taken into the summation where δ_{sk} represents the Kronecker delta:

$$b_k = \sum_{s=1}^N \left[u_{sk} q_{o,s} - u_{sk} \frac{A_s}{A_k} q_{o,s} F_{sk} - (1 - u_{sk}) \frac{A_s}{A_k} q_{o,s} F_{sk} \right] \quad (\text{Eq. 5-6})$$

A total differentiation with respect to the view factor F_{ij} between faces i and j is conducted the following way with running index r :

$$\frac{\partial b_k}{\partial F_{ij}} = \frac{\partial b_k}{\partial A_k} \frac{\partial A_k}{\partial F_{ij}} + \sum_{r=1}^N \frac{\partial b_k}{\partial A_r} \frac{\partial A_r}{\partial F_{ij}} + \sum_{r=1}^N \frac{\partial b_k}{\partial q_{o,r}} \frac{\partial q_{o,r}}{\partial F_{ij}} + \sum_{r=1}^N \frac{\partial b_k}{\partial F_{rk}} \frac{\partial F_{rk}}{\partial F_{ij}} \quad (\text{Eq. 5-7})$$

In this treatment I presume the geometry not to be affected by thermally or load induced displacements. Consequently, the derivative of the heat flux b_k with respect to area amounts to zero. It behooves me now to derive the gradient of the boundary heat flux and radiosity:

$$\frac{\partial b_k}{\partial q_{o,r}} = \sum_{s=1}^N \left[u_{sk} \frac{\partial q_{o,s}}{\partial q_{o,r}} - u_{sk} F_{sk} \frac{\partial q_{o,s}}{\partial q_{o,r}} - (1 - u_{sk}) \frac{A_s}{A_k} F_{sk} \frac{\partial q_{o,s}}{\partial q_{o,r}} \right] \quad (\text{Eq. 5-8})$$

Likewise, the derivation of b_k with F_{sk} :

$$\frac{\partial b_k}{\partial F_{rk}} = \sum_{s=1}^N \left[-u_{sk} q_{o,s} \frac{\partial F_{sk}}{\partial F_{rk}} - (1 - u_{sk}) \frac{A_s}{A_k} q_{o,s} \frac{\partial F_{sk}}{\partial F_{rk}} \right] \quad (\text{Eq. 5-9})$$

Substituting Eq. (5-8) and Eq. (5-9) into Eq. (5-7) and switching from index r to s one receives the following equation by observing that in a partial derivation the gradients are one only when r equals s and zero otherwise:

$$\frac{\partial b_k}{\partial F_{ij}} = \sum_{s=1}^N \left[u_{sk} (1 - F_{sk}) - (1 - u_{sk}) \frac{A_s}{A_k} F_{sk} \right] \frac{\partial q_{o,s}}{\partial F_{ij}} - \sum_{s=1}^N \left[u_{sk} \frac{A_s}{A_k} q_{o,s} + (1 - u_{sk}) \frac{A_s}{A_k} q_{o,s} \right] \frac{\partial F_{sk}}{\partial F_{ij}} \quad (\text{Eq. 5-10})$$

The derivative of the first term of the right hand side in Eq. (5-10) is the unknown to be determined. The gradient of the second term in Eq. (5-10) can be simplified to be 1 if s equals i and j equals k , zero otherwise, if one presumes that each view factor can be changed, independently. It should be noted, that other relations for the derivation of the view factor term could be applied, when one presumes following the summation or the reciprocity rule in view factor algebra. In this work, these relations are not strictly enforced in the thermal radiation solver employed. The interested reader is referred to Taylor et al. (1995) for a treatment of closure and reciprocity in the uncertainty relation.

$$\frac{\partial b_k}{\partial F_{ij}} = \sum_{s=1}^N \left[u_{ks} (1 - F_{kk}) - (1 - u_{ks}) \frac{A_s}{A_k} F_{sk} \right] \frac{\partial q_{o,s}}{\partial F_{ij}} - u_{si} u_{kj} \frac{A_i}{A_j} q_{o,i} \quad (\text{Eq. 5-11})$$

So far, the author has followed the papers of Taylor et al. (1994, 1995). They did not make a distinction between different heat transfer modes. In the present treatment the author wishes to distinguish those modes in order to be able to observe the propagation of uncertainties for each respective property representing a transfer mode. Therefore, the boundary heat flux is written as:

$$b_k = q_{imp} + h_k(T_f - T_k) + \frac{1}{A_k} \sum_{t=1}^{N_{Cond}} \left(-\frac{k_{kt} A_{kt}}{l_{kt}} (T_k - T_t) \right) \quad (\text{Eq. 5-12})$$

T_f represents the fluid temperature, h_k the convective heat transfer coefficient, k_{kt} the thermal conductivity, which in this study is presumed to be independent of temperature, A_{kt} the area bordering a neighboring thermal element, l_{kt} the distance between two thermal node centers, q_{imp} the imposed heat, which is treated as a constant with respect to a view factor in this work, and N_{Cond} the number of thermally conducting neighbors. Figure 5-8 depicts a thermal node with corresponding heat fluxes and area definitions. For clarification, the radiative flux is defined positive when leaving the system, as opposed to the convective and conductive fluxes. That is why Eq. (5-5) is written for radiation and Eq. (5-12) for conduction and convection, respectively. As demonstrated in Eq. (5-7) a partial differentiation with respect to the view factor is applied to Eq. (5-12).

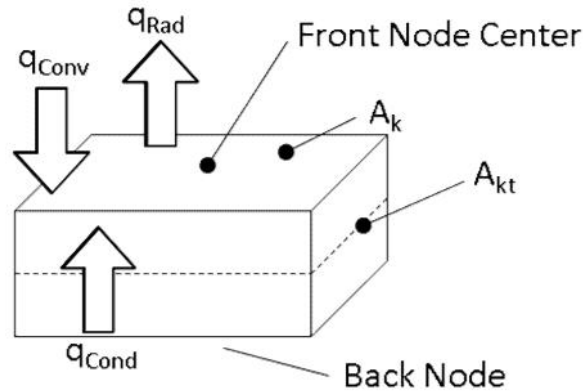


Figure 5-8: Thermal node with heat fluxes.

$$\frac{\partial b_k}{\partial F_{ij}} = \frac{\partial b_k}{\partial T_k} \frac{\partial T_k}{\partial F_{ij}} + \sum_{r=1}^{N_{Cond}} \frac{\partial b_k}{\partial T_r} \frac{\partial T_r}{\partial F_{ij}} \quad (\text{Eq. 5-13})$$

The partial derivative of the order one with respect to the node temperature is:

$$\frac{\partial b_k}{\partial T_k} = -h_k - \frac{1}{A_k} \sum_{t=1}^{N_{Cond}} \frac{k_{kt}}{l_{kt}} A_{kt} \quad (\text{Eq. 5-14})$$

The partial derivative with the neighboring node temperature is:

$$\frac{\partial b_k}{\partial T_r} = \frac{1}{A_k} \sum_{t=1}^{N_{Cond}} \frac{k_{kt}}{l_{kt}} A_{kt} \frac{\partial T_t}{\partial T_r} \quad (\text{Eq. 5-15})$$

Substituting Eqs. (5-14) and (5-15) into Eq. (5-13) one gets:

$$\frac{\partial b_k}{\partial F_{ij}} = \left(-h_k - \frac{1}{A_k} \sum_{t=1}^{N_{Cond}} \frac{k_{kt}}{l_{kt}} A_{kt} \right) \frac{\partial T_k}{\partial F_{ij}} + \frac{1}{A_k} \sum_{t=1}^{N_{Cond}} \left[\frac{k_{kt}}{l_{kt}} A_{kt} \right] \frac{\partial T_t}{\partial F_{ij}} \quad (\text{Eq. 5-16})$$

Now, one can substitute Eq. (5-16) into Eq. (5-11).

$$\begin{aligned} & \sum_{s=1}^N \left[u_{ks} (1 - F_{kk}) - (1 - u_{ks}) \frac{A_s}{A_k} F_{sk} \right] \frac{\partial q_{o,s}}{\partial F_{ij}} - u_{si} u_{kj} \frac{A_i}{A_j} q_{o,i} \\ & = \left(-h_k - \frac{1}{A_k} \sum_{t=1}^{N_{Cond}} \frac{k_{kt}}{l_{kt}} A_{kt} \right) \frac{\partial T_k}{\partial F_{ij}} + \frac{1}{A_k} \sum_{t=1}^{N_{Cond}} \left[\frac{k_{kt}}{l_{kt}} A_{kt} \right] \frac{\partial T_t}{\partial F_{ij}} \end{aligned} \quad (\text{Eq. 5-17})$$

Since I now have two unknown gradients of radiosity and nodal temperature with respect to the form factor, I need a second relation. Poljaks approach provides for a relation between radiosity and temperature:

$$q_{o,k} - (1 - v_k) \frac{1}{A_k} \sum_{s=1}^N A_s q_{o,s} F_{sk} = b_k \quad (\text{Eq. 5-18})$$

In this relation the emissivity ε is introduced, otherwise the left hand side is quite similar to Eq. (5-5). The derivation of this relation with respect to the view factor follows the same pattern. First, the first term is drawn into the summation term:

$$b_k = \sum_{s=1}^N \left[u_{sk} q_{o,s} - u_{sk} (1 - v_k) q_{o,s} F_{sk} - (1 - u_{sk}) (1 - v_k) \frac{A_s}{A_k} q_{o,s} F_{sk} \right] \quad (\text{Eq. 5-19})$$

Then, partial differentiation is applied:

$$\frac{\partial b_k}{\partial F_{ij}} = \sum_{r=1}^N \frac{\partial b_k}{\partial A_r} \frac{\partial A_r}{\partial F_{ij}} + \frac{\partial b_k}{\partial v_k} \frac{\partial v_k}{\partial F_{ij}} + \sum_{r=1}^N \frac{\partial b_k}{\partial q_{o,r}} \frac{\partial q_{o,r}}{\partial F_{ij}} + \sum_{r=1}^N \frac{\partial b_k}{\partial F_{rk}} \frac{\partial F_{rk}}{\partial F_{ij}} \quad (\text{Eq. 5-20})$$

The same considerations as for Eq. (5-7) apply with the addition that the emissivity is a material property and thus stands in no relation to the view factor. The derivations of the boundary heat flux with respect to radiosity and form factor are:

$$\frac{\partial b_k}{\partial q_{o,s}} = \sum_{s=1}^N \left[u_{sk} \frac{\partial q_{o,s}}{\partial q_{o,r}} - u_{sk} (1 - v_k) F_{sk} \frac{\partial q_{o,s}}{\partial q_{o,r}} - (1 - u_{sk}) (1 - v_k) \frac{A_s}{A_k} F_{sk} \frac{\partial q_{o,s}}{\partial q_{o,r}} \right] \quad (\text{Eq. 5-21})$$

$$\frac{\partial b_k}{\partial F_{sk}} = \sum_{s=1}^N \left[-u_{sk} (1 - v_k) q_{o,s} \frac{\partial F_{sk}}{\partial F_{rk}} - (1 - u_{sk}) (1 - v_k) \frac{A_s}{A_k} q_{o,s} \frac{\partial F_{sk}}{\partial F_{rk}} \right] \quad (\text{Eq. 5-22})$$

These relations are substituted into Eq. (5-20).

$$\begin{aligned} \frac{\partial b_k}{\partial F_{ij}} = & \sum_{s=1}^N \left[u_{sk} - u_{sk}(1-v_k)F_{sk} - (1-u_{sk})(1-v_k)\frac{A_s}{A_k}F_{sk} \right] \frac{\partial q_{o,s}}{\partial F_{ij}} \\ & - \sum_{s=1}^N \left[u_{sk}(1-v_k)q_{os} + (1-u_{sk})(1-v_k)\frac{A_s}{A_k}q_{os} \right] \frac{\partial F_{sk}}{\partial F_{ij}} \end{aligned} \quad (\text{Eq. 5-23})$$

Equation (5-23) can be simplified at the second term of the right hand side in the same way as in Eq. (5-11).

$$\frac{\partial b_k}{\partial F_{ij}} = \sum_{s=1}^N \left[u_{sk} - u_{sk}(1-v_k)F_{sk} - (1-u_{sk})(1-v_k)\frac{A_s}{A_k}F_{sk} \right] \frac{\partial q_{o,s}}{\partial F_{ij}} - u_{si}u_{kj}(1-v_j)\frac{A_i}{A_j}q_{o,i} \quad (\text{Eq. 5-24})$$

It is now time to introduce the temperature T:

$$b_k = v_k \dagger T_k^4 \quad (\text{Eq. 5-25})$$

In this work the emissivity is kept to be independent of temperature. Again, partial differentiation is applied and yields:

$$\frac{\partial b_k}{\partial F_{ij}} = \frac{\partial b_k}{\partial T_k} \frac{\partial T_k}{\partial F_{ij}} + \frac{\partial b_k}{\partial v_k} \frac{\partial v_k}{\partial F_{ij}} \quad (\text{Eq. 5-26})$$

$$\frac{\partial b_k}{\partial T_k} = 4v_k \dagger T_k^3 \quad (\text{Eq. 5-27})$$

$$\frac{\partial b_k}{\partial F_{ij}} = 4v_k \dagger T_k^3 \frac{\partial T_k}{\partial F_{ij}} \quad (\text{Eq. 5-28})$$

Equation (5-28) is set equal with Eq. (5-24):

$$\begin{aligned} 4v_k \dagger T_k^3 \frac{\partial T_k}{\partial F_{ij}} = & \sum_{s=1}^N \left[u_{sk} - u_{sk}(1-v_k)F_{sk} - (1-u_{sk})(1-v_k)\frac{A_s}{A_k}F_{sk} \right] \frac{\partial q_{o,s}}{\partial F_{ij}} \\ & - u_{si}u_{kj}(1-v_j)\frac{A_i}{A_j}q_{o,i} \end{aligned} \quad (\text{Eq. 5-29})$$

Equation (5-29) provides a relation for the temperature gradient:

$$\begin{aligned} \frac{\partial T_k}{\partial F_{ij}} = & \frac{1}{4v_k \dagger T_k^3} \left[\sum_{s=1}^N \left[u_{sk} - u_{sk}(1-v_k)F_{sk} - (1-u_{sk})(1-v_k)\frac{A_s}{A_k}F_{sk} \right] \frac{\partial q_{o,s}}{\partial F_{ij}} \right. \\ & \left. - u_{si}u_{kj}(1-v_j)\frac{A_i}{A_j}q_{o,i} \right] \end{aligned} \quad (\text{Eq. 5-30})$$

The same relation as above is used to express the temperature gradients for the neighboring faces:

$$\frac{\partial T_t}{\partial F_{ij}} = \frac{1}{4v_t \uparrow T_t^3} \left[\sum_{s=1}^N \left[u_{st} - u_{st}(1-v_t)F_{st} - (1-u_{st})(1-v_t) \frac{A_s}{A_t} F_{st} \right] \frac{\partial q_{o,s}}{\partial F_{ij}} \right. \\ \left. - u_{si} u_{ij} (1-v_j) \frac{A_i}{A_j} q_{o,i} \right] \quad (\text{Eq. 5-31})$$

Equations (5-30) and (5-31) are now substituted into Eq. (5-17):

$$\sum_{s=1}^N \left[u_{sk} (1-F_{sk}) - (1-u_{sk}) \frac{A_s}{A_k} F_{sk} \right] \frac{\partial q_{o,s}}{\partial F_{ij}} = u_{si} u_{kj} \frac{A_i}{A_j} q_{o,i} \\ + \frac{1}{4v_k \uparrow T_k^3} \left[\sum_{s=1}^N \left[u_{sk} - u_{sk}(1-v_k)F_{sk} - (1-u_{sk})(1-v_k) \frac{A_s}{A_k} F_{sk} \right] \frac{\partial q_{o,s}}{\partial F_{ij}} \right. \\ \left. - u_{si} u_{kj} (1-v_j) \frac{A_i}{A_j} q_{o,i} \right] \left(-h_k - \frac{1}{A_k} \sum_{t=1}^{N_{\text{Cond}}} \frac{k_{kt}}{l_{kt}} A_{kt} \right) \\ + \frac{1}{A_k} \sum_{t=1}^{N_{\text{Cond}}} \left[\frac{k_{kt}}{l_{kt}} A_{kt} \frac{1}{4v_t \uparrow T_t^3} \left[\sum_{s=1}^N \left[u_{st} - u_{st}(1-v_t)F_{st} - (1-u_{st})(1-v_t) \frac{A_s}{A_t} F_{st} \right] \frac{\partial q_{o,s}}{\partial F_{ij}} \right. \right. \\ \left. \left. - u_{si} u_{ij} (1-v_j) \frac{A_i}{A_j} q_{o,i} \right] \right] \quad (\text{Eq. 5-32})$$

Separating the terms containing an unknown I obtain the final relation for calculating the derivative with respect to radiosity:

$$\sum_{s=1}^N \left[u_{sk} (1-F_{sk}) - (1-u_{sk}) \frac{A_s}{A_k} F_{sk} \right] \frac{\partial q_{o,s}}{\partial F_{ij}} \\ - \frac{1}{4v_k \uparrow T_k^3} \left[\sum_{s=1}^N \left[u_{sk} - u_{sk}(1-v_k) \frac{A_s}{A_k} F_{sk} - (1-u_{sk})(1-v_k) \frac{A_s}{A_k} F_{sk} \right] \frac{\partial q_{o,s}}{\partial F_{ij}} \right] \left(-h_k - \frac{1}{A_k} \sum_{t=1}^{N_{\text{Cond}}} \frac{k_{kt}}{l_{kt}} A_{kt} \right) \\ - \frac{1}{A_k} \sum_{t=1}^{N_{\text{Cond}}} \left[\frac{k_{kt}}{l_{kt}} A_{kt} \frac{1}{4v_t \uparrow T_t^3} \left[\sum_{s=1}^N \left[u_{st} - u_{st}(1-v_t) \frac{A_s}{A_t} F_{st} - (1-u_{st})(1-v_t) \frac{A_s}{A_t} F_{st} \right] \frac{\partial q_{o,s}}{\partial F_{ij}} \right] \right] \\ = u_{si} u_{kj} \frac{A_i}{A_j} q_{o,i} \\ - u_{si} u_{kj} (1-v_j) \frac{A_i}{A_j} q_{o,i} \left(-h_k - \frac{1}{A_k} \sum_{t=1}^{N_{\text{Cond}}} \frac{k_{kt}}{l_{kt}} A_{kt} \right) \frac{1}{4v_k \uparrow T_k^3} \\ - u_{si} u_{ij} \frac{1}{A_k} \frac{k_{kj}}{l_{kj}} A_{kj} \frac{1}{4v_j \uparrow T_j^3} (1-v_j) \frac{A_i}{A_j} q_{o,i} \quad (\text{Eq. 5-33})$$

Once the radiosity derivative has been calculated by Eq. (5-33), one can simply multiply the result vector by Eq. (5-29).

The first term on the left-hand-side (LHS) of Eq. (5-33) is the radiative term as published by Taylor et al. (1995). The second term is a mixed convective and conductive term and the last term of the LHS is a conductive term. The same holds for the right-hand-side (RHS). One should note the summations in the terms. Equation (5-33) can only be solved for all elements - more precisely thermal nodes in the finite difference formulation - simultaneously. In other words one has a dense solution matrix. On the RHS there will be only one: When the index j of the view factor coincides with the thermal node number. Including conduction, terms with neighbors of a thermal node with index t are added.

The aforementioned derivations presumed that the temperature of node k was not fixed. If it is fixed, Eq. (5-29) can be taken. Since the derivative of node temperature with respect to the view factor will be zero in that particular case one can calculate the change of radiosities with respect to the view factor by the following equation:

$$\sum_{s=1}^N \left[u_{sk} - u_{sk}(1-v_k)F_{sk} - (1-u_{sk})(1-v_k)\frac{A_s}{A_k}F_{sk} \right] \frac{\partial q_{o,s}}{\partial F_{ij}} = u_{si}u_{kj}(1-v_j)\frac{A_i}{A_j}q_{o,i} \quad (\text{Eq. 5-34})$$

With the radiosity derivative with respect to view factor known, Eq. (5-11) can be used to calculate the change in net heat flux on that node.

5.3.2 Sensitivity of Emissivity

The following treatment was published in Rauch and Almbauer (2010a).

We start again from Eq. (5-6) which shall be rewritten as:

$$b_k = \sum_{s=1}^N \left[u_{sk}q_{o,s} - u_{sk}q_{o,s}F_{sk} - (1-u_{sk})\frac{A_s}{A_k}q_{o,s}F_{sk} \right] \quad (\text{Eq. 5-35})$$

Now, the partial derivatives of the heat flux with respect to emissivity have to be calculated:

$$\frac{\partial b_k}{\partial v_i} = \sum_{r=1}^N \frac{\partial b_k}{\partial A_r} \frac{\partial A_r}{\partial v_i} + \sum_{r=1}^N \frac{\partial b_k}{\partial q_{o,r}} \frac{\partial q_{o,r}}{\partial v_i} + \sum_{r=1}^N \frac{\partial b_k}{\partial F_{rk}} \frac{\partial F_{rk}}{\partial v_i} \quad (\text{Eq. 5-36})$$

The partial derivatives for the area and the view factor with respect to the emissivity can be ignored, as we do not consider changes in geometry due to thermal stresses. The radiosity will usually change with changing parameter and is duplicated from Eq. (5-8).

$$\frac{\partial b_k}{\partial q_{o,r}} = \sum_{s=1}^N \left[u_{ks} (1 - F_{kk}) \frac{\partial q_{o,s}}{\partial q_{o,r}} - (1 - u_{sk}) \frac{A_s}{A_k} F_{sk} \frac{\partial q_{o,s}}{\partial q_{o,r}} \right] \quad (\text{Eq. 5-37})$$

Substituting eq. (5-37) into eq. (5-36) with all the aforementioned simplifications yields:

$$\frac{\partial b_k}{\partial v_i} = \sum_{s=1}^N \left[u_{ks} (1 - F_{kk}) - (1 - u_{ks}) \frac{A_s}{A_k} F_{sk} \right] \frac{\partial q_{o,s}}{\partial v_i} \quad (\text{Eq. 5-38})$$

Equation (5-12) is rewritten as:

$$b_k = q_{imp} + h_k (T_f - T_k) + \frac{1}{A_k} \sum_{t=1}^{N_{Cond}} \left(-\frac{k_{kt} A_{kt}}{l_{kt}} (T_k - T_t) \right) \quad (\text{Eq. 5-39})$$

A partial differentiation with respect to emissivity is conducted:

$$\frac{\partial b_k}{\partial v_i} = \frac{\partial b_k}{\partial T_k} \frac{\partial T_k}{\partial v_i} + \sum_{r=1}^{N_{Cond}} \frac{\partial b_k}{\partial T_r} \frac{\partial T_r}{\partial v_i} \quad (\text{Eq. 5-40})$$

The partial derivative of the order one with respect to the node temperature is:

$$\frac{\partial b_k}{\partial T_k} = -h_k - \frac{1}{A_k} \sum_{t=1}^{N_{Cond}} \frac{k_{kt}}{l_{kt}} A_{kt} \quad (\text{Eq. 5-41})$$

The partial derivative with the neighboring node temperature is:

$$\frac{\partial b_k}{\partial T_r} = \frac{1}{A_k} \sum_{t=1}^{N_{Cond}} \frac{k_{kt}}{l_{kt}} A_{kt} \frac{\partial T_t}{\partial T_r} \quad (\text{Eq. 5-42})$$

Placing those last two equations into Eq. (5-40) we get:

$$\frac{\partial b_k}{\partial v_i} = \left(-h_k - \frac{1}{A_k} \sum_{t=1}^{N_{Cond}} \frac{k_{kt}}{l_{kt}} A_{kt} \right) \frac{\partial T_k}{\partial v_i} + \frac{1}{A_k} \sum_{t=1}^{N_{Cond}} \frac{k_{kt}}{l_{kt}} A_{kt} \frac{\partial T_t}{\partial v_i} \quad (\text{Eq. 5-43})$$

Equation (5-43) can now be substituted into Eq. (5-38):

$$\sum_{s=1}^N \left[u_{ks} (1 - F_{kk}) - (1 - u_{ks}) \frac{A_s}{A_k} F_{sk} \right] \frac{\partial q_{o,s}}{\partial v_i} = \left(-h_k - \frac{1}{A_k} \sum_{t=1}^{N_{Cond}} \frac{k_{kt}}{l_{kt}} A_{kt} \right) \frac{\partial T_k}{\partial v_i} + \frac{1}{A_k} \sum_{t=1}^{N_{Cond}} \frac{k_{kt}}{l_{kt}} A_{kt} \frac{\partial T_t}{\partial v_i} \quad (\text{Eq. 5-44})$$

Taylor et al. (1995) in their work were able to calculate the radiosity derivative, because there were no terms containing temperature. In Eq. (5-44) there are the partial derivative of temperature and radiosity as unknowns. Therefore, we need a second equation, relating temperature to radiosity which we already showed in Eq. (5-19).

$$b_k = \sum_{s=1}^N \left[u_{sk} q_{o,s} - u_{sk} (1 - v_k) q_{o,s} F_{sk} - (1 - u_{sk}) (1 - v_k) \frac{A_s}{A_k} q_{o,s} F_{sk} \right] \quad (\text{Eq. 5-45})$$

The total derivative of this equation is:

$$\frac{\partial b_k}{\partial v_i} = \sum_{r=1}^N \frac{\partial b_k}{\partial q_{o,r}} \frac{\partial q_{o,r}}{\partial v_i} + \frac{\partial b_k}{\partial v_k} \frac{\partial v_k}{\partial v_i} \quad (\text{Eq. 5-46})$$

The partial derivatives are:

$$\frac{\partial b_k}{\partial q_{o,r}} = \sum_{s=1}^N \left[u_{sk} - u_{sk} (1 - v_k) \frac{A_s}{A_k} F_{sk} - (1 - u_{sk}) (1 - v_k) \frac{A_s}{A_k} F_{sk} \frac{\partial q_{o,s}}{\partial q_{o,r}} \right] \quad (\text{Eq. 5-47})$$

$$\frac{\partial b_k}{\partial v_k} = \frac{1}{A_k} \sum_{s=1}^N \left[u_{sk} A_s q_{o,s} F_{sk} + (1 - u_{sk}) A_s q_{o,s} F_{sk} \right] \quad (\text{Eq. 5-48})$$

The last derivation can be simplified to:

$$\frac{\partial b_k}{\partial v_k} = \frac{1}{A_k} \sum_{s=1}^N A_s q_{o,s} F_{sk} \quad (\text{Eq. 5-49})$$

Equations (5-49) and (5-47) are substituted into Eq. (5-46):

$$\frac{\partial b_k}{\partial v_i} = \sum_{s=1}^N \left[u_{ks} (1 - (1 - v_k) F_{kk}) - (1 - u_{ks}) (1 - v_k) \frac{A_s}{A_k} F_{sk} \right] \frac{\partial q_{o,s}}{\partial v_i} + \frac{u_{ki}}{A_i} \sum_{s=1}^N A_s q_{o,s} F_{si} \quad (\text{Eq. 5-50})$$

The other side of Eq. (5-45) is:

$$b_k = v_k \dagger T_k^4 \quad (\text{Eq. 5-51})$$

The total derivation with respect to emissivity yields:

$$\frac{\partial b_k}{\partial v_i} = \frac{\partial b_k}{\partial T_k} \frac{\partial T_k}{\partial v_i} + \frac{\partial b_k}{\partial v_k} \frac{\partial v_k}{\partial v_i} \quad (\text{Eq. 5-52})$$

$$\frac{\partial b_k}{\partial v_k} = \dagger T_k^4 \quad (\text{Eq. 5-53})$$

$$\frac{\partial b_k}{\partial T_k} = 4v_k \dagger T_k^3 \quad (\text{Eq. 5-54})$$

Putting Eq. (5-53) and Eq. (5-54) into Eq. (5-52) one gets:

$$\frac{\partial b_k}{\partial v_i} = 4v_k \dagger T_k^3 \frac{\partial T_k}{\partial v_i} + \dagger T_k^4 \frac{\partial v_k}{\partial v_i} = 4v_k \dagger T_k^3 \frac{\partial T_k}{\partial v_i} + u_{ik} \dagger T_i^4 \quad (\text{Eq. 5-55})$$

Substituting this equation into Eq. (5-50) we have the following relation:

$$\sum_{s=1}^N \left[u_{ks} (1 - (1 - v_k) F_{sk}) - (1 - u_{ks}) (1 - v_k) \frac{A_s}{A_k} F_{sk} \right] \frac{\partial q_{o,s}}{\partial v_i} + \frac{u_{ki}}{A_i} \sum_{s=1}^N A_s q_{o,s} F_{si} = 4v_k \dagger T_k^3 \frac{\partial T_k}{\partial v_i} + u_{ik} \dagger T_i^4 \quad (\text{Eq. 5-56})$$

This is our second relation for the unknown derivatives T and radiosity in emissivity.

Eq. (5-56) is rewritten to explicitly calculate the temperature derivatives:

$$\frac{\partial T_k}{\partial v_i} = \left[\sum_{s=1}^N \left[u_{ks} (1 - (1 - v_k) F_{sk}) - (1 - u_{ks}) (1 - v_k) \frac{A_s}{A_k} F_{sk} \right] \frac{\partial q_{o,s}}{\partial v_i} + \frac{u_{ki}}{A_i} \sum_{s=1}^N A_s q_{o,s} F_{si} - u_{ik} \dagger T_i^4 \right] \frac{1}{4v_k \dagger T_k^3} \quad (\text{Eq. 5-57})$$

When we replace the index k with t we have:

$$\frac{\partial T_t}{\partial v_i} = \left[\sum_{s=1}^N \left[u_{ts} (1 - (1 - v_t) F_{ts}) - (1 - u_{ts}) (1 - v_t) \frac{A_s}{A_t} F_{st} \right] \frac{\partial q_{o,s}}{\partial v_i} + \frac{u_{ti}}{A_t} \sum_{s=1}^N A_s q_{o,s} F_{si} - u_{it} \dagger T_i^4 \right] \frac{1}{4v_t \dagger T_t^3} \quad (\text{Eq. 5-58})$$

In order to obtain the final equation the last two equations are put into Eq. (5-44):

$$\begin{aligned}
& \sum_{s=1}^N \left[u_{ks} (1 - F_{sk}) - (1 - u_{ks}) \frac{A_s}{A_k} F_{sk} \right] \frac{\partial q_{o,s}}{\partial v_i} = \left(-h_k - \frac{1}{A_k} \sum_{t=1}^{N_{Cond}} \frac{k_{kt}}{l_{kt}} A_{kt} \right) \\
& * \frac{1}{4v_k \uparrow T_k^3} \left(\sum_{s=1}^N \left[u_{ks} (1 - (1 - v_k) F_{sk}) - (1 - u_{ks}) (1 - v_k) \frac{A_s}{A_k} F_{sk} \right] \frac{\partial q_{o,s}}{\partial v_i} + \frac{u_{ki}}{A_i} \sum_{s=1}^N A_s q_{o,s} F_{si} - u_{ik} \uparrow T_i^4 \right) \\
& \quad + \frac{1}{A_k} \sum_{t=1}^{N_{Cond}} \frac{k_{kt}}{l_{kt}} A_{kt} \\
& * \frac{1}{4v_t \uparrow T_t^3} \left(\sum_{s=1}^N \left[u_{ts} (1 - (1 - v_t) F_{st}) - (1 - u_{ts}) (1 - v_t) \frac{A_s}{A_t} F_{st} \right] \frac{\partial q_{o,s}}{\partial v_i} + \frac{u_{ti}}{A_i} \sum_{s=1}^N A_s q_{o,s} F_{si} - u_{it} \uparrow T_i^4 \right)
\end{aligned} \tag{Eq. 5-59}$$

Separating LHS terms from RHS terms one gets the equations as it is implemented:

$$\begin{aligned}
& \sum_{s=1}^N \left[u_{ks} (1 - F_{sk}) - (1 - u_{ks}) \frac{A_s}{A_k} F_{sk} \right] \frac{\partial q_{o,s}}{\partial v_i} - \left(-h_k - \frac{1}{A_k} \sum_{t=1}^{N_{Cond}} \frac{k_{kt}}{l_{kt}} A_{kt} \right) \frac{1}{4v_k \uparrow T_k^3} \\
& * \sum_{s=1}^N \left[u_{ks} (1 - (1 - v_k) F_{sk}) - (1 - u_{ks}) (1 - v_k) \frac{A_s}{A_k} F_{sk} \right] \frac{\partial q_{o,s}}{\partial v_i} \\
& - \frac{1}{A_k} \sum_{t=1}^{N_{Cond}} \frac{k_{kt}}{l_{kt}} A_{kt} \frac{1}{4v_t \uparrow T_t^3} \sum_{s=1}^N \left[u_{ts} (1 - (1 - v_t) F_{st}) - (1 - u_{ts}) (1 - v_t) \frac{A_s}{A_t} F_{st} \right] \frac{\partial q_{o,s}}{\partial v_i} \\
& = u_{ki} \left(-h_i - \frac{1}{A_i} \sum_{t=1}^{N_{Cond}} \frac{k_{it}}{l_{it}} A_{it} \right) \frac{1}{4v_i \uparrow T_i^3} \left(\frac{1}{A_i} \sum_{s=1}^N A_s q_{o,s} F_{si} - u_{ik} \uparrow T_i^4 \right) \\
& \quad + u_{ti} \frac{1}{A_k} \frac{k_{ki}}{l_{ki}} A_{ki} \frac{1}{4v_i \uparrow T_i^3} \left(\frac{1}{A_i} \sum_{s=1}^N A_s q_{o,s} F_{si} - \uparrow T_i^4 \right)
\end{aligned} \tag{Eq. 5-60}$$

Once the radiosity derivative has been calculated by Eq. (5-60), one can simply multiply the result vector by Eq. (5-57).

To the reader is pointed out that there is no sole radiative term on the RHS. This means, that in the absence of conduction and convection the radiosity gradient will be zero. In that case Eq. (5-57) is simplified. It then states that a change of temperature by emissivity is proportional to the difference of radiosity and node temperature. In an IR camera radiosity is measured and interpreted as temperature by assuming an emissivity. Changing that assumed emissivity lets one find the temperature iteratively.

If the node temperature is fixed, Eq. (5-57) can be taken. Since the derivative of node temperature with respect to emissivity will be zero in that particular case we can calculate the change of radiosities with respect to emissivity by the following equation:

$$\sum_{s=1}^N \left[u_{ks} (1 - (1 - v_k) F_{sk}) - (1 - u_{ks}) (1 - v_k) \frac{A_s}{A_k} F_{sk} \right] \frac{\partial q_{o,s}}{\partial v_i} = - \frac{u_{ki}}{A_i} \sum_{s=1}^N A_s q_{o,s} F_{si} + u_{ik} \uparrow T_i^4 \quad (\text{Eq. 5-61})$$

With the radiosity derivative with respect to emissivity is known, Eq. (5-38) can be used to calculate the change in net heat flux on that node.

5.3.3 Sensitivity of Fluid Temperature

I start again from Eq. (5-6) which shall be rewritten as:

$$b_k = \sum_{s=1}^N \left[u_{sk} q_{o,s} - u_{sk} q_{o,s} F_{sk} - (1 - u_{sk}) \frac{A_s}{A_k} q_{o,s} F_{sk} \right] \quad (\text{Eq. 5-62})$$

The partial derivatives of the heat flux with respect to the fluid temperature T_f have to be calculated:

$$\frac{\partial b_k}{\partial T_{f,i}} = \sum_{r=1}^N \frac{\partial b_k}{\partial q_{o,r}} \frac{\partial q_{o,r}}{\partial T_{f,i}} \quad (\text{Eq. 5-63})$$

$$\frac{\partial b_k}{\partial q_{o,r}} = \sum_{s=1}^N \left[u_{ks} (1 - F_{kk}) \frac{\partial q_{o,s}}{\partial q_{o,r}} - (1 - u_{ks}) \frac{A_s}{A_k} F_{sk} \frac{\partial q_{o,s}}{\partial q_{o,r}} \right] \quad (\text{Eq. 5-64})$$

$$\frac{\partial b_k}{\partial T_{f,i}} = \sum_{s=1}^N \left[u_{ks} (1 - F_{sk}) - (1 - u_{ks}) \frac{A_s}{A_k} F_{sk} \right] \frac{\partial q_{o,s}}{\partial T_{f,i}} \quad (\text{Eq. 5-65})$$

This is a particular simple derivative so far.

Equation (5-12) is rewritten as:

$$b_k = q_{imp} + h_k (T_f - T_k) + \frac{1}{A_k} \sum_{t=1}^{N_{Cond}} \left(- \frac{k_{kt} A_{kt}}{l_{kt}} (T_k - T_t) \right) \quad (\text{Eq. 5-66})$$

Again, total derivation is applied to that equation:

$$\frac{\partial b_k}{\partial T_{f,i}} = \frac{\partial b_k}{\partial T_k} \frac{\partial T_k}{\partial T_{f,i}} + \sum_{r=1}^{N_{Cond}} \frac{\partial b_k}{\partial T_r} \frac{\partial T_r}{\partial T_{f,i}} + \frac{\partial b_k}{\partial T_{f,k}} \frac{\partial T_{f,k}}{\partial T_{f,i}} \quad (\text{Eq. 5-67})$$

$$\frac{\partial b_k}{\partial T_k} = -h_k - \frac{1}{A_k} \sum_{t=1}^{N_{Cond}} \frac{k_{kt}}{l_{kt}} A_{kt} \quad (\text{Eq. 5-68})$$

$$\frac{\partial b_k}{\partial T_r} = \frac{1}{A_k} \sum_{t=1}^{N_{Cond}} \frac{k_{kt}}{l_{kt}} A_{kt} \frac{\partial T_t}{\partial T_r} \quad (\text{Eq. 5-69})$$

$$\frac{\partial b_k}{\partial T_{f,i}} = h_k \quad (\text{Eq. 5-70})$$

$$\frac{\partial b_k}{\partial T_{f,i}} = \left(-h_k - \frac{1}{A_k} \sum_{t=1}^{N_{Cond}} \frac{k_{kt}}{l_{kt}} A_{kt} \right) \frac{\partial T_k}{\partial T_{f,i}} + \frac{1}{A_k} \sum_{t=1}^{N_{Cond}} \frac{k_{kt}}{l_{kt}} A_{kt} \frac{\partial T_t}{\partial T_{f,i}} + u_{ki} h_i \quad (\text{Eq. 5-71})$$

When equaling this equation with Eq. (5-65) I get the following:

$$\begin{aligned} \sum_{s=1}^N \left[u_{ks} (1 - F_{sk}) - (1 - u_{ks}) \frac{A_s}{A_k} F_{sk} \right] \frac{\partial q_{o,s}}{\partial T_{f,i}} &= \left(-h_k - \frac{1}{A_k} \sum_{t=1}^{N_{Cond}} \frac{k_{kt}}{l_{kt}} A_{kt} \right) \frac{\partial T_k}{\partial T_{f,i}} + \\ &+ \frac{1}{A_k} \sum_{t=1}^{N_{Cond}} \frac{k_{kt}}{l_{kt}} A_{kt} \frac{\partial T_t}{\partial T_{f,i}} + u_{ki} h_i \end{aligned} \quad (\text{Eq. 5-72})$$

Now, I need the second relation of Poljak's approach:

$$b_k = \sum_{s=1}^N \left[u_{sk} q_{o,s} - u_{sk} (1 - v_k) q_{o,s} F_{sk} - (1 - u_{sk}) (1 - v_k) \frac{A_s}{A_k} q_{o,s} F_{sk} \right] \quad (\text{Eq. 5-73})$$

The total derivative with respect to the fluid temperature is:

$$\frac{\partial b_k}{\partial T_{f,i}} = \sum_{r=1}^N \frac{\partial b_k}{\partial q_{o,r}} \frac{\partial q_{o,r}}{\partial T_{f,i}} \quad (\text{Eq. 5-74})$$

The corresponding partial derivative is:

$$\frac{\partial b_k}{\partial q_{o,r}} = \sum_{s=1}^N \left[u_{sk} \left(1 - (1 - v_k) \frac{A_s}{A_k} F_{sk} \right) \frac{\partial q_{o,s}}{\partial q_{o,r}} - (1 - u_{sk}) (1 - v_k) \frac{A_s}{A_k} F_{sk} \frac{\partial q_{o,s}}{\partial q_{o,r}} \right] \quad (\text{Eq. 5-75})$$

$$\frac{\partial b_k}{\partial T_{f,i}} = \sum_{s=1}^N \left[u_{ks} (1 - (1 - v_k) F_{kk}) - (1 - u_{ks}) (1 - v_k) \frac{A_s}{A_k} F_{sk} \right] \frac{\partial q_{o,s}}{\partial T_{f,i}} \quad (\text{Eq. 5-76})$$

Now, the temperature relation needs to be differentiated:

$$b_k = v_k \uparrow T_k^4 \quad (\text{Eq. 5-77})$$

$$\frac{\partial b_k}{\partial T_{f,i}} = \frac{\partial b_k}{\partial T_k} \frac{\partial T_k}{\partial T_{f,i}} \quad (\text{Eq. 5-78})$$

$$\frac{\partial b_k}{\partial T_k} = 4v_k \uparrow T_k^3 \quad (\text{Eq. 5-79})$$

$$\frac{\partial b_k}{\partial T_{f,i}} = 4v_k \uparrow T_k^3 \frac{\partial T_k}{\partial T_{f,i}} \quad (\text{Eq. 5-80})$$

Substituting this equation into Eq. (5-76) I obtain the following relation:

$$\sum_{s=1}^N \left[u_{ks} (1 - (1 - v_k) F_{sk}) - (1 - u_{ks}) (1 - v_k) \frac{A_s}{A_k} F_{sk} \right] \frac{\partial q_{o,s}}{\partial T_{f,i}} = 4v_k \uparrow T_k^3 \frac{\partial T_k}{\partial T_{f,i}} \quad (\text{Eq. 5-81})$$

This equation is reformulated to explicitly express the differential node temperature and the differential neighboring node temperature with respect to the fluid temperature:

$$\frac{\partial T_k}{\partial T_{f,i}} = \frac{1}{4v_k \uparrow T_k^3} \left(\sum_{s=1}^N \left[u_{ks} (1 - (1 - v_k) F_{sk}) - (1 - u_{ks}) (1 - v_k) \frac{A_s}{A_k} F_{sk} \right] \frac{\partial q_{o,s}}{\partial T_{f,i}} \right) \quad (\text{Eq. 5-82})$$

$$\frac{\partial T_t}{\partial T_{f,i}} = \frac{1}{4v_t \uparrow T_t^3} \left(\sum_{s=1}^N \left[u_{ts} (1 - (1 - v_t) F_{st}) - (1 - u_{ts}) (1 - v_t) \frac{A_s}{A_t} F_{st} \right] \frac{\partial q_{o,s}}{\partial T_{f,i}} \right) \quad (\text{Eq. 5-83})$$

In order to obtain the final equation the last two equations are put into Eq. (5-72):

$$\begin{aligned} & \sum_{s=1}^N \left[u_{ks} (1 - F_{sk}) - (1 - u_{ks}) \frac{A_s}{A_k} F_{sk} \right] \frac{\partial q_{o,s}}{\partial T_{f,i}} \\ &= \left(-h_k - \frac{1}{A_k} \sum_{t=1}^{N_{\text{Cmd}}} \frac{k_{kt}}{l_{kt}} A_{kt} \right) \frac{1}{4v_k \uparrow T_k^3} \left(\sum_{s=1}^N \left[u_{ks} (1 - (1 - v_k) F_{sk}) - (1 - u_{ks}) (1 - v_k) \frac{A_s}{A_k} F_{sk} \right] \frac{\partial q_{o,s}}{\partial T_{f,i}} \right) \\ &+ \frac{1}{A_k} \sum_{t=1}^{N_{\text{Cmd}}} \frac{k_{kt}}{l_{kt}} A_{kt} \frac{1}{4v_t \uparrow T_t^3} \left(\sum_{s=1}^N \left[u_{ts} (1 - (1 - v_t) F_{st}) - (1 - u_{ts}) (1 - v_t) \frac{A_s}{A_t} F_{st} \right] \frac{\partial q_{o,s}}{\partial T_{f,i}} \right) + u_{ki} h_i \end{aligned} \quad (\text{Eq. 5-84})$$

The final equation is found by separating RHS from LHS terms:

$$\begin{aligned}
& \sum_{s=1}^N \left[u_{ks} (1 - F_{sk}) - (1 - u_{ks}) \frac{A_s}{A_k} F_{sk} \right] \frac{\partial q_{o,s}}{\partial T_{f,i}} - \left(-h_k - \frac{1}{A_k} \sum_{t=1}^{N_{Cond}} \frac{k_{kt}}{l_{kt}} A_{kt} \right) \frac{1}{4v_k \dagger T_k^3} \\
& \quad * \sum_{s=1}^N \left[u_{ks} (1 - (1 - v_k) F_{sk}) - (1 - u_{ks})(1 - v_k) \frac{A_s}{A_k} F_{sk} \right] \frac{\partial q_{o,s}}{\partial T_{f,i}} \\
& - \frac{1}{A_k} \sum_{t=1}^{N_{Cond}} \frac{k_{kt}}{l_{kt}} A_{kt} \frac{1}{4v_t \dagger T_t^3} \sum_{s=1}^N \left[u_{ts} (1 - (1 - v_t) F_{st}) - (1 - u_{ts})(1 - v_t) \frac{A_s}{A_t} F_{st} \right] \frac{\partial q_{o,s}}{\partial T_{f,i}} = u_{ki} h_i
\end{aligned} \tag{Eq. 5-85}$$

Once the radiosity derivative has been calculated by Eq. (5-85), one can simply multiply the results vector by Eq. (5-82).

If the node temperature and all neighboring node temperatures are fixed, Eq. (5-72) can be taken. Since the derivative of node temperature with respect to fluid temperature will be zero in that particular case I can calculate the change of radiosity with respect to fluid temperature by the following equation:

$$\sum_{s=1}^N \left[u_{ks} (1 - F_{sk}) - (1 - u_{ks}) \frac{A_s}{A_k} F_{sk} \right] \frac{\partial q_{o,s}}{\partial T_{f,i}} = u_{ki} h_i \tag{Eq. 5-86}$$

With the radiosity derivative with respect to fluid temperature known, Eq. (5-65) can be used to calculate the change in net heat flux on that node.

5.3.4 Sensitivity to Conductance

Here, conductance C_{kt} is defined as:

$$C_{kt} = \frac{k_{kt}}{l_{kt}} A_{kt} \tag{Eq. 5-87}$$

The reason for deriving this lumped term instead of conductivity is the ease of extracting this information from the commercial solver. Again, I start my treatment of sensitivity on conductance with the following equation:

$$b_k = \sum_{s=1}^N \left[u_{sk} q_{o,s} - u_{sk} q_{o,s} F_{sk} - (1 - u_{sk}) \frac{A_s}{A_k} q_{o,s} F_{sk} \right] \tag{Eq. 5-88}$$

The total derivative with respect to conductance is:

$$\frac{\partial b_k}{\partial C_{ij}} = \sum_{r=1}^N \frac{\partial b_k}{\partial q_{o,r}} \frac{\partial q_{o,r}}{\partial C_{ij}} \quad (\text{Eq. 5-89})$$

$$\frac{\partial b_k}{\partial q_{o,r}} = \sum_{s=1}^N \left[u_{ks} (1 - F_{sk}) \frac{\partial q_{o,s}}{\partial q_{o,r}} - (1 - u_{ks}) \frac{A_s}{A_k} F_{sk} \frac{\partial q_{o,s}}{\partial q_{o,r}} \right] \quad (\text{Eq. 5-90})$$

$$\frac{\partial b_k}{\partial C_{ij}} = \sum_{s=1}^N \left[u_{ks} (1 - F_{sk}) - (1 - u_{ks}) \frac{A_s}{A_k} F_{sk} \right] \frac{\partial q_{o,s}}{\partial C_{ij}} \quad (\text{Eq. 5-91})$$

Equation (5-12) is rewritten with conductance as:

$$b_k = q_{imp,k} + h_k (T_{fk} - T_k) + \frac{1}{A_k} \sum_{t=1}^{N_{Cond}} (-C_{kt} (T_k - T_t)) \quad (\text{Eq. 5-92})$$

A full derivation is applied to get:

$$\frac{\partial b_k}{\partial C_{ij}} = \frac{\partial b_k}{\partial T_k} \frac{\partial T_k}{\partial C_{ij}} + \sum_{r=1}^{N_{Cond}} \frac{\partial b_k}{\partial T_r} \frac{\partial T_r}{\partial C_{ij}} + \sum_{r=1}^{N_{Cond}} \frac{\partial b_k}{\partial C_{kr}} \frac{\partial C_{kr}}{\partial C_{ij}} \quad (\text{Eq. 5-93})$$

$$\frac{\partial b_k}{\partial T_k} = -h_k - \frac{1}{A_k} \sum_{t=1}^{N_{Cond}} C_{kt} \quad (\text{Eq. 5-94})$$

$$\frac{\partial b_k}{\partial T_r} = \frac{1}{A_k} \sum_{t=1}^{N_{Cond}} C_{kt} \frac{\partial T_t}{\partial T_r} \quad (\text{Eq. 5-95})$$

$$\frac{\partial b_k}{\partial C_{kr}} = -\frac{1}{A_k} \sum_{t=1}^{N_{Cond}} (T_k - T_t) \frac{\partial C_{kt}}{\partial C_{kr}} \quad (\text{Eq. 5-96})$$

When changing a conductance from i to j the conductance from j to i will also change:

$$\frac{\partial C_{kt}}{\partial C_{ij}} = 1 : (i = k \wedge j = t) \vee (j = k \wedge i = t) \quad (\text{Eq. 5-97})$$

Putting the above relations into Eq. (5-93) one gets:

$$\frac{\partial b_k}{\partial C_{ij}} = \left(-h_k - \frac{1}{A_k} \sum_{t=1}^{N_{Cond}} C_{kt} \right) \frac{\partial T_k}{\partial C_{ij}} + \frac{1}{A_k} \sum_{t=1}^{N_{Cond}} C_{kt} \frac{\partial T_t}{\partial C_{ij}} - \frac{1}{A_k} \sum_{t=1}^{N_{Cond}} [(T_k - T_t) (u_{ik} u_{jt} + u_{it} u_{jk})] \quad (\text{Eq. 5-98})$$

This equation is set equal to Eq. (5-91):

$$\sum_{s=1}^N \left[u_{ks} (1 - F_{sk}) - (1 - u_{ks}) \frac{A_s}{A_k} F_{sk} \right] \frac{\partial q_{o,s}}{\partial C_{ij}} = \left(-h_k - \frac{1}{A_k} \sum_{t=1}^{N_{Cond}} C_{kt} \right) \frac{\partial T_k}{\partial C_{ij}} + \frac{1}{A_k} \sum_{t=1}^{N_{Cond}} C_{kt} \frac{\partial T_t}{\partial C_{ij}} - \frac{1}{A_k} \sum_{t=1}^{N_{Cond}} [(T_k - T_t)(u_{ik} u_{jt} + u_{it} u_{jk})] \quad (\text{Eq. 5-99})$$

The same procedure is applied to the second equation in Poljak's method:

$$b_k = \sum_{s=1}^N \left[u_{sk} q_{o,s} - u_{sk} (1 - v_k) q_{o,s} F_{sk} - (1 - u_{sk})(1 - v_k) \frac{A_s}{A_k} q_{o,s} F_{sk} \right] \quad (\text{Eq. 5-100})$$

$$\frac{\partial b_k}{\partial C_{ij}} = \sum_{r=1}^N \frac{\partial b_k}{\partial q_{o,r}} \frac{\partial q_{o,r}}{\partial C_{ij}} \quad (\text{Eq. 5-101})$$

$$\frac{\partial b_k}{\partial q_{o,r}} = \sum_{s=1}^N \left[u_{sk} \frac{\partial q_{o,s}}{\partial q_{o,r}} - u_{sk} (1 - v_k) F_{sk} \frac{\partial q_{o,s}}{\partial q_{o,r}} - (1 - u_{sk})(1 - v_k) \frac{A_s}{A_k} F_{sk} \frac{\partial q_{o,s}}{\partial q_{o,r}} \right] \quad (\text{Eq. 5-102})$$

$$\frac{\partial b_k}{\partial C_{ij}} = \sum_{s=1}^N \left[u_{sk} - u_{sk} (1 - v_k) F_{sk} - (1 - u_{sk})(1 - v_k) \frac{A_s}{A_k} F_{sk} \right] \frac{\partial q_{o,s}}{\partial C_{ij}} \quad (\text{Eq. 5-103})$$

$$b_k = v_k \uparrow T_k^4 \quad (\text{Eq. 5-104})$$

$$\frac{\partial b_k}{\partial C_{ij}} = \frac{\partial b_k}{\partial T_k} \frac{\partial T_k}{\partial C_{ij}} \quad (\text{Eq. 5-105})$$

$$\frac{\partial b_k}{\partial T_k} = 4v_k \uparrow T_k^3 \quad (\text{Eq. 5-106})$$

$$\frac{\partial b_k}{\partial C_{ij}} = 4v_k \uparrow T_k^3 \frac{\partial T_k}{\partial C_{ij}} \quad (\text{Eq. 5-107})$$

$$\sum_{s=1}^N \left[u_{sk} - u_{sk} (1 - v_k) F_{sk} - (1 - u_{sk})(1 - v_k) \frac{A_s}{A_k} F_{sk} \right] \frac{\partial q_{o,s}}{\partial C_{ij}} = 4v_k \uparrow T_k^3 \frac{\partial T_k}{\partial C_{ij}} \quad (\text{Eq. 5-108})$$

As was done for other parameters, the last equation is rearranged in order to express the temperature derivative with respect to conductance, explicitly:

$$\frac{\partial T_k}{\partial C_{ij}} = \frac{1}{4v_k \uparrow T_k^3} \sum_{s=1}^N \left[u_{sk} - u_{sk} (1 - v_k) F_{sk} - (1 - u_{sk})(1 - v_k) \frac{A_s}{A_k} F_{sk} \right] \frac{\partial q_{o,s}}{\partial C_{ij}} \quad (\text{Eq. 5-109})$$

$$\frac{\partial T_t}{\partial C_{ij}} = \frac{1}{4v_t \uparrow T_t^3} \sum_{s=1}^N \left[u_{st} - u_{st}(1-v_t)F_{st} - (1-u_{st})(1-v_t)\frac{A_s}{A_t}F_{st} \right] \frac{\partial q_{o,s}}{\partial C_{ij}} \quad (\text{Eq. 5-110})$$

Finally, Eq. (5-109) and Eq. (5-110) are substituted into Eq. (5-99):

$$\begin{aligned} & \sum_{s=1}^N \left[u_{ks}(1-F_{sk}) - (1-u_{ks})\frac{A_s}{A_k}F_{sk} \right] \frac{\partial q_{o,s}}{\partial C_{ij}} \\ - & \left(-h_k - \frac{1}{A_k} \sum_{t=1}^{N_{\text{Cond}}} C_{kt} \right) \frac{1}{4v_k \uparrow T_k^3} \sum_{s=1}^N \left[u_{sk} - u_{sk}(1-v_k)F_{sk} - (1-u_{sk})(1-v_k)\frac{A_s}{A_k}F_{sk} \right] \frac{\partial q_{o,s}}{\partial C_{ij}} \\ & - \frac{1}{A_k} \sum_{t=1}^{N_{\text{Cond}}} \left(C_{kt} \frac{1}{4v_t \uparrow T_t^3} \sum_{s=1}^N \left[u_{st} - u_{st}(1-v_t)F_{st} - (1-u_{st})(1-v_t)\frac{A_s}{A_t}F_{st} \right] \frac{\partial q_{o,s}}{\partial C_{ij}} \right) \\ & = -\frac{1}{A_k} \sum_{t=1}^{N_{\text{Cond}}} [(T_k - T_t)(u_{ik}u_{jt} + u_{it}u_{jk})] \end{aligned} \quad (\text{Eq. 5-111})$$

On the RHS there will be two entries. Once the radiosity derivative has been calculated by Eq. (5-111), one can simply multiply the results vector by Eq. (5-109).

If the node temperature is fixed, Eq. (5-99) can be taken. Since the derivative of node temperature with respect to conductance will be zero in that particular case we can calculate the change of radiosity with respect to conductance by the following equation:

$$\sum_{s=1}^N \left[u_{ks}(1-F_{sk}) - (1-u_{ks})\frac{A_s}{A_k}F_{sk} \right] \frac{\partial q_{o,s}}{\partial C_{ij}} = -\frac{1}{A_k} \sum_{t=1}^{N_{\text{Cond}}} [(T_k - T_t)(u_{ik}u_{jt} + u_{it}u_{jk})] \quad (\text{Eq. 5-112})$$

With the radiosity derivative with respect to conductance known, Eq. (5-91) can be used to calculate the change in net heat flux on that node.

5.3.5 Calculation Procedure for Sensitivity Coefficients

The method proposed here is a posteriori, because first, a conjugate heat transfer case needs to be calculated. The results of this simulation such as node temperature and radiosities need to be extracted along with geometric information, boundary conditions, and view factors in order to calculate the radiosity gradients as described in Eqs. (5-33), (5-60), (5-85), and (5-111). Because this has to be done for a change in every node, LU factorization has been employed. In this way, all

radiosity gradients are obtained by vector matrix multiplication. Once those radiosity gradients are known, temperature gradients as described in Eqs. (5-30), (5-57), (5-82), and (5-109) can be calculated. These gradients are used in Eq. (5-113) after rendering them dimensionless. Along with standard uncertainties actual temperature ranges can be provided by multiplying the combined standard uncertainty by the node temperature.

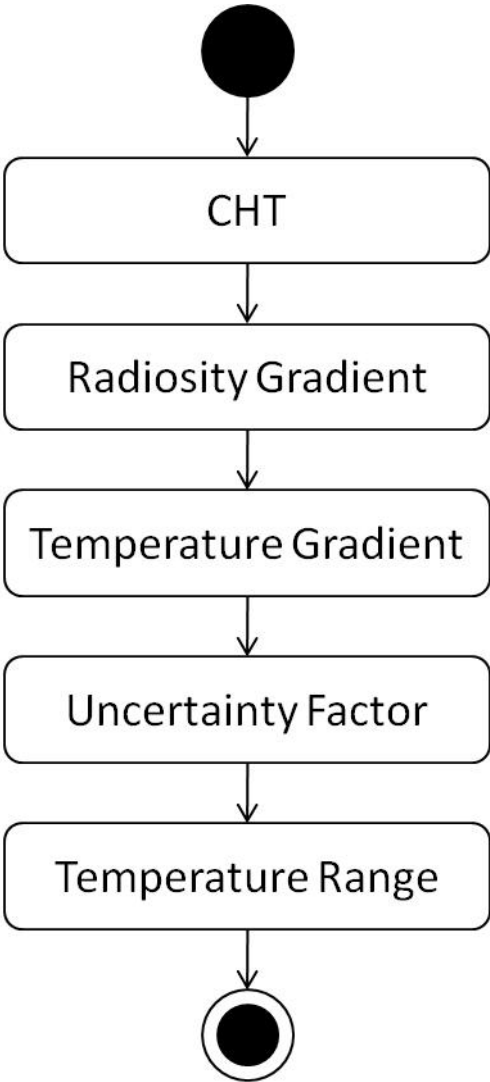


Figure 5-9: Activity diagram for calculation procedure.

Some other applications for sensitivity coefficients would be in inverse calculations and model reduction.

5.4 Uncertainty

The combined standard uncertainty can be formulated as follows:

$$\frac{u_c}{T_k} = \sqrt{\sum_{s=1}^N \left(\frac{v_s}{T_k} \frac{\partial T_k}{\partial v_s} \right)^2} u_v + \sqrt{\sum_{s=1}^N \left(\frac{T_{f,s}}{T_k} \frac{\partial T_k}{\partial T_{f,s}} \right)^2} u_{T_f} + \sqrt{\sum_{s=1}^N \sum_{t=1}^{N_{cmd}} \left(\frac{C_{st}}{T_k} \frac{\partial T_k}{\partial C_{st}} \right)^2} u_C + \sqrt{\sum_{s=1}^N \sum_{t=1}^N \left(\frac{F_{st}}{T_k} \frac{\partial T_k}{\partial F_{st}} \right)^2} u_f \quad (\text{Eq. 5-113})$$

It should be noted, that the standard uncertainties are drawn outside of the uncertainty factors. The reasons are that in general either not enough information is available on a local basis, or processing all bits of information would be cumbersome. Concerning the first issue, the present author already elaborated on the topic, that for partially obstructed view factors only for the simplest cases analytical view factors are available. Figure 5-7 provides a quick way of estimating view factor standard uncertainties, provided they were calculated by a random method, such as ray tracing or Monte Carlo integration. In many cases, expert knowledge is needed to estimate standard uncertainties. For the second issue, the example of emissivity might be given. In real word problems a material part does not have a single value of a property. The author has pointed out already, that various parameters such as soiling, temperature, state of oxidation, or influences of manufacturing can alter emissivity. Since these influences vary with space, also emissivity will. It is one thing making measurements of them, but quite another to use the information of special distribution in a commercial radiation solver and transfer it to uncertainty analysis. Usually, this information is averaged.

Another issue in Eq. (5-113) is the topic of scaling and dimension. The derivatives are also called sensitivity coefficients in this context. In order to compare or add them, they need to be made dimensionless as is demonstrated in the above equation. Taylor et al. (1995) did not multiply sensitivity coefficients by emissivity and view factor. The reasoning was that these two parameters are dimensionless and normalized. A value between zero and one is not always guaranteed for view factors, as Taylor and Luck (1995) showed. Therefore, I chose to normalize also emissivity and form factor. Consequently, when the view factor is zero, the sensitivity coefficient is also zero and does not contribute to the uncertainty coefficient. In another example, I use unscaled sensitivity coefficients.

5.5 Case Hexahedron

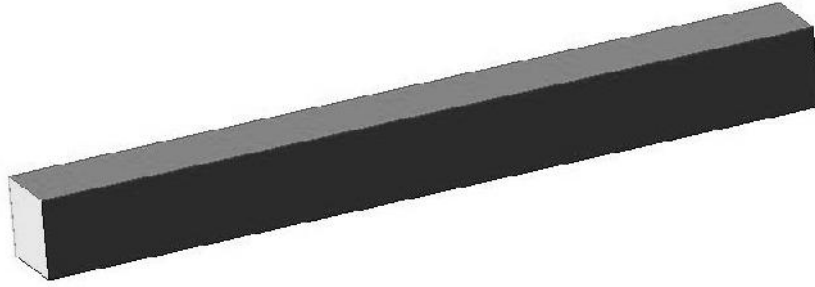


Figure 5-10: Case hexahedron.

A simple case shall be used to investigate uncertainty analysis. The hexahedron has a length of 0.9 m on the small side. The long side has a length of 9 m. The small front face is kept at a constant temperature. The temperatures of the other faces, that are facing each other, are calculated. All faces are insulated at the backside. Therefore, this system is a closed one. The boundary conditions are given in the following table. Conduction has been neglected.

Entity	Unit	Front	Other
ε	[-]	0,9	0,9
T	[K]	373,15	
h	[W/m ² /K]		1
T _f	[K]		293,15

Table 5-1: Boundary conditions for hexahedron.

Three different sets of view factors were employed by the thermal radiation solver RadThermIR: A setting with 512 rays cast without subdivision, another setting had a fourfold subdivision amounting to 294.912 rays per face, and finally analytically determined view factors which are shown in chapter 8.1. Since RadThermIR 9.3.1 was not able to import view factors a simple solver was written. The results for the relative deviations in view factor and temperatures for the three cases are shown in the following two figures where the relative error is defined as:

$$Error_{rel} = \frac{F_{analytic} - F_{calculated}}{F_{analytic}} * 100 \quad (\text{Eq. 5-114})$$

F is the analytical or actually calculated view factor. The energy source face is named 'Front' with the others named intuitively.

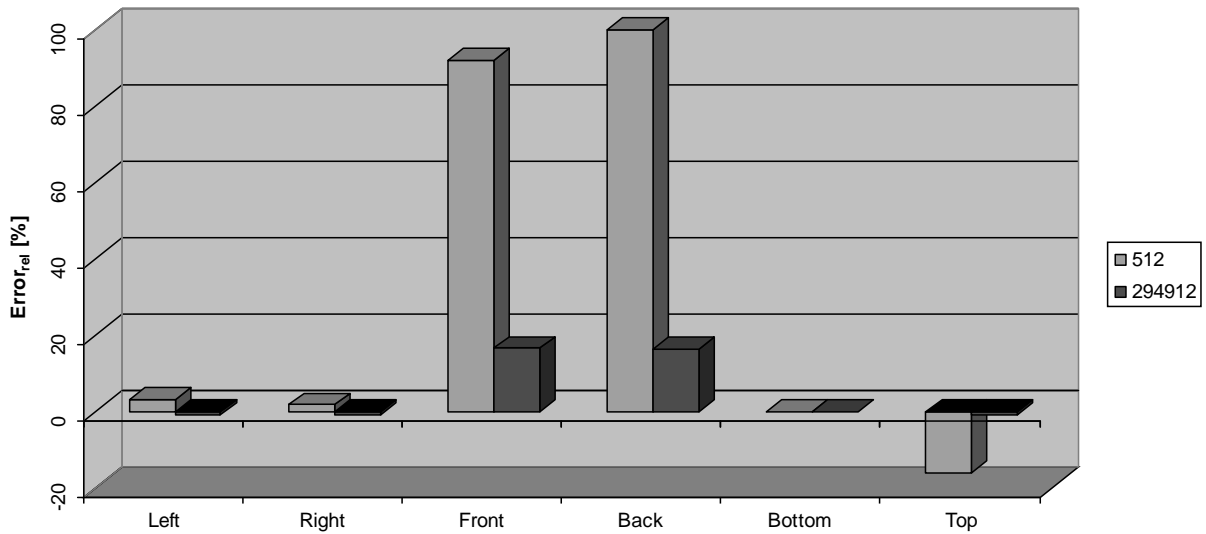


Figure 5-11: Relative view factor error for the hexahedron from face 'Bottom'.

The case with 512 rays shows, that the face 'Bottom' has a different view towards the back and front faces which should not be the case due to symmetry.

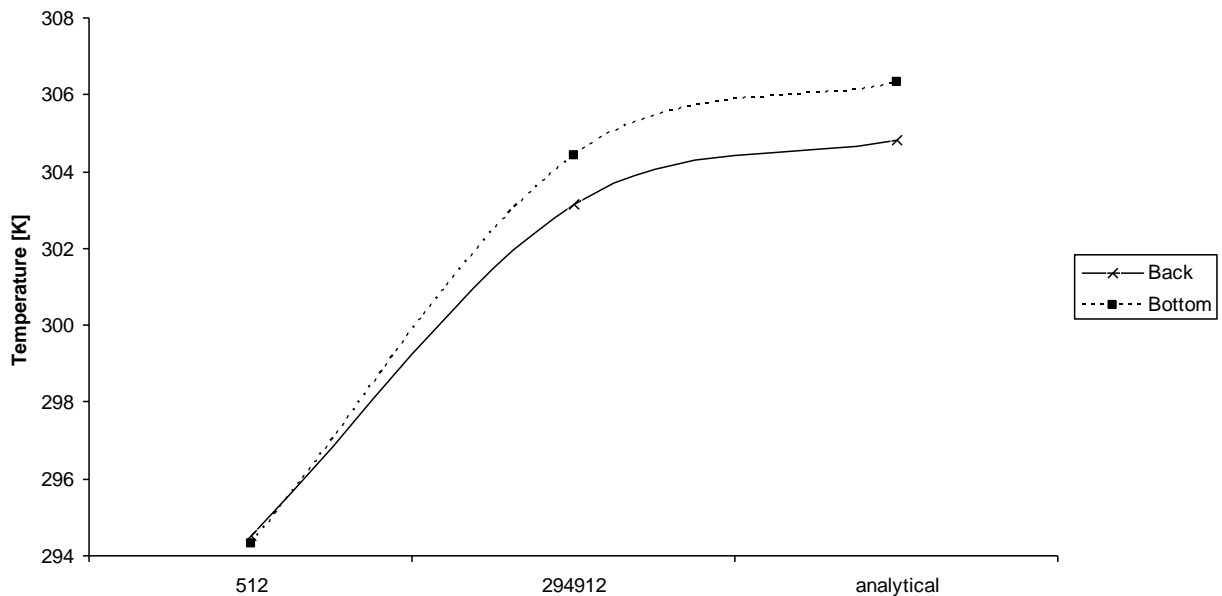


Figure 5-12: Calculated face temperatures for the hexahedron.

Next, the radiative heat fluxes from face 'Back' are drawn in the following diagram.

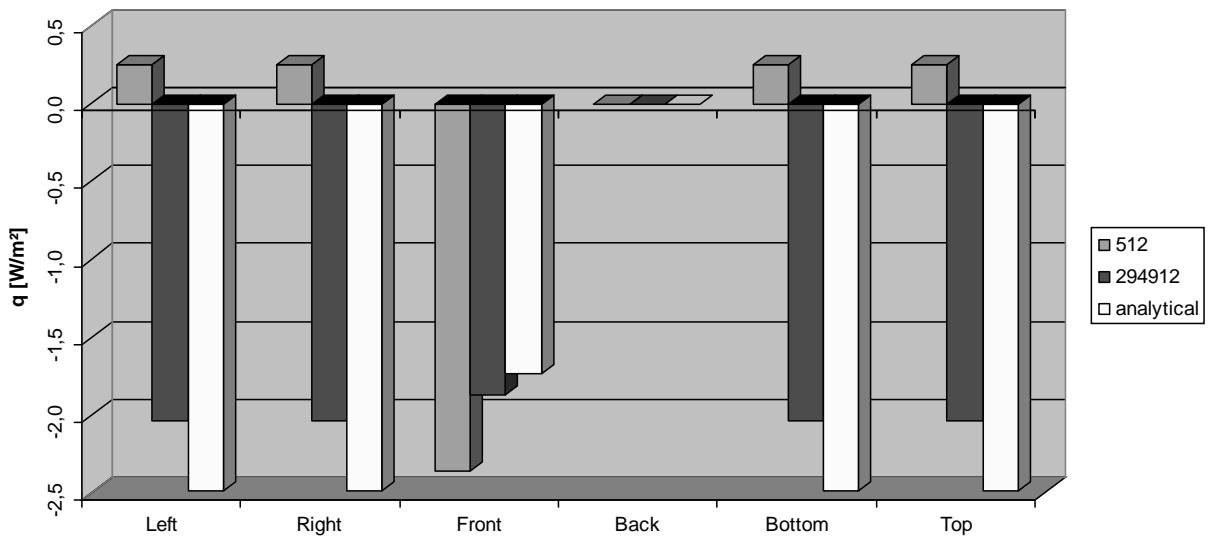


Figure 5-13: Radiative heat flux from face 'Back' for the hexahedron.

An increase in accuracy of view factors brings with it a change in radiative heat flux and radiosity.

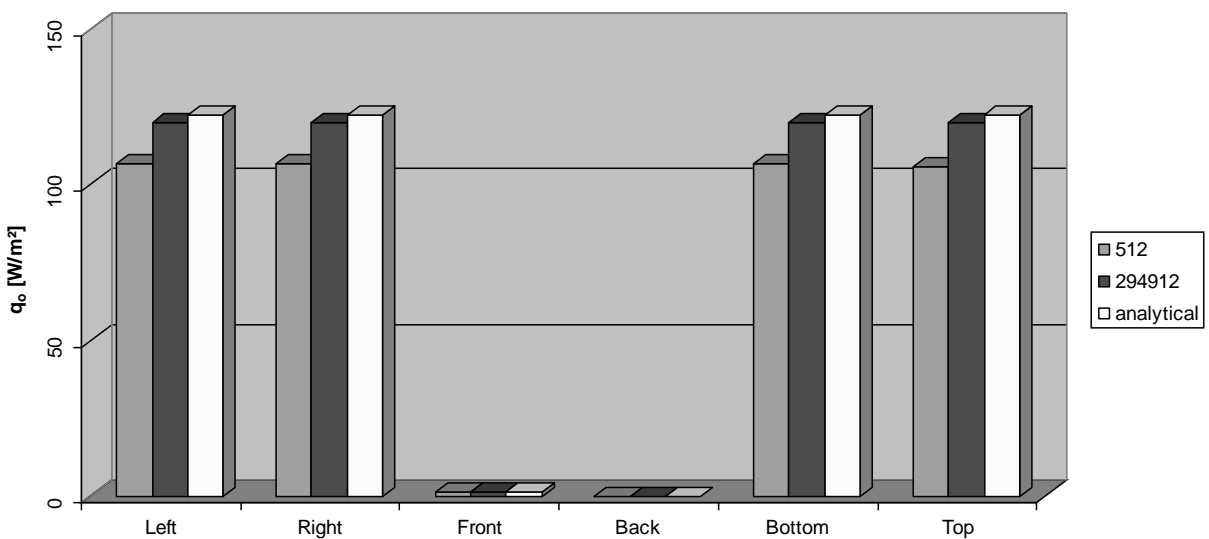


Figure 5-14: Radiosity flux from face 'Back' for the hexahedron.

The following diagram shows the calculated normalized sensitivity coefficients (SC) for emissivity when that variable is changed at the face 'Back'. In principle, the coefficients follow the trends of radiosity and net radiative flux. But the magnitude of change would not have been possible to predict by observing radiosity alone.

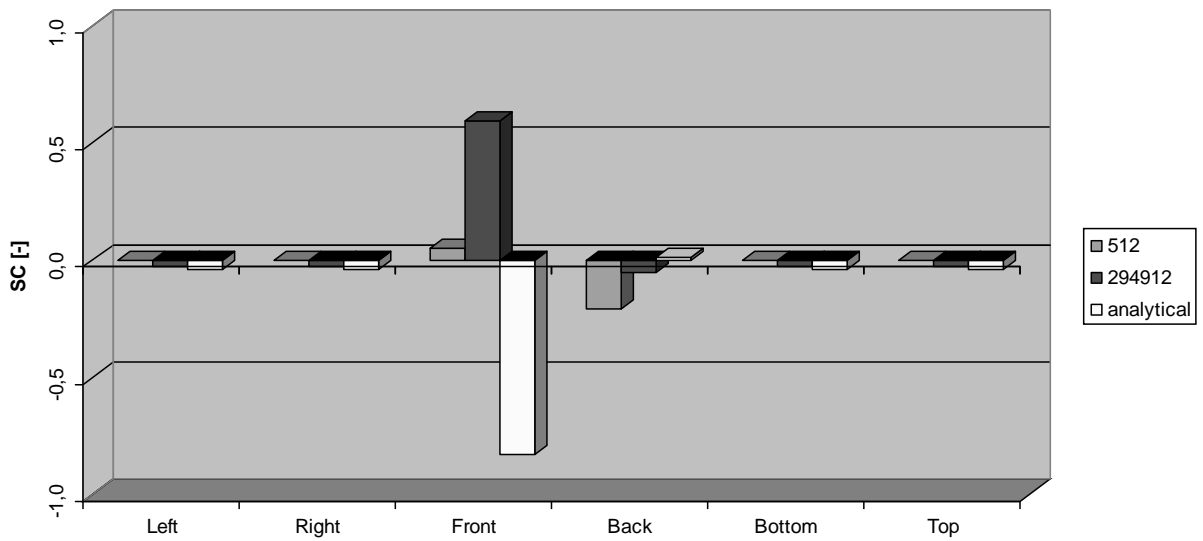


Figure 5-15: Dimensionless, normalized sensitivity coefficient of emissivity from face 'Back' for the hexahedron.

Sensitivity analysis, basically, is a first principle analysis for the energy balance which has been taken as a starting point. This analysis strives to unveil the change of the system when changing a parameter or even a model.

The sensitivity coefficient for the face 'Front' is larger in magnitude. This is a general observation for changes in heat fluxes as fluxes cause higher changes than changes in temperature would.

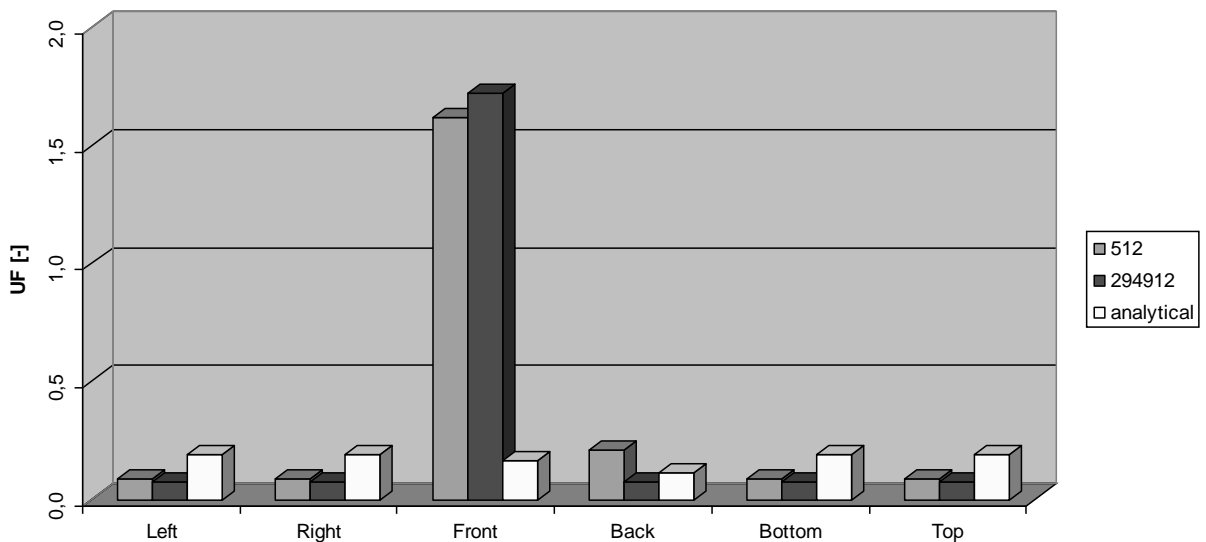


Figure 5-16: Uncertainty factor of emissivity for the hexahedron.

The uncertainty factor (UF) is the sum of the changes from all faces of the system. This makes it rather unpredictable which factor will raise or fall for complex systems. Even in this simple case it would not be possible to explain why these uncertainty factors with analytical view factors do not follow the trend that the low and high quality form factors suggest. For this reason it would be dangerous to shortcut obtaining the sensitivity coefficients of the whole system in order to speed-up the calculation. This would require a deep understanding of the system at hand which is often lacking in industrial settings.

The reader is invited to draw his attention to the behavior of form factor uncertainties.

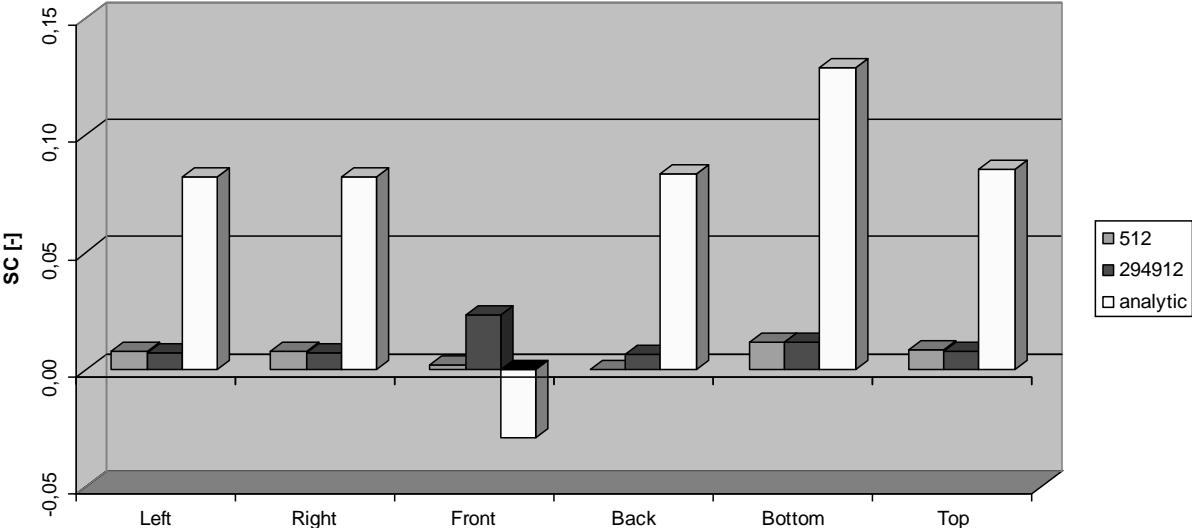


Figure 5-17: Dimensionless, normalized sensitivity coefficient of form factor from face ‘Back’ to ‘Bottom’ for the hexahedron.

The rise in temperature for the analytic setting was accompanied by a rise in the net radiation and radiosity flux. Consequently, the system will be more responsive to changes. But for the entire system, sensitivity coefficients did not change much.

$$RMS = \frac{1}{N} \sqrt{\sum^N (SC_{analytic} - SC_{calc})^2} \tag{Eq. 5-115}$$

The root mean square (RMS) is here defined with N as the number of sensitivity coefficients for either a change of temperature or a change of radiation flux. For the temperature SC the RMS changes from 0.0055 for 512 rays to 0.005 for the large ray setting.

The net radiation flux RMS for sensitivity coefficients from the face 'Front' rises from 0.0075 to 0.0356. The trends show that sensitivity coefficients for heat fluxes change more than those for temperature.

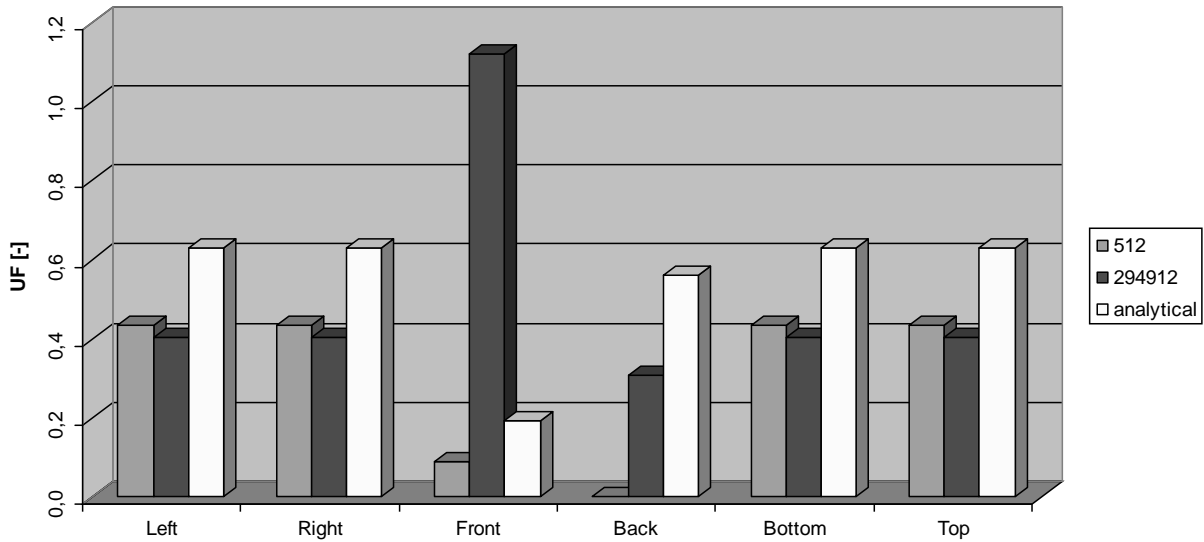


Figure 5-18: Uncertainty factor of form factor for the hexahedron.

The uncertainty factor (UF) of dimensionless, normalized SC of view factors did actually rise. One might intuitively expect view factor UF to reduce with improved view factors. But form factors are responsible for the geometric distribution of radiation fluxes. A change in configuration factors leads simply to a redirection of the fluxes and the uncertainty equations in this chapter are based on the change of those fluxes. The UF based on heat flux change sees a remarkable reduction for the analytical case which compensates somewhat the rise at the other faces. Taylor et al. (1995) showed that a significant change in sensitivity coefficients is expected when the summation and reciprocity relation were violated and put into order.

To finish this simple hexahedron case, the uncertainty factors for the fluid temperature T_f are shown in the next figure. Because the radiative heat flux is rising, the influence of convection is diminishing slightly. The face 'Front' did not have convection defined. When one compares Figure 5-16, Figure 5-18, and Figure 5-19, one can see that view factors have the most significant influence in the system, followed by the fluid temperature. Emissivity has only a small influence in the system.

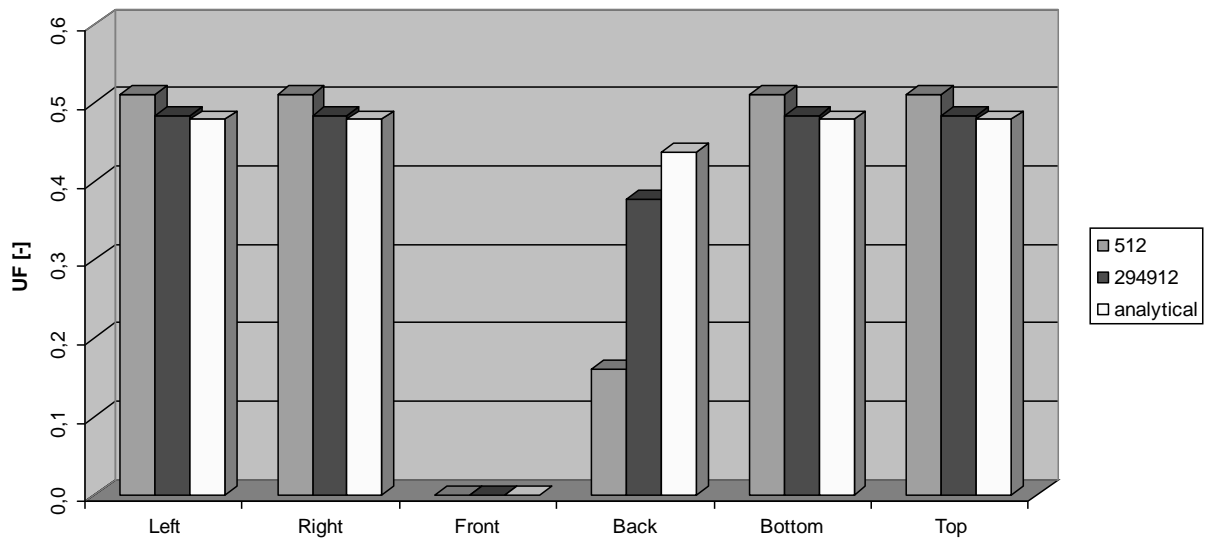


Figure 5-19: Uncertainty factor of T_f for the hexahedron.

5.6 Numerical Analysis

Another example shall serve for a numerical analysis.

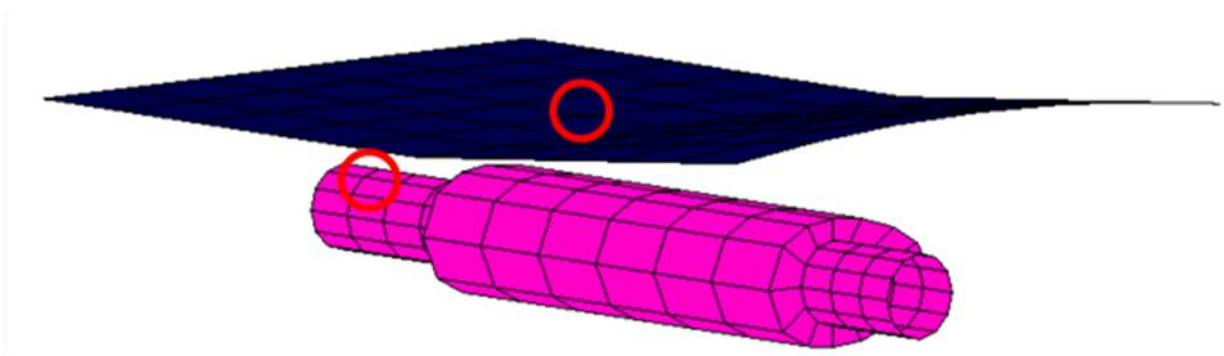


Figure 5-20: Muffler with two test faces.

A generic muffler without internals is used as a case. The geometry consists of 260 quadrilaterals. The muffler is topped by a heat shield. The case is set up in RadThermIR 9.1. An in-built heat transfer model was used. The exterior boundary conditions were chosen in a way that would be similar to a highway drive. They are shown in the following table. The form factors were calculated with 512 rays per face. The exhaust gas is modeled as air without soot formation. Though a severe simplification, the exhaust gas serves merely as a heat source. The exhaust gas itself is held at a constant temperature.

Entity	Unit	Heatshield	Muffler	
			Outside	Inside
Emissivity	[-]	0,6	0,216	0,9
Thickness	[m]	0,002	0,001	0,001
Conductivity	[W/m/K]	17,3056	52,019	52,019
Air Velocity	[m/s]	20	20	20
Air Temperature	[K]	303	303	413

Table 5-2: Boundary conditions for the muffler.

5.6.1 Numerical Stability

Attempting to implement an iterative solver failed because of instability. Therefore, a numerical analysis was conducted.

The Gershgorin circle theorem helps in estimating eigenvalues and thus stability of a solver because it gives the maximum possible value of λ by the radius r . The eigenvalue λ assures stability if it is less than or equal to 1. This is guaranteed when the radius r is less than or equal 0.5. In that case it can be expected, that the set of equations can be handled by an iterative solver without preconditioning. N is the number of entries of the solution matrix and a_{ij} are actual entries.

$$r = \sum_{\substack{j=1 \\ j \neq i}}^N |a_{ij}| \quad (\text{Eq. 5-116})$$

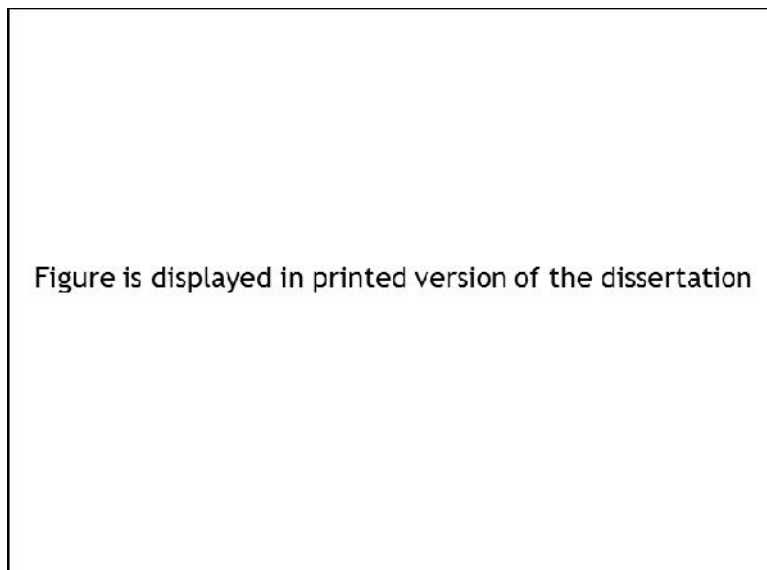


Figure 5-21: Stability analysis for the radiation term for the muffler (Rauch and Almbauer, 2010). Copyright © 2010 by AIAA, Inc. Reprinted with permission of the American Institute of Aeronautics and Astronautics.

The first 60 nodes constitute the heat shield. The next 200 nodes belong to the exterior of the muffler, and the last 200 nodes constitute the inside of the muffler. Figure 5-21 shows the value of the main diagonal entry a_{ii} which is always one. Here, only the radiation term for sensitivity coefficients is employed. All heat shield entries are below one. Diagonal dominance is another assurance of numerical stability. Just one entry of the exterior is greater than one but many entries of the interior of the muffler. Consequently, stability is not assured.

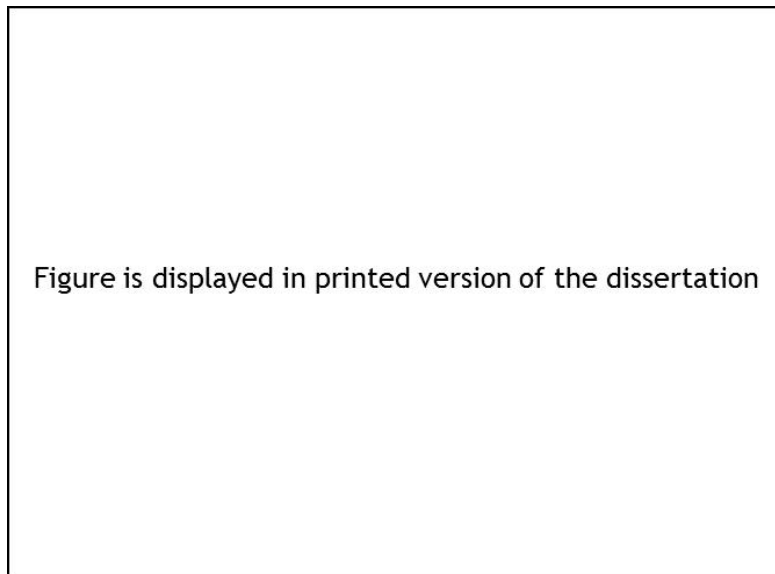


Figure 5-22: Stability analysis for radiation and convective terms for the muffler (Rauch and Almbauer, 2010). Copyright © 2010 by AIAA, Inc. Reprinted with permission of the American Institute of Aeronautics and Astronautics.

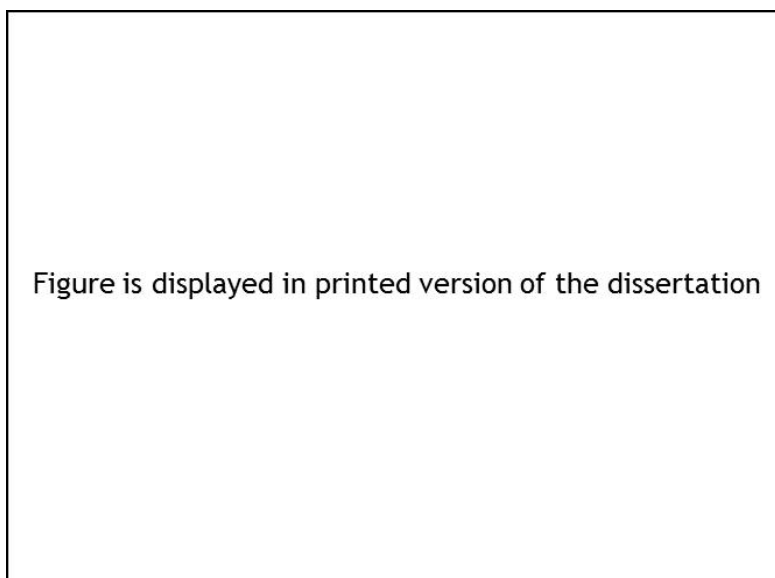


Figure 5-23: Stability analysis for radiation and conduction terms for the muffler (Rauch and Almbauer, 2010). Copyright © 2010 by AIAA, Inc. Reprinted with permission of the American Institute of Aeronautics and Astronautics.

When using both radiative and convective terms in the calculations, diagonal dominance assures stability as demonstrated in Figure 5-22.

But when using the radiative and conductive terms as in Figure 5-23, the inside of the muffler will prevent convergence, to which the present author can testify.

For the sake of completeness, the stability analysis for the case when all heat transfer modes are taken into account is shown.

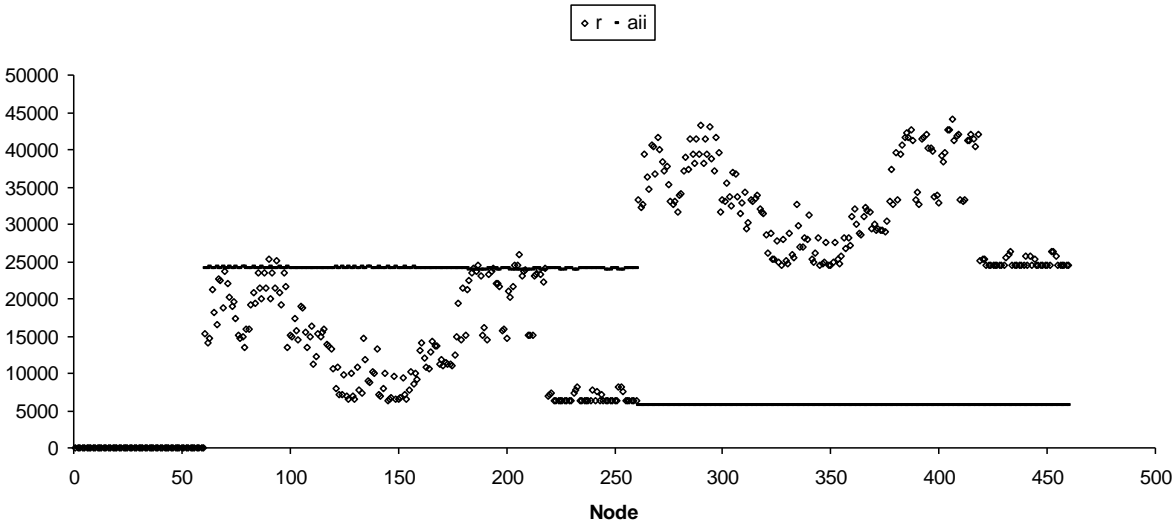


Figure 5-24: Stability analysis for radiation, convection, and conduction terms for the muffler.

In order to achieve a solution, the suggestion of Taylor et al. (1995) was followed by implementing an LU factorization algorithm. Unfortunately, this solver will be, to the present author’s best knowledge, not suitable for large industrial models except for a parallelized distributed memory version. Otherwise, an iterative solver would be needed, and hence, there would be a need for a suitable preconditioner.

The infinity norm $\|M\|_\infty$ is another indicator for stability.

$$\|M\|_\infty = \max_{1 \leq i < N} \sum_{j=1}^N |a_{ij}| \tag{Eq. 5-117}$$

M is the solution matrix and the other parameters are defined as in Eq. (5-116). The values are in the order of the just conducted stability analysis, 2.2, 61.2, 49856.6, and 49915.7. These values show in increased likelihood for instability.

5.6.2 Partial Uncertainties

To round-up the present test case, the first-principle analysis of two faces, as marked in Figure 5-20, is presented in the following table.

Node 28 is situated at the center of the heat shield. Radiation has the largest value, which would presume it will have the largest impact on a change followed by convection. Node 96 indicates that conduction is the most important term followed by convection.

Node	28	96
	[W/m ²]	
Radiation	21,22	-91,08
Convection	-19,16	-3.598,71
Conduction	-2,00	3.688,99

Table 5-3: Heat fluxes for two nodes of the muffler.

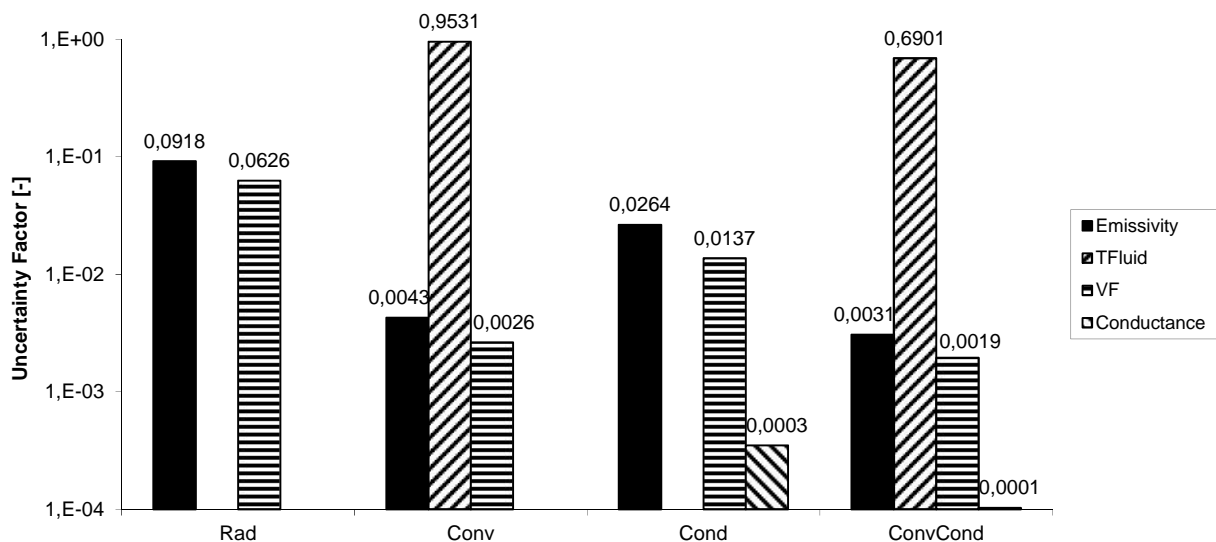


Figure 5-25: Partial uncertainty calculation for node 28 of the muffler system.

Usually, partial uncertainty calculation is practiced when calculating certain differentials becomes too cumbersome. Though this is not applicable in this case, it serves as a demonstration how interactions between the parameters have been taken care of.

The first column in Figure 5-25 has been calculated with the radiation term, only. Both emissivity and view factors (VF) exhibit values well below one, indicating that their influence might not be dominant. The second column deals with radiation and convection terms. Fluid temperature clearly shows its prominent role for that node. Emissivity and view factor dropped by one order of magnitude. When considering the radiation and conduction terms, emissivity and view factor dominate by two orders of magnitude. Considering all heat transfer modes yields the last column. Now, conductance becomes even more insignificant as expected by the heat flux magnitude. But convection dominates the results in change, which could not have been predicted by fluxes alone. A significant change in accuracy, such as fulfilling reciprocity and closure relation, or the realization of obstructions could alter uncertainties of form factors, significantly.

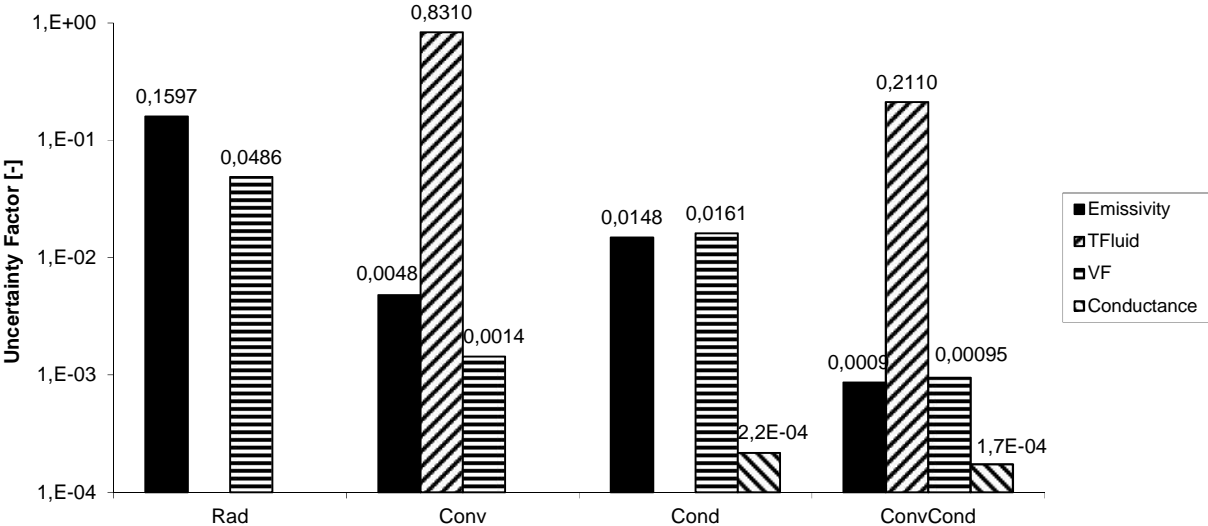


Figure 5-26: Partial uncertainty calculation for node 96 of the muffler system.

A similar behavior is found for node 96. Here, heat fluxes predict dominance of conduction, whereas convection prevails as the most important factor for change. Conductance, actually, plays no role in this example. Including conductance in the observations lets the UF of the view factor slightly overtake the UF for emissivity. It should be stressed, that all the equations are based on radiosity, where view factors play a prominent role. A discontinuity, whether an obstruction is partial or complete, could not be foreseen by this method.

5.6.3 Accuracy of Uncertainty Prediction

Finally, the question remains how accurate those predictions of the uncertainty analysis are. To answer that question, a separate calculation of the muffler was conducted with the only change of lowering the external air temperature by 10 K.

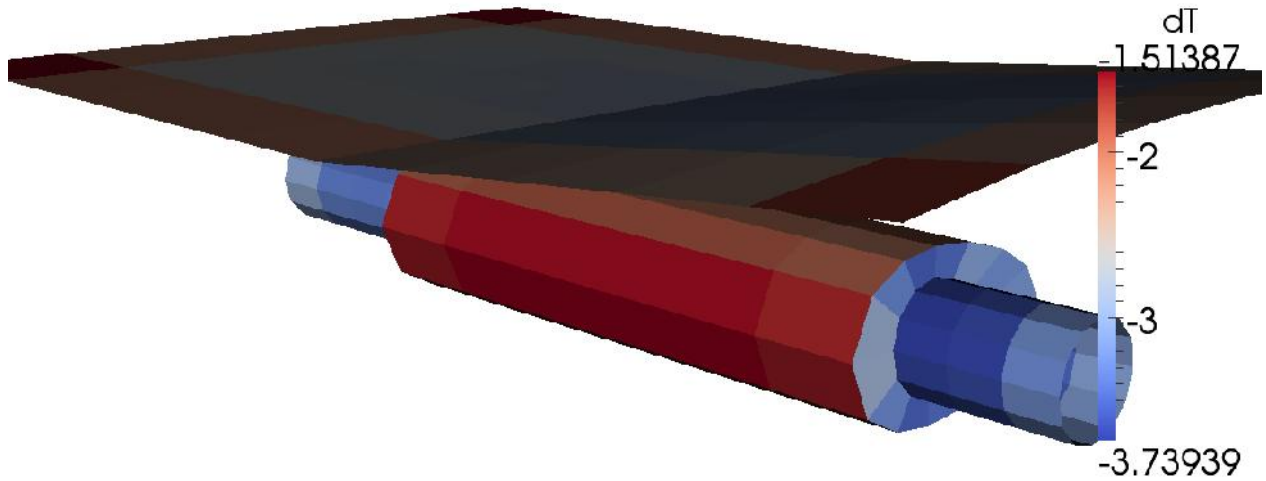


Figure 5-27: Difference of new simulation with prediction by uncertainty of the front nodes.

The values above were calculated as follows:

$$\Delta T_k = T_{k293} - (T_k - T_k UF_f u_f) \quad (\text{Eq. 5-118})$$

ΔT_k is the difference between simulated node temperature T_{k293} with new boundary condition and original simulated temperature T_k , uncertainty factor UF_f , and standard uncertainty u_f for the change in external air temperature.

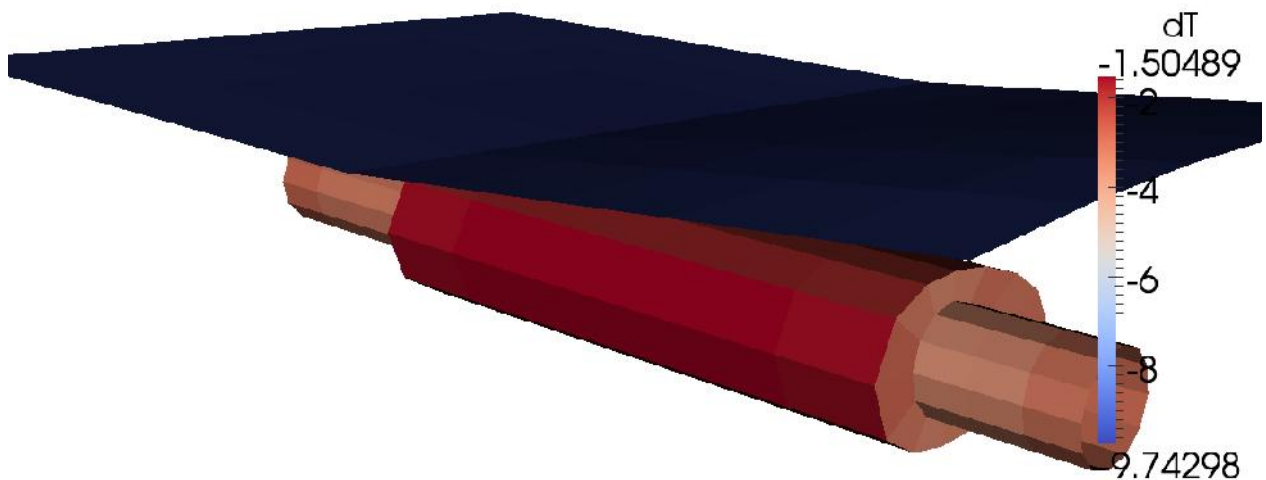


Figure 5-28: Difference of new simulation with prediction by uncertainty of the backside nodes.

The last figure shows, that when the uncertainty factor becomes zero, as it happens to the back of the heat shield, no combined uncertainty can be calculated. In this example, this happens because the back of the heat shield is treated as isolated for radiation. The only way those backside nodes receive energy, is by conduction. But in real world models, radiation and reflection can only be switched off when the mass has no internal energy at exactly 0 K, which has not been detected yet, and the material is either a black body or is positioned inside a black cavity. These are extreme out-of-the-world conditions, which not even spacecrafts are exposed to.

For sake of completeness, uncertainty factors for this example are presented in chapter 8.2.

Another, more simple example is investigated where conduction plays a larger role.

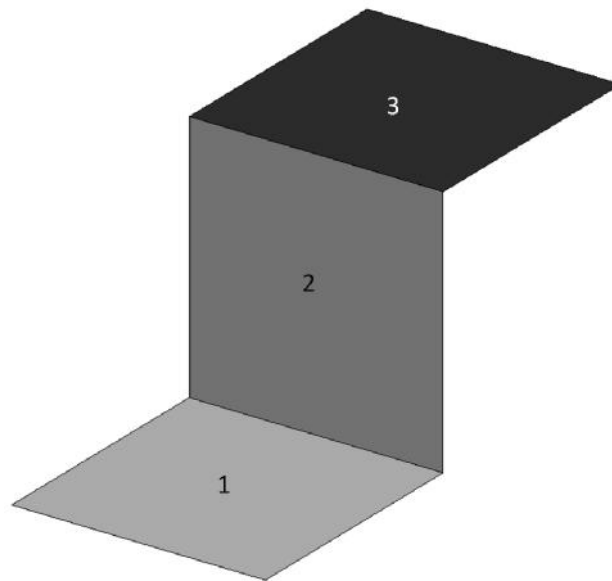


Figure 5-29: Case step.

The step example consists of three squares as thermal nodes with a side length of 0.1 m. To simplify the analysis the backside has been isolated. On node '1' a heat of 50 W is imposed. The step is placed inside a box in order to simulate the environment by a constant radiation temperature. Properties and boundary conditions for the base setting can be taken from Table 5-4.

Entity	Unit	
Emissivity	[-]	0,9
Thickness	[m]	0,01
Air Temperature	[K]	293,15
Heat Transfer Coefficient	[W/m ² /K]	10
Radiation Temperature	[K]	293,15
Conductivity	[W/m/K]	100
Density	[kg/m ³]	8000
Specific Heat	[J/kg/K]	800

Table 5-4: Boundary conditions for the step example.

Nodes '1' and '2' have no radiative heat exchange with node '3' because the respective view factors have the value zero. Node '3' only receives information on changes in heat fluxes from the other nodes by conduction. A steady-state solution with the aforementioned heat flux on node '1' is obtained.

A simulation experiment is conducted by changing various parameters from the base setting. In order to investigate the changes on the fluid temperature Figure 5-30 shows the temperatures of the step.

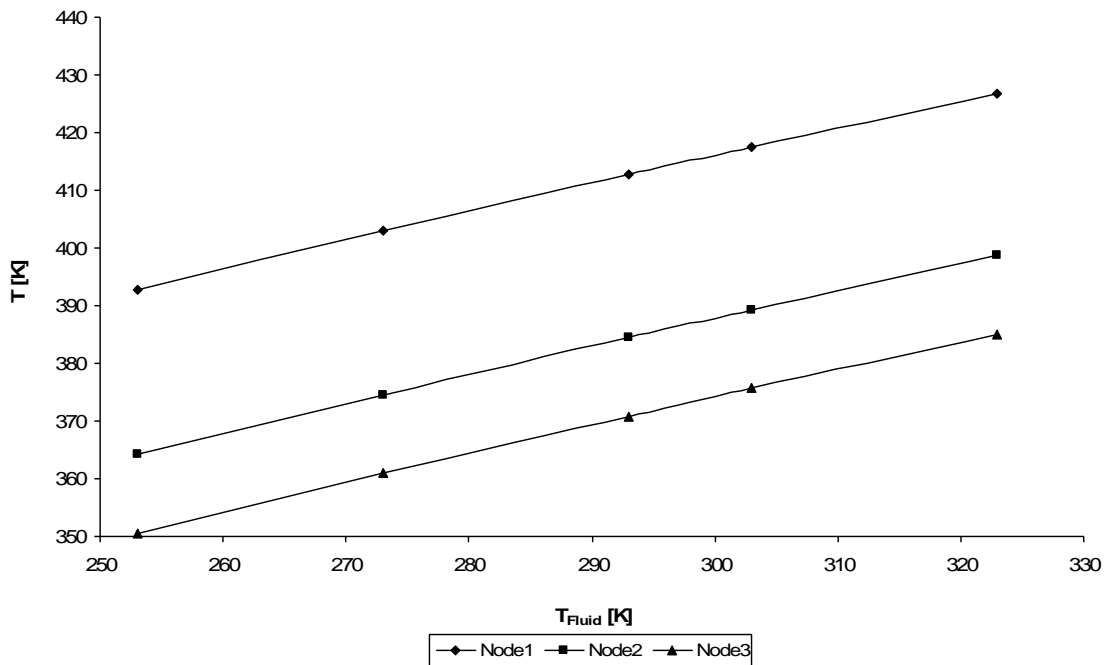


Figure 5-30: Temperatures for Step at $Q=50W$ with changing fluid temperature.

These changes are almost linear and it can be assumed that local sensitivity coefficients can predict this behavior well. Because the sensitivity coefficients for

the three thermal nodes share the same sign and the changes in fluid temperature are the same as well, uncertainty factors can be used to predict the resulting node temperatures.

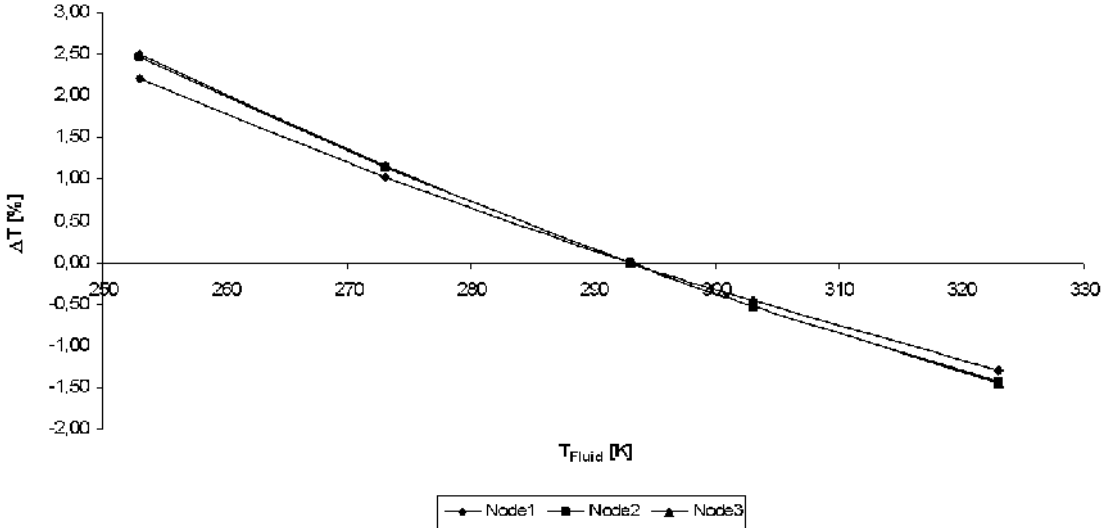


Figure 5-31: Temperature differences for Step at Q=50W with changing fluid temperature.

Eq. (5-118) has been used but with dimensional uncertainty factors and differences as standard uncertainties. Figure 5-31 shows the deviations between temperatures obtained by UFs at the base setting and temperatures obtained by simulations with changed fluid temperature. As expected the deviations are small over the entire range.

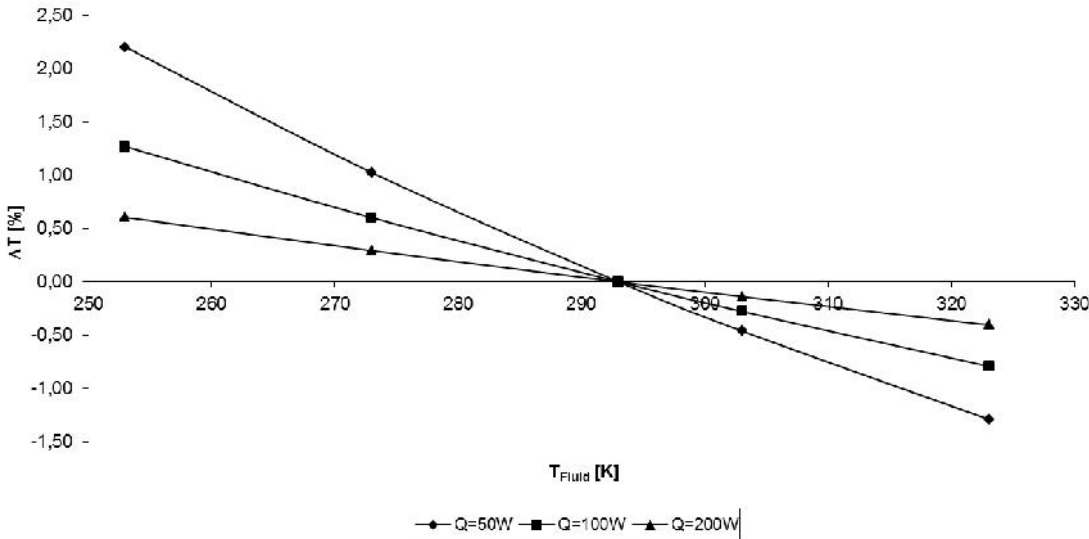


Figure 5-32: Temperature differences for Step with different heat sources and changing fluid temperature.

When using different heat fluxes at node ‘1’, the tendency is basically the same, when considering that at higher heat fluxes the node temperatures are higher.

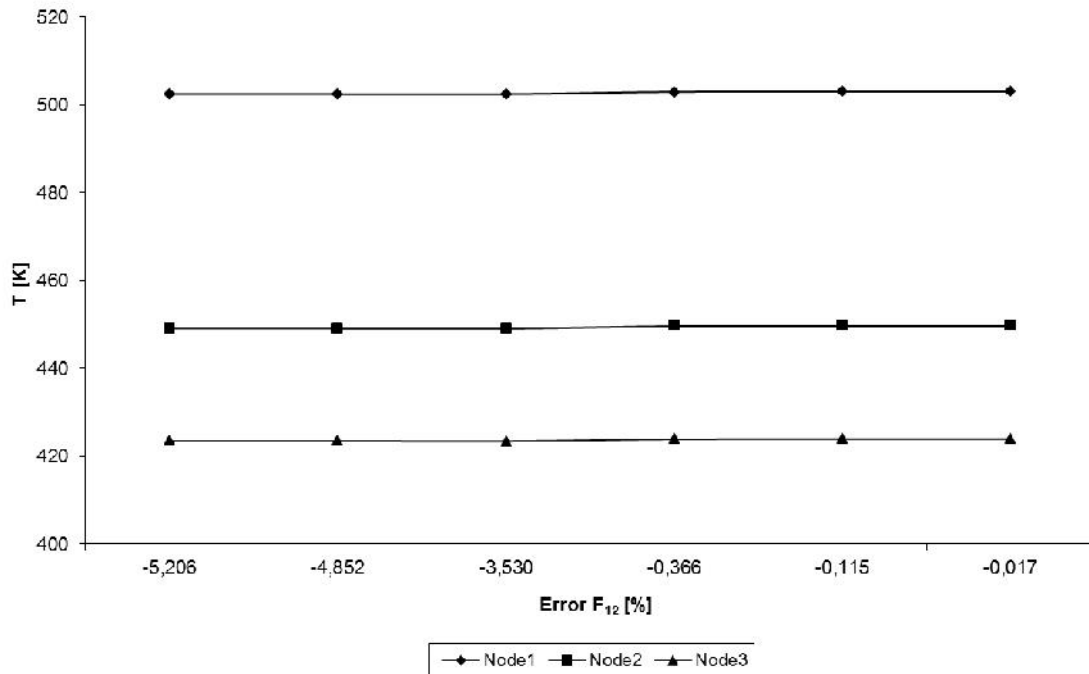


Figure 5-33: Temperatures for Step at $Q=50W$ with changing view factor error.

In Figure 5-33 the temperatures are depicted over the error of the view factor from node ‘1’ to ‘2’ to the analytical value. This view factor has been chosen, because only between these two nodes of the example there is a view. There is also a view from the three nodes to the environment, which was taken into account for the sensitivity estimations but shall not be investigated here. As with Figure 5-30 the temperature curves are linear. On the abscissa it can be seen, that the error is quite small which speaks of the quality of the code used. Figure 5-34 shows the differences between simulated and by UFs estimated node temperatures when view factors do change. At this point, there is a comment on this methodology necessary. The method presented does calculate sensitivities between nodes even when there is no view between them. Also, planarity is ignored, which increases UFs unnecessarily. Node ‘3’ only sees the environment and, therefore, it is presumed that it has the largest errors in this diagram. The other two nodes do have a view between them such that this unwanted effect is less pronounced. When changing the heat source at node ‘1’ the deviations are higher with higher heat fluxes, which substantiates the suspicion just raised.

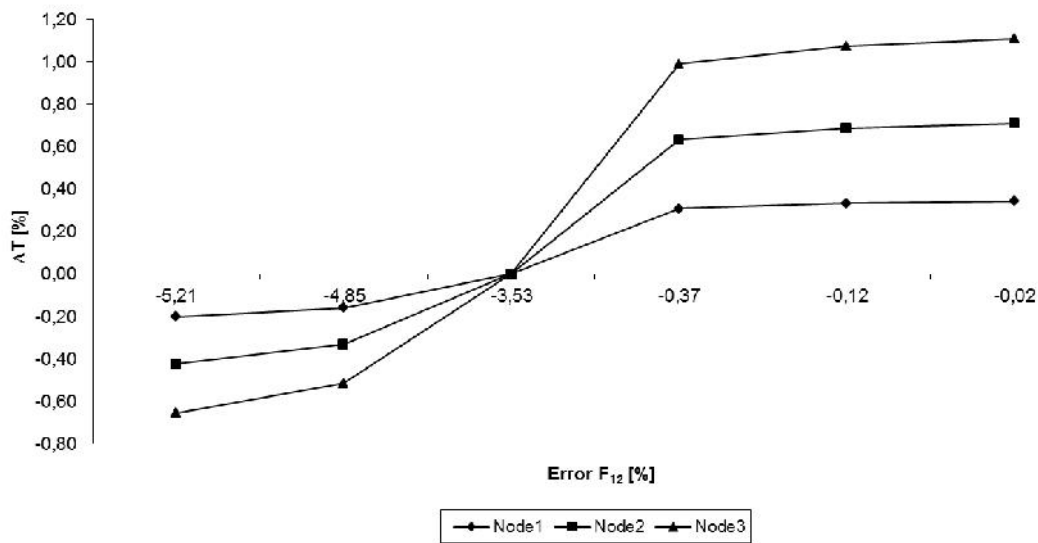


Figure 5-34: Temperature differences for Step at $Q=50W$ with changing view factors.

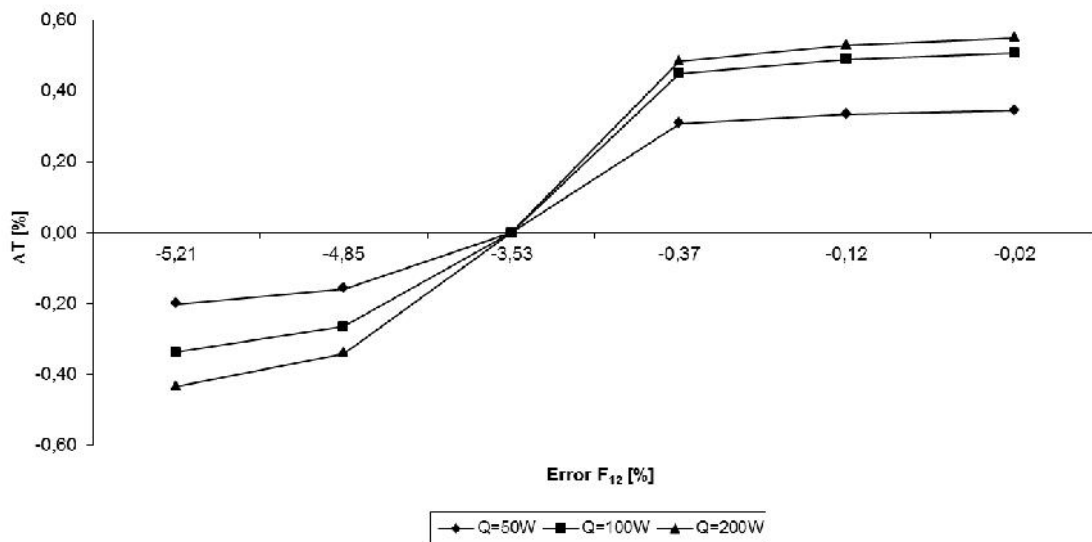


Figure 5-35: Temperature differences for Step with different heat sources and changing view factors.

In order to remedy this issue un-scaled UFs seem to be the wrong choice. When scaling them, only sensitivities are left where there is an actual view. As view factors usually do not change homogeneously, standard uncertainties, or in this case deviations, should be multiplied for each individual sensitivity coefficient resulting in importance factors. But all in all, the deviations are very small in this example.

When looking at the temperature curves for changing emissivity the non-linearity of the system is revealed.

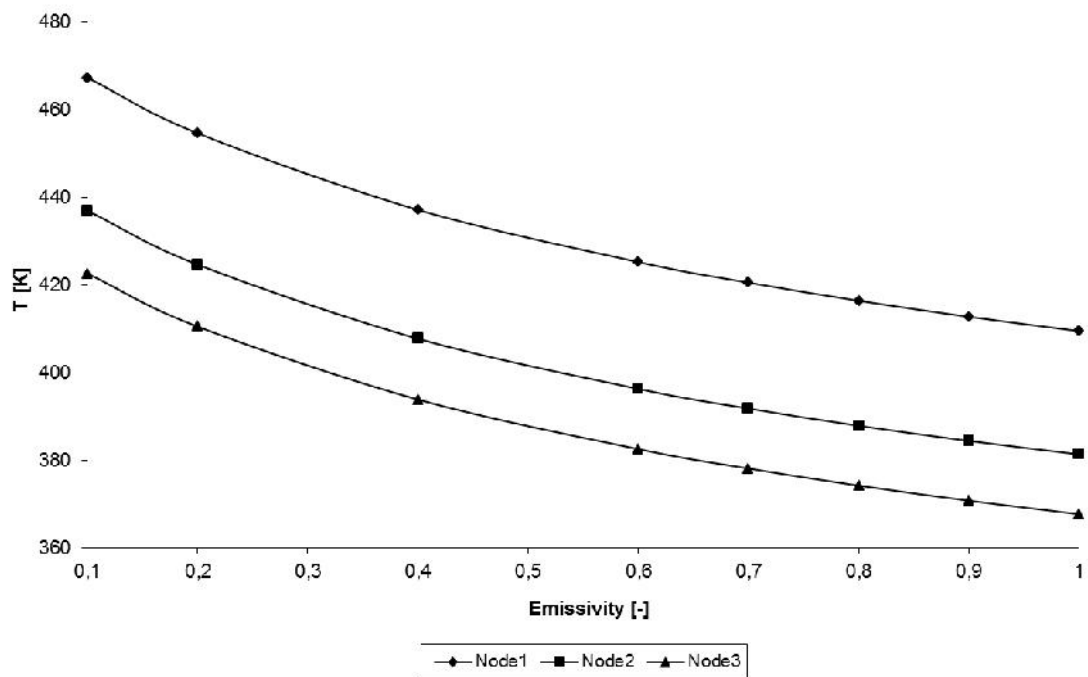


Figure 5-36: Temperatures for Step at Q=50W with changing emissivity.

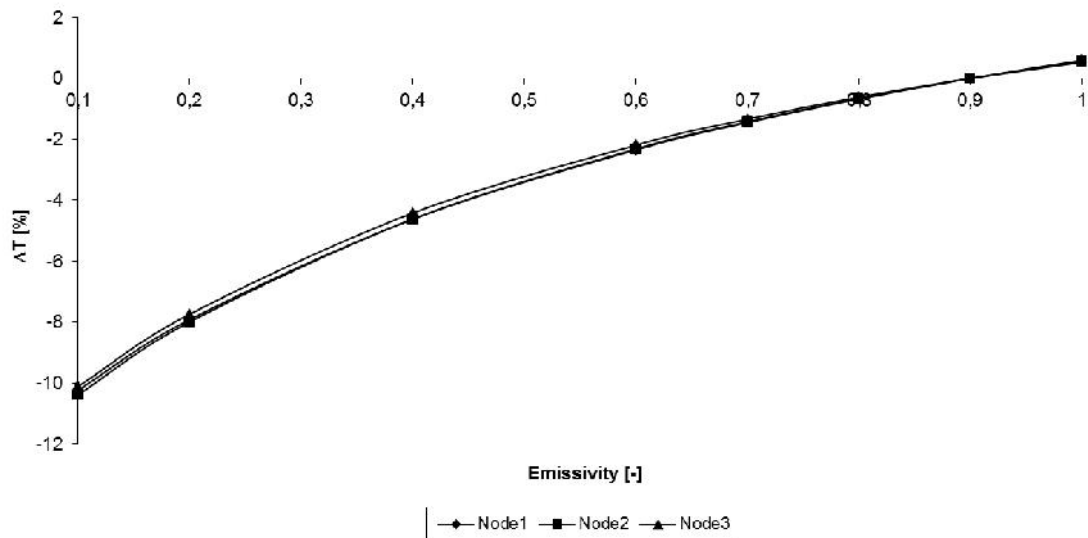


Figure 5-37: Temperature differences for Step at Q=50W with changing emissivity.

As expected, the greater the non-linear behavior, the greater the deviations. This observation is confirmed when raising the heat flux at node '1'. The highest input reveals the highest deviations.

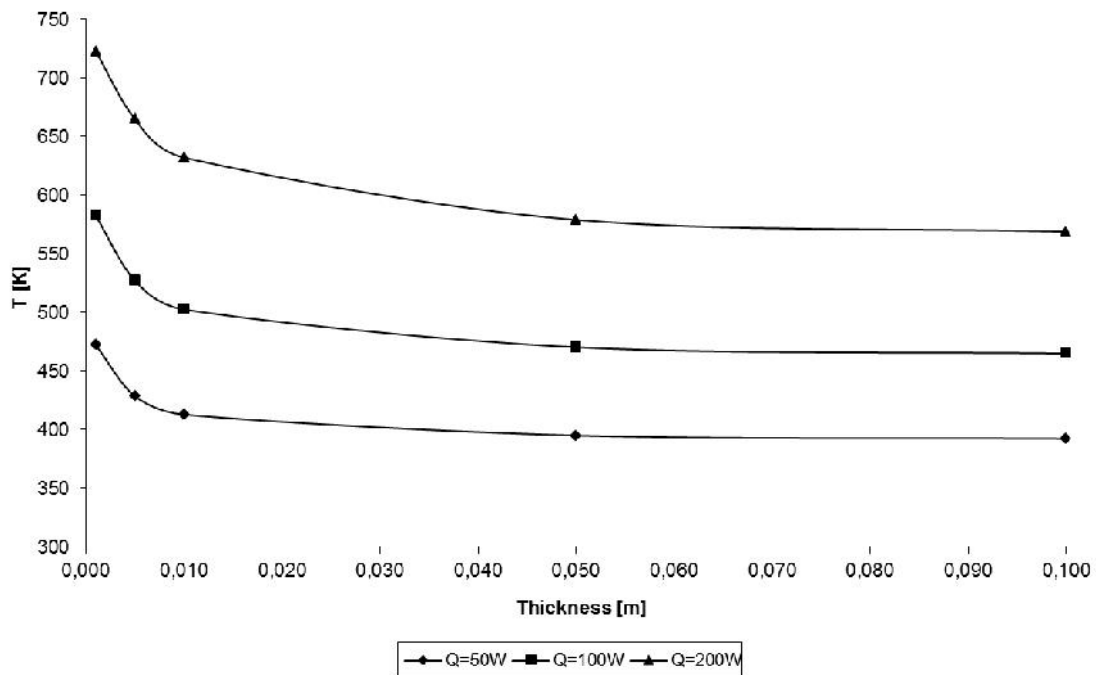


Figure 5-38: Temperatures for Step with different heat sources and changing emissivity.

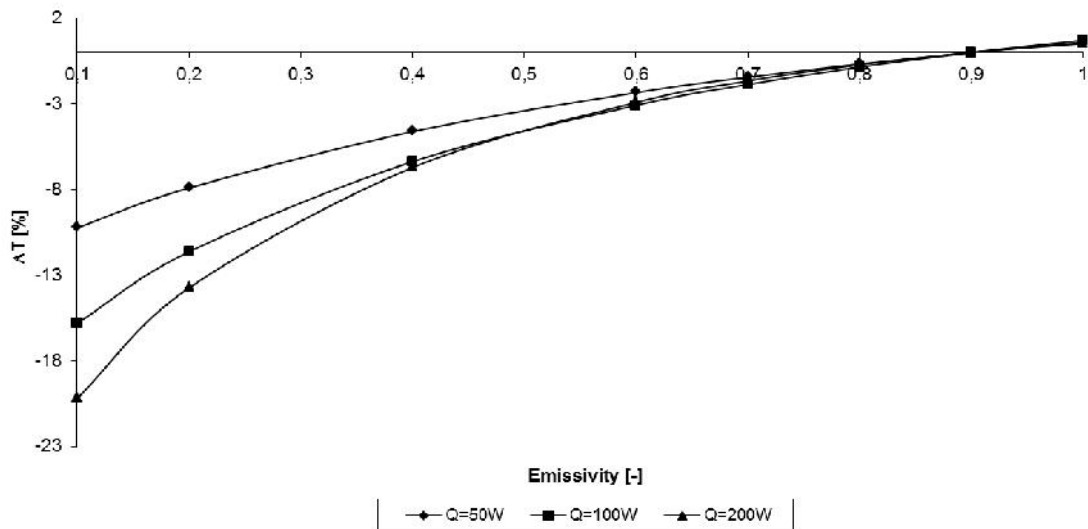


Figure 5-39: Temperature differences for Step with different heat sources and changing emissivity.

Finally, the change in conductance is elaborated. In Figure 5-40 the thickness is shown on the abscissa. This value directly influences conductance. When changing thickness, one can control the relative share of conduction on the total heat fluxes. When radiation becomes the strongest player temperature changes in a strong non-linear way. Figure 5-42 confirms the deviations at small thicknesses. Here, conduction is hampered because of the small interfacial area.

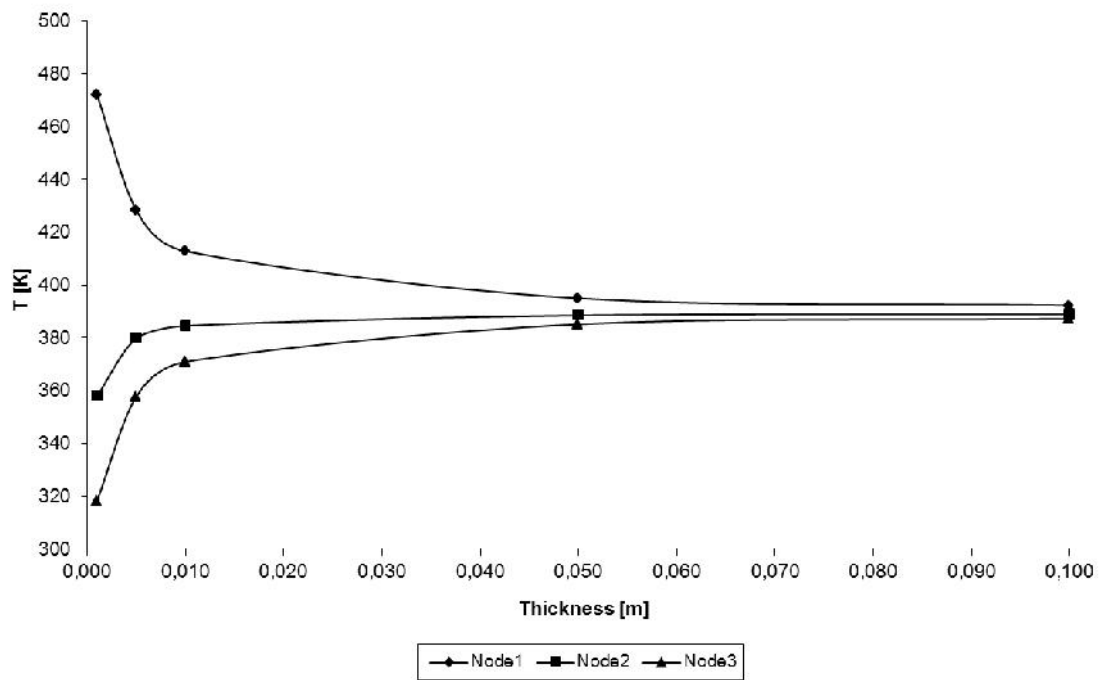


Figure 5-40: Temperatures for Step at $Q=50W$ with changing thickness.

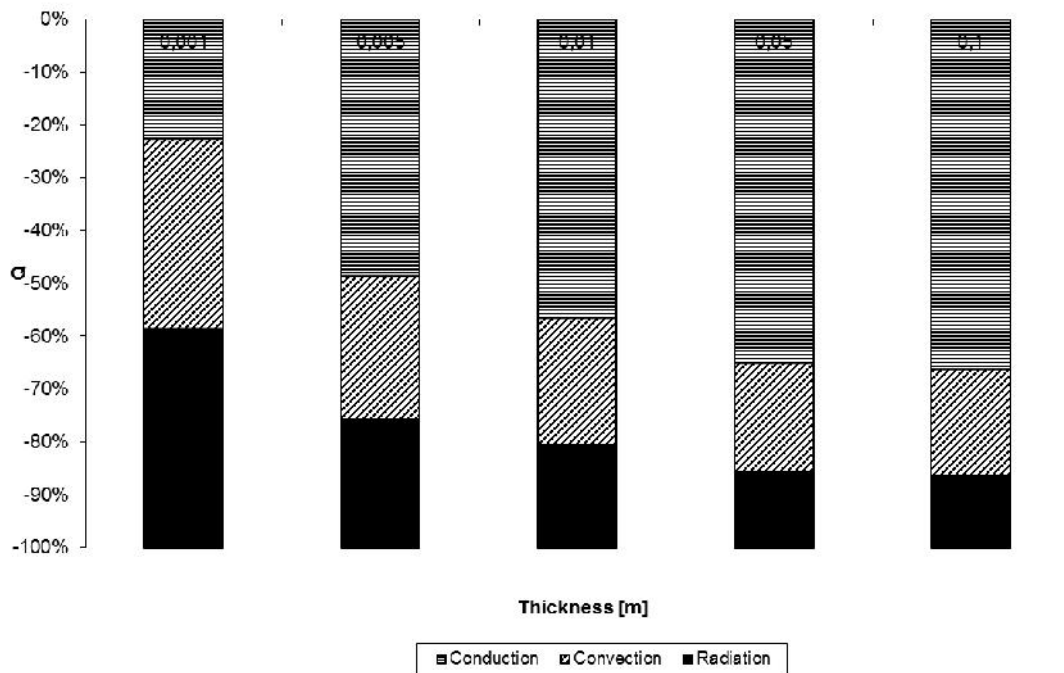


Figure 5-41: Heat flux shares for Step at $Q=50W$ with changing thickness.

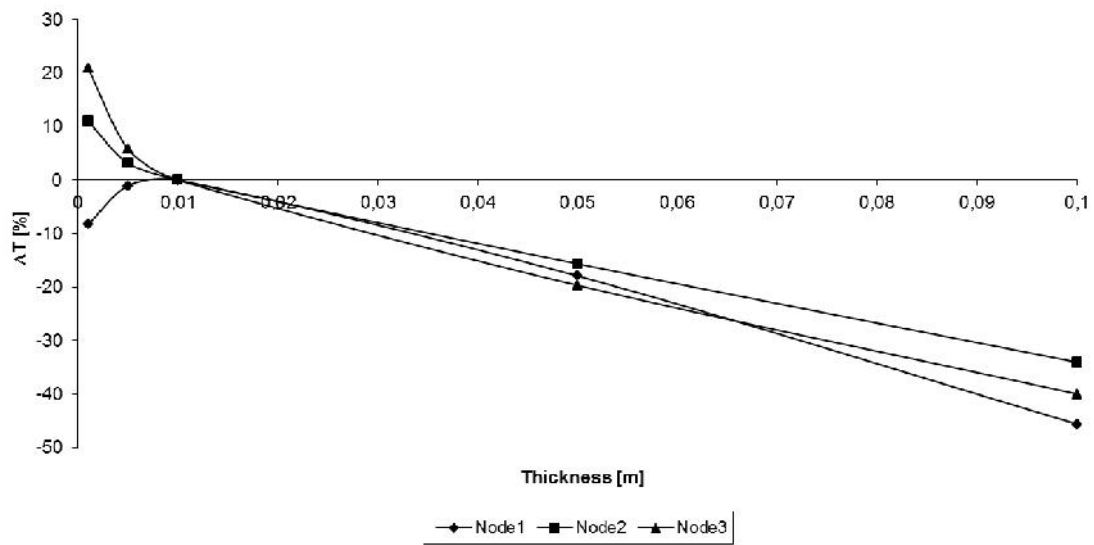


Figure 5-42: Temperature differences for Step at $Q=50W$ with changing thickness.

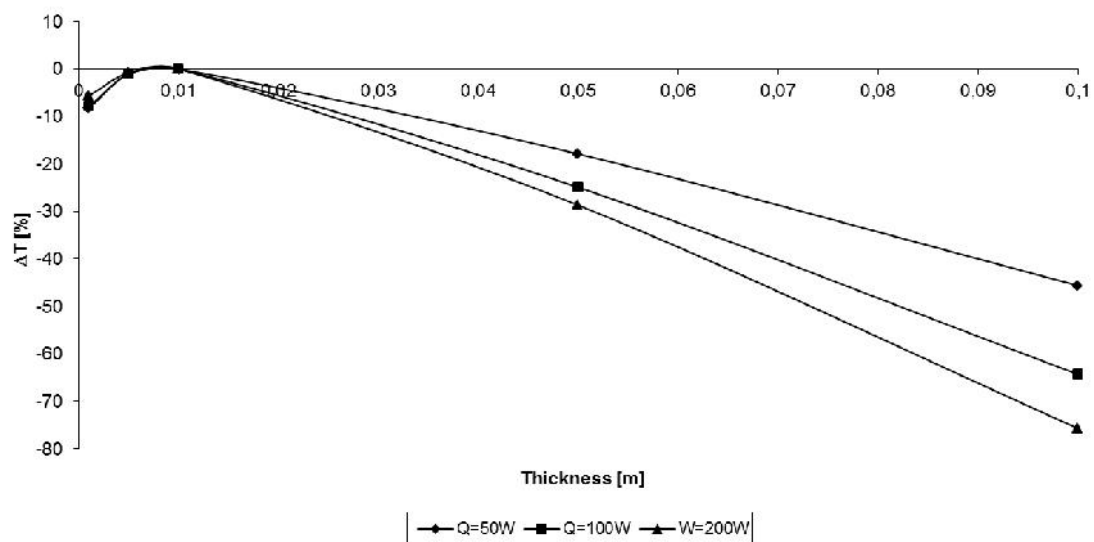


Figure 5-43: Temperature differences for Step with different heat sources and changing thickness.

But this cannot explain the large deviations on the right of Figure 5-41 where conduction is predominant. This effect is even more pronounced when raising the heat flux at node '1'. In order to explain this phenomenon, UFs were calculated at a thickness of 0.05m and the temperatures estimated with them. The behavior on the right side of Figure 5-44 shows a big improvement at the expense of some slightly raised errors on the left side of the diagram. The same trend can be observed in Figure 5-45 for node '1'. This issue with parameter dependant UFs is the same as for non-linear equation solvers as gradients can change severely.

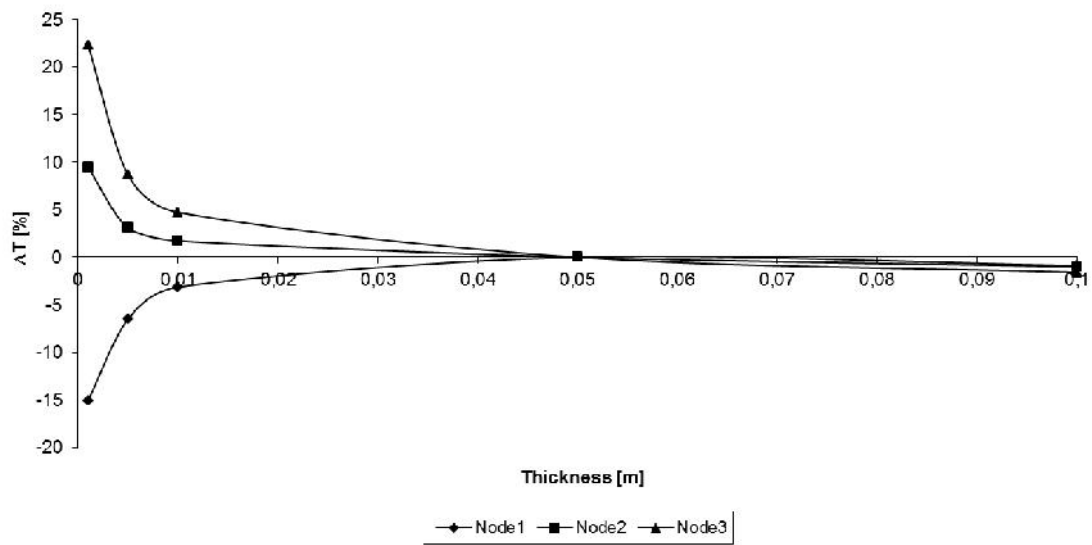


Figure 5-44: Temperature differences for Step at $Q=50W$ and UFs at a thickness of $0.05m$ with changing thickness.

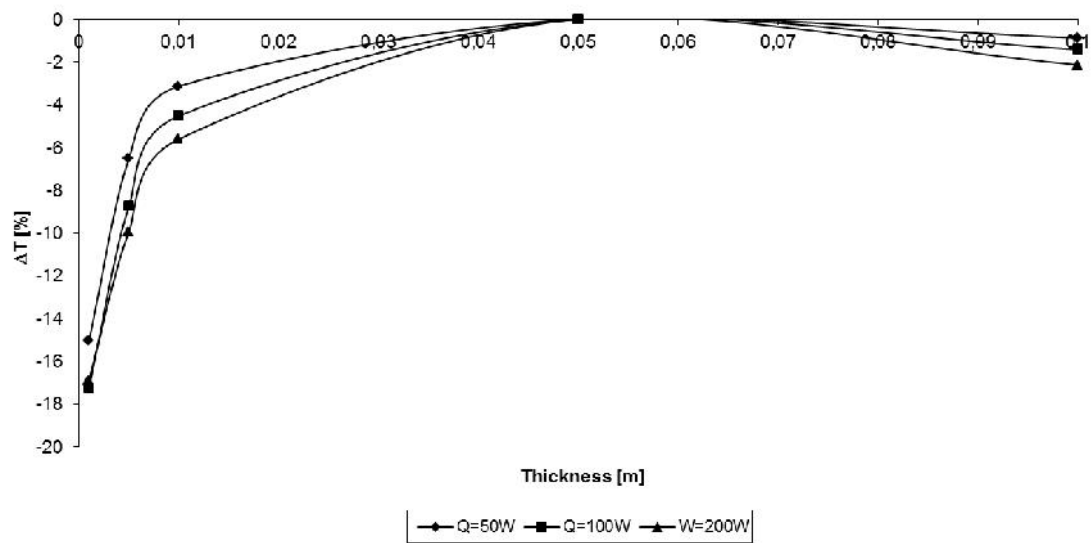


Figure 5-45: Temperature differences for Step with different heat sources and UFs at a thickness of $0.05m$ with changing thickness.

This discussion, by no means, shall diminish the usability of the equations derived. It shows that these coefficients are valid at the base setting and there reveal a lot of information for the thermal analyst. With this work the present author hopes of having been able to derive hands-on formulations that the practicing engineer can employ for real-world applications.

6 Conclusions

Even though the author made an effort to elaborate on the use of the surface-to-surface (S2S) model for automotive applications, this by no means can cover the entire research effort. Despite of the age of this model, there are still areas left for research. For example, in deriving the first order derivatives for the finite difference formulation in the previous chapter, the treatment for the heat transfer coefficient (HTC) was omitted. Since the HTC does depend on the fluid temperature and the element temperature, this parameter cannot be regarded as independent from a statistically point of view. In order to quantify the assumed degree of interaction or covariance, a global sensitivity analysis would have to be conducted. The interaction in the proposed method is taken care of. The second order derivative would allow for estimating saddle points. Generally, higher order terms would one allow formulating the expected change in view factors by applying a Taylor series expansion, thus allowing a formulation of a simple reduced model for thermal radiation.

Another open area of research would be the numerical treatment of the equations of uncertainty. As has been shown, introducing the conductive term necessitates preconditioning for use in iterative solvers. In this work, only a closed solution by LU factorization was presented, which renders the method difficult to employ for industrial sized applications.

According to Saltelli et al. (2008) local sensitivity analysis is not suitable for non-linear models and for parameters differing in several orders of magnitude. Introducing temperature dependant properties such as emissivity, a strong non-linear behavior of the uncertainty equations is expected. A comparison with global sensitivity methods such as Monte Carlo might be necessary. Second order derivatives might help in increasing the range of applicability of the method.

Introducing time dependency greatly increases computation time. The applicability of the reverse mode adjoint method or the forward mode direct differentiation needs to be investigated along with possible shortcuts.

When conducting uncertainty calculations for view factors, it was shown, that the effort is of the order of N^2 not counting the actual matrix vector multiplications for the RHS. This is another stumbling block for industrial applications. One way of dealing with this would be the use of patching or Monte Carlo screening methods to approach full-scale uncertainty results.

For the practicing thermal simulation engineer of great benefit would be to see how uncertainties might contribute in defining a convergence criteria for coupled simulations.

In this work, only parametric uncertainties were considered. The influence of discretization might be investigated. Also, epistemic uncertainties might be quantified with the goal in mind how the results as range of ranges might aid the engineer in decision making.

The derivations of sensitivity factors simplified the approach by assuming that all neighboring nodes are either all temperature fixed or all have a heat flux specified. The equations need to be reviewed for the situation of neighbors with mixed boundary conditions.

At present, view factors are looked up by the binary search algorithm, because view factors are stored at the thermal node according to their destination j . Because the reciprocity relation was not guaranteed the corresponding view factor has to be looked-up at the receiving node j . Because zero entries were not saved, binary search was employed. Introducing a suitable data structure could speed-up large-scale problems. Alternatively, the equations could be reformulated for enforced reciprocity and closure.

The lumped term 'conductance' was treated in this thesis, because this term was readily available from the commercial solver. Using thermal conductivity and geometric parameters instead would be more consistent with the other derivations.

Since in this work local sensitivity is considered, the range of validity needs to be investigated more deeply. The question needs to be answered without simulation experiments of the last chapter, how large the incremental change is allowed to become for a valid prediction.

A local derivative presumes a continuous, differentiable function. Occluders are introducing discontinuities. At present partial shading cannot be predicted. Global uncertainty analysis is more suitable for this phenomenon.

In the derivations it was presumed that a change in one thermal node would independently occur from other nodes. In industrial cases of radiation solvers selections exists, where thermal nodes share physical properties or view factor settings. It remains to be investigated, how changing a parameter for several nodes in a selection simultaneously would improve the usability of the proposed method of uncertainty estimation for large-scale models.

The continuous sensitivity equation method should be used to obtain gradients free of discretization errors. By the method of manufactured solutions an analytical solution can be obtained.

Sensitivity coefficients play an important part for inverse heat transfer solutions. For example, by Tikhonov regularization some questions in industrial applications could be answered such as how the surrounding geometry should be shaped or what material properties are needed to maintain a system at a specified temperature.

Effort has been put into presenting an overview on thermal radiation use in the automotive industries. The radiation method most used in this sector has been described along with recent developments in dealing with meshes of industrial size. A coupling architecture has been developed. It was attempted to show why one needs to know how a simulation model will behave in changing a parameter. A local sensitivity and uncertainty analysis has been applied to the conjugate heat transfer problem and its usability demonstrated on a simple model.

7 Literature

Ambirajan A., Swaminathan P., Venkateshan S., 2010. The Effect of Directional Radiative Surface Properties on the Performance of Mutually Irradiating Conducting Fins. , 14th International Heat Transfer Conference, Washington DC, USA, IHTC14-22226.

Bader V, Neft J., Kleimeyer M., 2007. Usability of CFD for the Development of Tail and Head Lamps. 3rd European Automotive CFD Conference, Frankfurt/Main, Germany, 255-263.

Baum D., Rushmeier H., Winget J., 1989. Improving Radiosity Solutions Through the Use of Analytically Determined Form-Factors. ACM SIGGRAPH Computer Graphics 23 (3), 325-334.

Bhatia M., Livne E., 2008. Design-Oriented Thermostructural Analysis with Internal and External Radiation, Part 1: Steady State. AIAA Journal 46 (3), 578-590.

Bhatia M., Livne E., 2009. Design-Oriented Thermostructural Analysis with External and Internal Radiation, Part 2: Transient Response. AIAA Journal 47 (5), 1228-1240.

Bittner J., 2002. Hierarchical Techniques for Visibility Computations. Dissertation, Faculty of Electrical Engineering, Prague, Czech Technical University.

Blackwell B.F., Dowding K.J., 2006. Sensitivity Analysis and Uncertainty Propagation of Computational Models. In: Handbook of Numerical Heat Transfer, 2nd ed., Wiley, ISBN 978-0-471-34878-8, 443-469.

Clarksean R., Solbrig C., 1994, Minimization of the effect of errors in approximate radiation view factors. Nuclear Engineering and Design 149 (1), 431-440.

Cohen M., Wallace J., 1993. Radiosity and Realistic Image Synthesis. Academic Press, Cambridge, USA.

De Muth J., 2006. Basic statistics and pharmaceutical statistical applications, 2nd ed, CRC Press, Boca Raton.

Deiveegan M., Ramamoorthy V., Katte S., 2004. Analytical Expressions for View Factors with an Intervening Surface. Journal of Thermophysics and Heat Transfer 18 (2), 273-277.

- Doi A., Itoh T., 1998. Acceleration Radiosity Solutions Through the Use of Hemisphere-Base Formfactor Calculation. *Journal of Visualization and Computer Animation* 9 (1), 3-15.
- Emery A., Johansson O., Lobo M., Abrous A., 1991. A Comparative Study of methods for Computing the Diffuse Radiation Viewfactors for Complex Structures. *Journal of Heat Transfer* 113 (2), 413-422.
- Espinar B., Ramírez L., Polo J., Zarzalejo L., Wald L., 2009. Analysis of the influences of uncertainties in input variables on the outcomes of the Heliosat-2 method. *Solar Energy* 83 (9), 1731-1741.
- Farrington R., Rugh J., 2000. Impact of Vehicle Air-Conditioning on Fuel Economy, Tailpipe Emissions, and Electric Vehicle Range. NREL/CP-540-28960,
- Fleischmann M., 2007. Verfahren zur Berechnung der Viewfaktoren für Strahlungsprobleme. Master Thesis, Technical University Munich, Faculty of Mathematics, 1-50 (German).
- Frémond E., 2008. Integration of simulation in project development process for underhood thermal assessment at VOLVO - 3P -CVDEL. State of the art and perspectives. 4th RadTherm User Group Meeting, Böblingen, Germany.
- Goral C., Torrance K., Greenberg D., Battaile B., 1984. Modeling the Interaction of Light Between Diffuse Surfaces. *Computer Graphics* 18 (3), 212-222.
- Guo J., Du X., 2007. Sensitivity Analysis with Mixture of Epistemic and Aleatory Uncertainties. *AIAA Journal* 45 (9), 2337-2349.
- Hasenfratz J.-M., Lapierre M., Holzschuch N., Sillion F., 2003. A Survey of Real-time Soft Shadows Algorithms. *Computer Graphics forum* 22 (4), 753-774.
- Heinstein M., Laursen T., 2003. A three dimensional surface-to-surface projection algorithm for non-coincident domains. *Communications in Numerical Methods in Engineering* 19 (6), 421-432.
- Herrera L., Lund C., 2007. Underbody temperature simulation - are there pitfalls? 3rd RadTherm User Group Meeting, Böblingen, Germany.
- Howell J., 2010. A Catalog of Radiation Heat Transfer Configuration Factors, 3rd ed., <http://www.engr.uky.edu/rtl/Catalog>.

Jansen W., 2004. Vehicle disc brake cooling factor analysis. 1st RadTherm User Group Meeting, Neu-Ulm, Germany.

Jansen W., 2007. Thermal Management using Radtherm. 3rd RadTherm User Group Meeting, Böblingen, Germany.

Jansen W., 2008. Underhood and AC pipe modeling. 4th RadTherm User Group Meeting, Böblingen, Germany.

Jiao X., Heath M., 2004. Common-refinement-based data transfer between non-matching meshes in multiphysics simulations. *International Journal for Numerical Methods in Engineering* 61 (14), 2402-2427.

Jussila A., 2007. Silverstone Track Surface Temperature Simulation During Race Weekend. 3rd RadTherm User Group Meeting, Böblingen, Germany.

Jussila A., 2008. Paint Oven Thermal Analysis. 4th RadTherm User Group Meeting, Böblingen, Germany.

Klaus P., Demmerle M., von Kropff A., Bruegelmann M., 2004. Application and Validation of RadTherm for GM Fuel Cell Vehicles. 1st RadTherm User Group Meeting, Neu-Ulm, Germany.

Korycki R., 2006. Sensitivity analysis and shape optimization for transient heat conduction with radiation. *International Journal of Heat and Mass Transfer* 49 (13), 2033-2043.

Korycki R., 2010. Sensitivity oriented shape optimization of textile composites during coupled heat and mass transport. *International Journal of Heat and Mass Transfer* 53 (11), 2385-2392.

Krishnaprakas C., 1998. View-Factor Evaluation by Quadratur over Triangles. *Journal of Thermophysics and Heat Transfer* 12 (1), 11-120.

Kumar V., Shenge S., Baskar S., 2010. Underhood Thermal Simulation of a Small Passenger Vehicle with Rear Engine Compartment to Evaluate and Enhance Radiator Performance. SAE 2010-01-0801.

Lange K., Anderson W., 2010. Using sensitivity derivatives for design and parameter estimation in an atmospheric plasma discharge simulation. *Journal of Computational Physics* 229 (17), 6071-6083.

- Lawson D., 1995. An improved method for smoothing approximate exchange areas. *International Journal for Heat and Mass Transfer* 38 (16), 3109-3110.
- Lee S., Woodward C., Graziani F., 2003. Analyzing radiation diffusion using time-dependent sensitivity-based techniques. *Journal of Computational Physics* 192 (1), 211-230.
- Loehrke R., Dolaghan J., Burns P., 1995. Smoothing Monte Carlo Exchange Factors. *Journal of Heat Transfer* 117 (2), 524-526.
- Malalasekera W., James E., 1993. Thermal Radiation in a Room: Numerical Evaluation. *Building Services Engineering Research and Technology* 14 (4), 159-168.
- Michel F., Desmet B., Reister H., Binner T., 2006. Natural convective heat transfer connected with the battery in the trunk. 2nd RadTherm User Group Meeting, Böblingen, Germany.
- Mishra S., Prasad M., 1998. Radiative Heat Transfer in Participating Media - A Review. *Sādhanā* 23 (2), 213-232.
- Modest M., 2003. *Radiative Heat Transfer*, 2nd ed., Academic Press.
- Moshhammer T., 2006. Simulation of Radiation Effects in the Presence of the Exhaust System. 2nd RadTherm User Group Meeting, Böblingen, Germany.
- Nishita T., Nakamae E., 1985. Continuous Tone Representation of Three-Dimensional Objects Taking Account of Shadows and Interreflections. *ACM SIGGRAPH Computer Graphics* 19 (3), 23-30.
- Paulke S., 2007. Modern Ray Tracing Techniques Applied to Radiation Heat Transfer Analysis, FEAonline Technical Conference, Beijing, China.
- Pellegrini M., 1997. Monte Carlo Approximation of Form Factors with Error Bounded a Priori. *Discrete and Computational Geometry* 17 (3), 319-337.
- Phillips D., Marks D., 1996. Spatial uncertainty analysis: propagation of interpolation errors in spatially distributed models. *Ecological Modelling* 91 (1), 213-229.
- Rao V., Sastri V., 1996. Efficient Evaluation of Diffuse View Factors for Radiation. *International Journal of Heat and Mass Transfer* 39 (6), 1281-1286.

Rauch C., Wolfahrt J., Wiesler B., Almbauer R., 2004. On The Importance of Thermal Radiation on Human Comfort in Vehicles. 1st RadTherm User Group Meeting, Neu-Ulm, Germany.

Rauch C., Moshammer T., Almbauer R., 2007. Thermal Radiation Benchmarks for the Automotive Industry. Vehicle Thermal Management Systems 8, Nottingham, UK, 695-704, In: Vehicle Thermal Management Systems (VTMS8), edited by IMechE, Chandos Publishing (Oxford) Ltd, ISBN 978-1-84334-348-6.

Rauch C., Hörmann T., Jagsch S., Almbauer R., 2008. Advances in Automated Coupling of CFD and Radiation. SAE 2008-01-0389.

Rauch C., Hörmann T., Jagsch S., Almbauer R., 2008a. An Efficient Software Architecture for Automated Coupling of Convection and Thermal Radiation Tools. ASME Summer Heat Transfer Conference, Jacksonville, FL., USA, HT2008-56303.

Rauch C., Almbauer R., 2010. Uncertainty and Local Sensitivity Analysis of View Factors for Steady-State Conjugate Heat Transfer Problems. 10th AIAA/ASME Joint Thermophysics and Heat Transfer Conference, Chicago, USA, AIAA-2010-4907.

Rauch C., Almbauer R., 2010a. On Uncertainty and Local Sensitivity Analysis for Steady-State Conjugate Heat Transfer Problems. 14th International Heat Transfer Conference, Washington DC, USA, IHTC14-22859.

Sakai S., Maruyama S., 2003. A Fast Approximated Method of Radiative Exchange for Combined Heat Transfer Simulation. Numerical Heat Transfer, Part B 44 (5), 473-487.

Saltelli A., Chan K., Scott E. M., 2008. Sensitivity Analysis, Wiley, New York.

Saltiel C., Kolibal J., 1993. Adaptive Grid Generation for the Calculation of Radiative Configuration Factors. Journal of Thermophysics and Heat Transfer 7 (1), 175-178.

Sánchez M., Mahan J., 2010. Predicting uncertainty and confidence intervals in thermal radiative modeling using the Monte Carlo ray-trace method. International Journal of Numerical Methods for Heat & Fluid Flow 20 (1), 66-83.

Schröder P., Hanrahan P., 1993. A Closed Form Expression for the Form Factor between Two Polygons. Technical Report CS-404-93, Department of Computer Science, Princeton University.

Schröder P., Hanrahan P., 1993a. On the Form Factor between Two Polygons. 20th International Conference on Computer Graphics and Interactive Techniques, Anaheim, CA, USA, 163-164.

Siegel, R., Howell, J., 2002. Thermal Radiation Heat Transfer, 4th ed., Taylor&Francis, New York.

Shapiro A., 1985. Computer Implementation, Accuracy, and Timing of Radiation View Factor Algorithms. Journal of Heat Transfer 107 (3), 730-732.

Shuai, Y., Zhang H., Tan H., 2008. Radiation symmetry test and uncertainty analysis of Monte Carlo method based on radiative exchange factor. Journal of Quantitative Spectroscopy & Radiative Transfer 109 (7), 1281-1296.

Steinkilberg H., 2006. Thermal simulation in the Manifold Development Process. 2nd RadTherm User Group Meeting, Böblingen, Germany.

Tastan Z., 2008. Coupling RadTherm and Fluent for Radiation Analysis with MpCCI. 4th RadTherm User Group Meeting, Böblingen, Germany.

Taylor R., Luck R., Hodge B., Steele W., 1993. Uncertainty Analysis of Diffuse-Gray Radiation Enclosure Problems - A Hypersensitive Case Study. 5th Annual Thermal and Fluids Analysis Workshop, NASA, Washington DC, NASA CP 10122, 27-40.

Taylor R., Luck R., Hodge B., Steele W., 1994. Uncertainty Analysis of Diffuse-Gray Radiation Enclosure Problems. AIAA Paper 94-0132.

Taylor R., Luck R., Hodge B., Steele W., 1995. Uncertainty Analysis of Diffuse-Gray Radiation Enclosure Problems. Journal of Thermophysics and Heat Transfer 9 (1), 63-69.

Taylor R., Luck R., 1995. Comparison of Reciprocity and Closure Enforcement Methods for Radiation View Factors. Journal of Thermophysics and Heat Transfer 9 (4), 660-666.

Thermoanalytics, 2003. RadTherm Technical Documentation.

- Thunnissen D., Au S., Tsuyuki G., 2007. Uncertainty Quantification in Estimating Critical Spacecraft Component Temperatures. *Journal of Thermophysics and Heat Transfer* 21 (2), 422-430.
- Tuomaala P., Piira K., 2000. Thermal Radiation in a Room: An Improved Progressive Refinement Method. *Building Services Engineering Research and Technology* 21 (1), 9-17.
- Valli A., Carey G., Coutinho A., 2008. On decoupled time step/subcycling and iteration strategies for multiphysics problems. *Communications in Numerical Methods in Engineering* 24 (12), 1941-1952.
- Van Leersum J., 1989. A Method for Determining a Consistent Set of Radiation View Factors from a Set Generated by a Nonexact Method. *International Journal of Heat and Fluid Flow* 10 (1), 83-85.
- Vujičić M., Lavery N., Brown S., 2006. Numerical Sensitivity and View Factor Calculation Using the Monte Carlo Method. *Institute of Mechanical Engineers Part C: Journal of Mechanical Engineering Science* 220 (5), 697-702.
- Vujičić M., Lavery N., Brown S., 2006a. New Experimental Data for the Validation of Radiative Heat Transfer. *Experimental Heat Transfer* 19 (3), 193-207.
- Walker T., Xue S.-C., Barton G., 2010. Numerical Determination of Radiative View Factors Using Ray Tracing. *Journal of Heat Transfer* 132 (7), 72702:1-6.
- Walton G., 1986. Algorithms for Calculating Radiation View Factors Between Plane Convex Polygons With Obstructions. National Bureau of Standards, NBSIR 86-3463.
- Walton G., 2002. Calculation of Obstructed View Factors by Adaptive Integration. National Institute of Standards and Technology, NISTIR 6925.
- Watanabe N., Wang W., McDermott C., Taniguchi T., Kolditz O., 2010. Uncertainty analysis of thermo-hydro-mechanical coupled processes in heterogeneous porous media. *Computational Mechanics* 45 (4), 263-280.
- Weidmann E., Wiedemann J., Binner T., Reister H., 2004. Investigations on the thermal effect of soiled underhood components on the temperature distribution in an engine compartment. 1st RadTherm User Group Meeting, Neu-Ulm, Germany.

Williams M., 2010. A probabilistic study of the influence of parameter uncertainty on thermal radiation heat transfer. *International Journal of Heat and Mass Transfer* 53 (7), 1461-1472.

Yamada N., Shinoda T., Takizawa H., 2009. Performance of Hemisphere Algorithm for Fast Form Factor Calculation. *Heat Transfer - Asian Research* 38 (7), 450-463.

8 Appendix

8.1 Case Hexahedron for Uncertainty Calculation

	Left	Right	Front	Back	Bottom	Top
Left	0	0,38638249	0,02492095	0,02492095	0,28188781	0,28188781
Right	0,38638249	0	0,02492095	0,02492095	0,28188781	0,28188781
Front	0,24920949	0,24920949	0	0,00316206	0,24920949	0,24920949
Back	0,24920949	0,24920949	0,00316206	0	0,24920949	0,24920949
Bottom	0,28188781	0,28188781	0,02492095	0,02492095	0	0,38638249
Top	0,28188781	0,28188781	0,02492095	0,02492095	0,38638249	0

Table 8-1: Analytical view factors for hexahedron.

	Left	Right	Front $\frac{F_{ij}}{T_k} \frac{\partial T_k}{\partial F_{ij}}$	Back $\frac{F_{ij}}{q_k} \frac{\partial q_k}{\partial F_{ij}}$	Bottom	Top
Left	0,000000	0,000000	0,000000	0,000000	0,000000	0,000000
	0,135320	0,204170	-0,045733	0,132120	0,129900	0,129900
	0,000966	0,000966	-0,021141	0,000871	0,000966	0,000966
	0,008357	0,008357	-0,002608	0,067739	0,008357	0,008357
	0,094769	0,094769	-0,033365	0,096390	0,148950	0,098721
	0,094769	0,094769	-0,033365	0,096390	0,098721	0,148950
Right	0,204170	0,135320	-0,045733	0,132120	0,129900	0,129900
	0,000000	0,000000	0,000000	0,000000	0,000000	0,000000
	0,000966	0,000966	-0,021141	0,000871	0,000966	0,000966
	0,008357	0,008357	-0,002608	0,067739	0,008357	0,008357
	0,094769	0,094769	-0,033365	0,096390	0,148950	0,098721
	0,094769	0,094769	-0,033365	0,096390	0,098721	0,148950
Front	0,273350	0,181170	-0,061231	0,176890	0,173920	0,173920
	0,181170	0,273350	-0,061231	0,176890	0,173920	0,173920
	0,000000	0,000000	0,000000	0,000000	0,000000	0,000000
	0,002201	0,002201	-0,000687	0,017842	0,002201	0,002201
	0,173920	0,173920	-0,061231	0,176890	0,273350	0,181170
	0,173920	0,173920	-0,061231	0,176890	0,181170	0,273350
Back	0,129060	0,085541	-0,028910	0,083521	0,082116	0,082116
	0,085541	0,129060	-0,028910	0,083521	0,082116	0,082116
	0,000120	0,000120	-0,002629	0,000108	0,000120	0,000120
	0,000000	0,000000	0,000000	0,000000	0,000000	0,000000
	0,082116	0,082116	-0,028910	0,083521	0,129060	0,085541
	0,082116	0,082116	-0,028910	0,083521	0,085541	0,129060
Bottom	0,148950	0,098721	-0,033365	0,096390	0,094769	0,094769
	0,098721	0,148950	-0,033365	0,096390	0,094769	0,094769
	0,000966	0,000966	-0,021141	0,000871	0,000966	0,000966
	0,008357	0,008357	-0,002608	0,067739	0,008357	0,008357
	0,000000	0,000000	0,000000	0,000000	0,000000	0,000000
	0,129900	0,129900	-0,045733	0,132120	0,135320	0,204170
Top	0,148950	0,098721	-0,033365	0,096390	0,094769	0,094769
	0,098721	0,148950	-0,033365	0,096390	0,094769	0,094769
	0,000966	0,000966	-0,021141	0,000871	0,000966	0,000966
	0,008357	0,008357	-0,002608	0,067739	0,008357	0,008357
	0,129900	0,129900	-0,045733	0,132120	0,204170	0,135320
	0,000000	0,000000	0,000000	0,000000	0,000000	0,000000

Table 8-2: Normalized sensitivity coefficients with analytical view factors for the hexahedron.

Table 8-2 represents sensitivity coefficients for each column face. Each row represents a view factor that is changed. For example, the ninth row states, that a change of the view factor from 'Right' to 'Front' will cause the sensitivity coefficients for the faces in each column in that row. The 10th row treats the view factor from 'Right' to Back' and so forth. It should be noted, that the third column has the sensitivity coefficient with respect to the net heat flux q_k , because for the face 'Front' the temperature was fixed. All other columns have the sensitivity coefficient with respect to face temperature T_k , as the temperature was calculated for those faces.

8.2 Uncertainty Factors for the Muffler

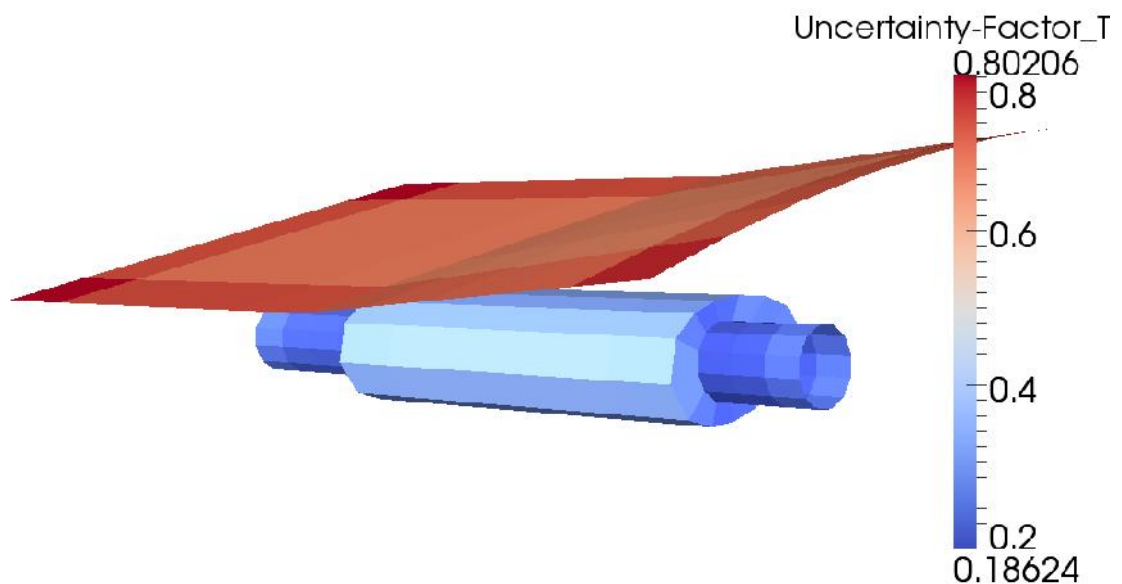


Figure 8-1: Uncertainty factor for fluid temperature for front nodes of the muffler.

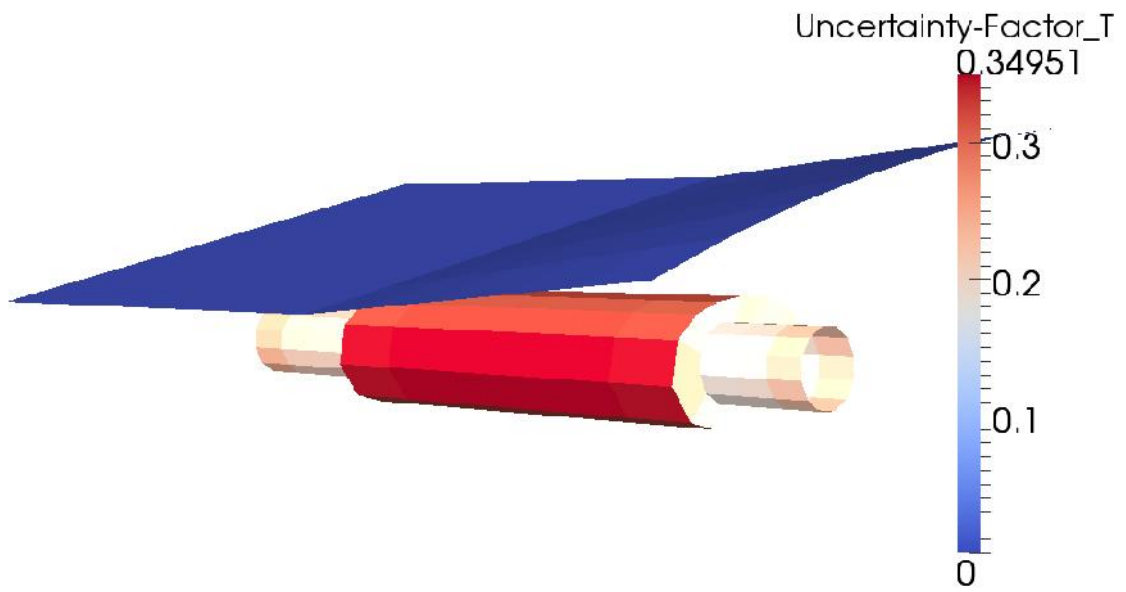


Figure 8-2: Uncertainty factor for fluid temperature for back nodes of the muffler.

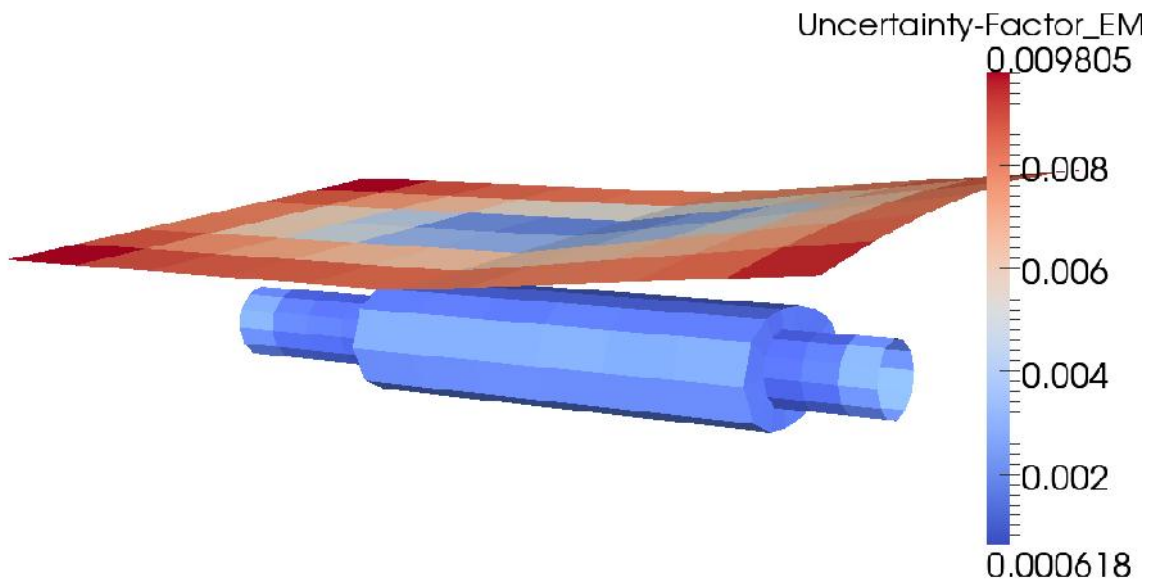


Figure 8-3: Uncertainty factor for emissivity for front nodes of the muffler.

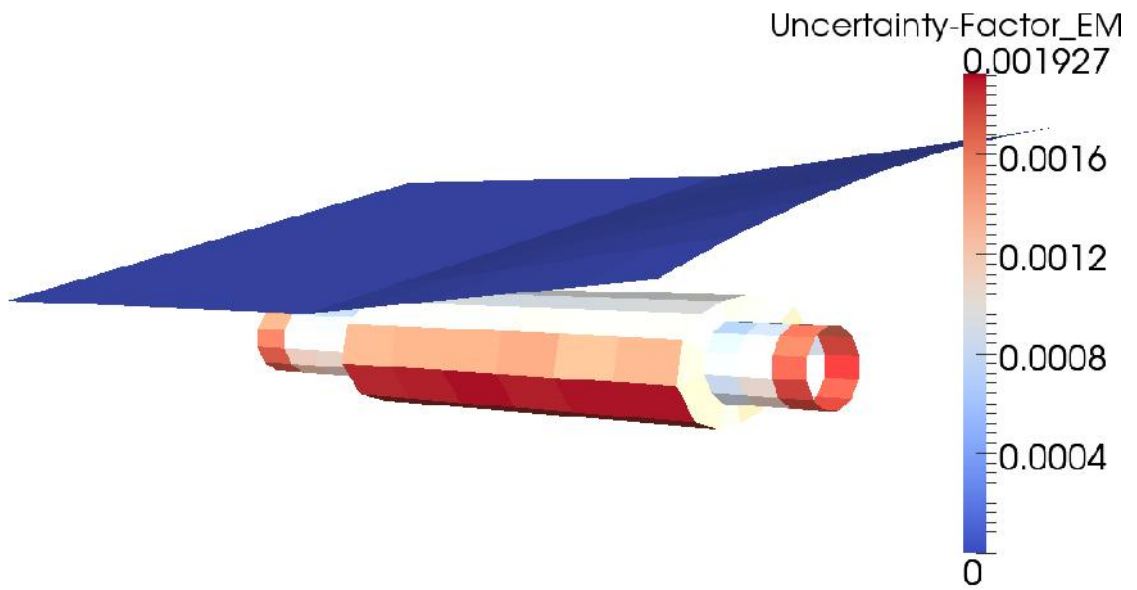


Figure 8-4: Uncertainty factor for emissivity for back nodes of the muffler.

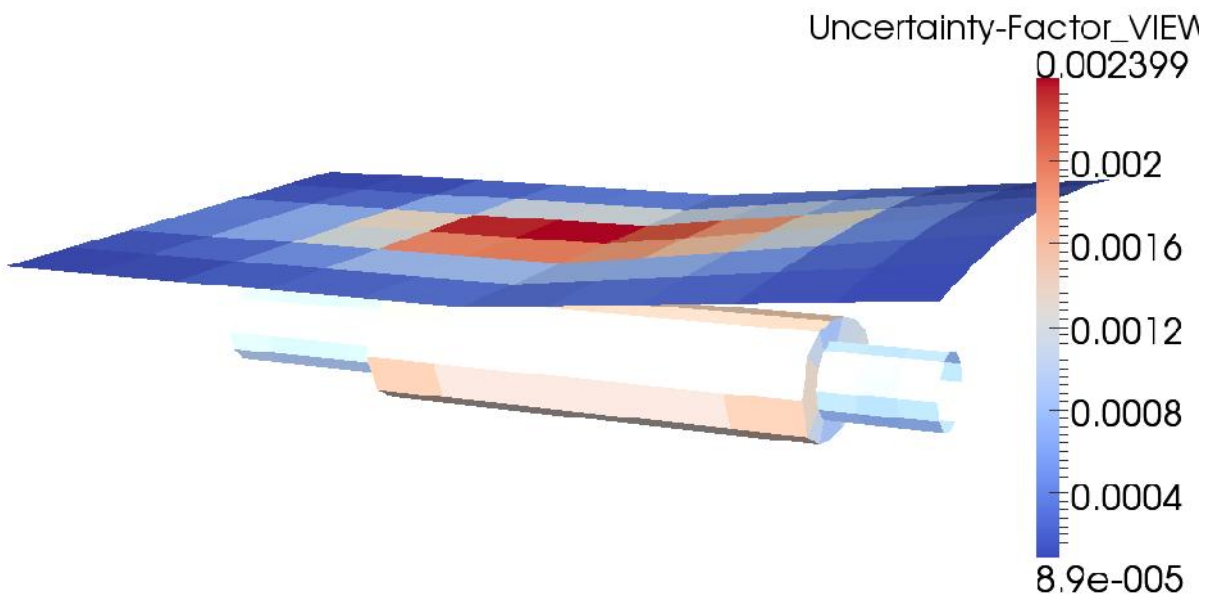


Figure 8-5: Uncertainty factor for view factor for front nodes of the muffler.

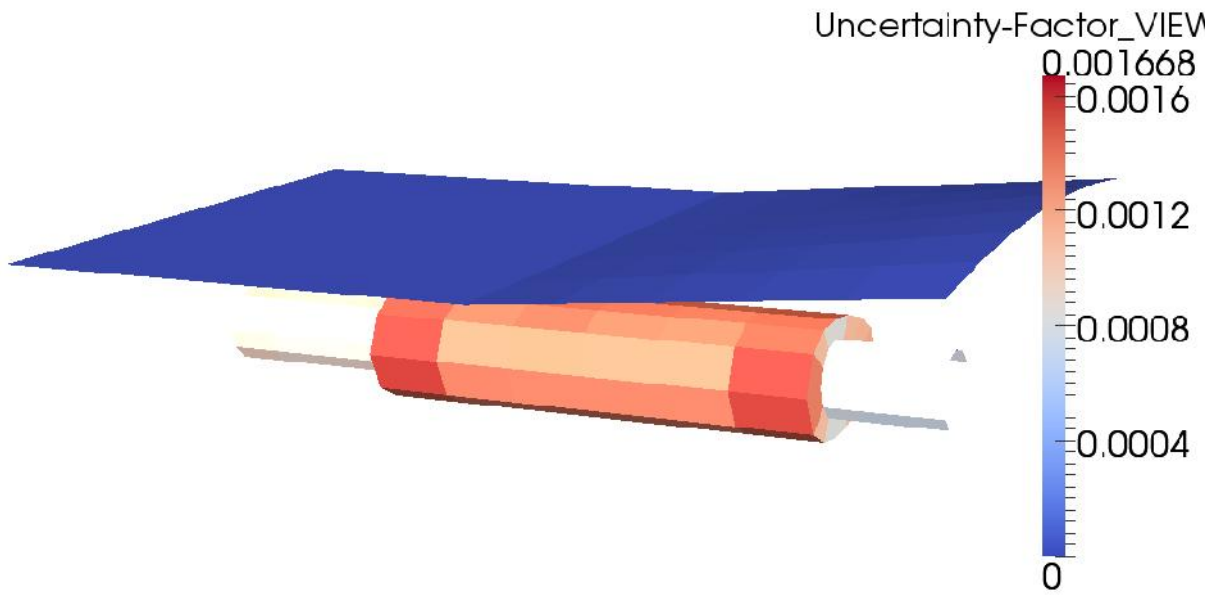


Figure 8-6: Uncertainty factor for view factor for back nodes of the muffler.

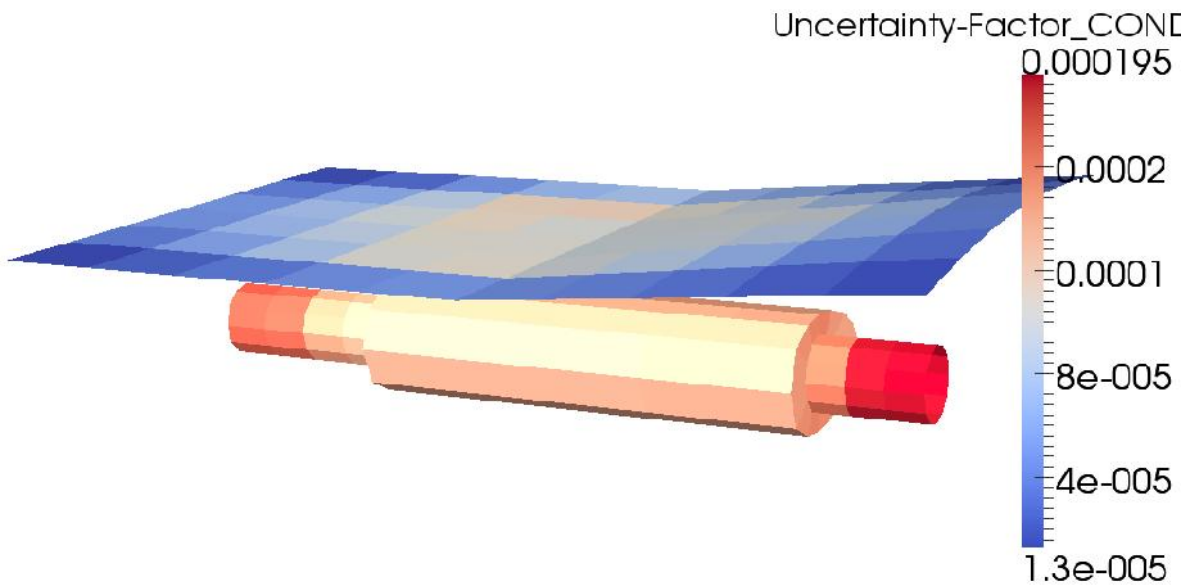


Figure 8-7: Uncertainty factor for conductance for front nodes of the muffler.

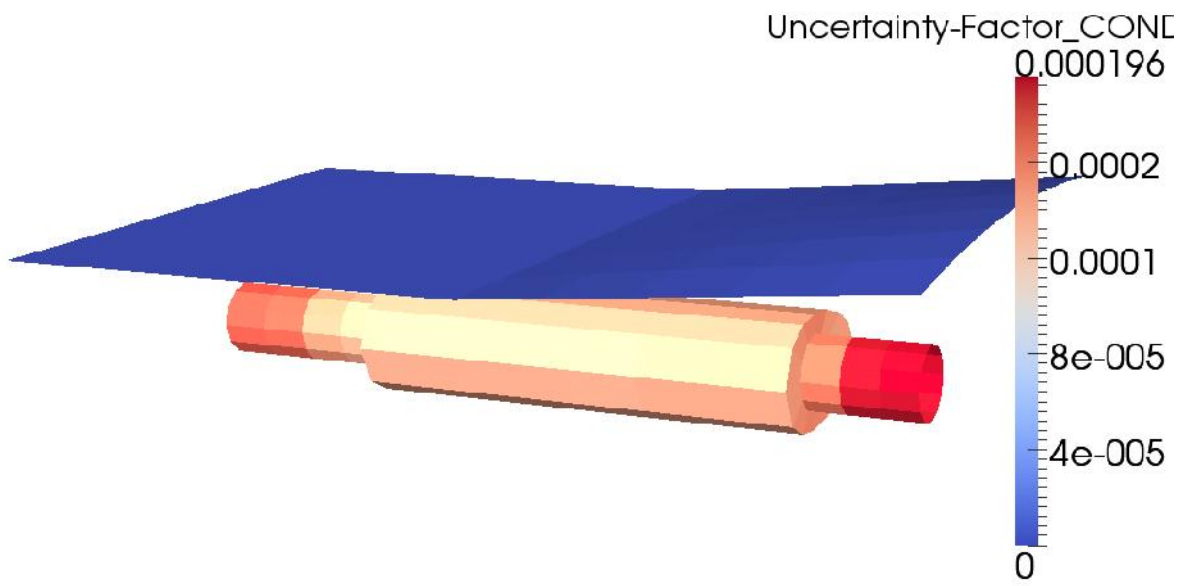


Figure 8-8: Uncertainty factor for conductance for back nodes of the muffler.